Modelling turbulent effects of stellar feedback in cosmological simulations

Dissertation
zur Erlangung des mathematisch-naturwissenschaftlichen
Doktorgrades
„Doctor rerum naturalium“
der Georg-August-Universität Göttingen

im Promotionsprogramm PROPHYS
der Georg-August University School of Science (GAUSS)

vorgelegt von
Jan Frederik Engels
aus Duisburg
Göttingen, 2017

Betreuungsausschuss:
Jens Niemeyer, Institut für Astrophysik, Universität Göttingen
Wolfram Schmidt, Hamburger Sternwarte, Universität Hamburg
Dominik Schleicher, Department of Astronomy, University of Concepcion

Prüfungskommission:
Referent: Jens Niemeyer, Institut für Astrophysik, Universität Göttingen
Koreferent: Ansgar Reiners, Institut für Astrophysik, Universität Göttingen

Weitere Mitglieder der Prüfungskommission:
Wolfram Schmidt, Hamburger Sternwarte, Universität Hamburg
Eberhard Bodenschatz, Institut für Nichtlineare Dynamik, Universität Göttingen
Karl-Henning Rehren, Institut für Theoretische Physik, Universität Göttingen
Wolfram Kollatschny, Institut für Astrophysik, Universität Göttingen

Tag der mündlichen Prüfung:

Ever tried. Ever failed. No matter.
Try again. Fail again. Fail better.
— Samuel Beckett, *Worstward Ho*

Contents

1 Introduction

How and to which extent do turbulent gas motions affect galaxies and their surroundings? Turbulence has been studied in galaxies extensively. Studies concerned with the surroundings of galaxies have mostly ignored turbulent effects. Here, we examine not only the influence of a turbulent subgrid model, but we also investigate the influence of explicit turbulent feedback and turbulent transport processes on star formation, feedback, and the surroundings of galaxies. The importance of the turbulent processes is ab initio not known, but they may have potentially significant influence on the efficiency of star formation and stellar feedback. We also expect to solve the overcooling problem in a physically well-motivated way. For this, we employ a turbulent subgrid model and develop a model for star formation and stellar feedback which is coupled to the turbulent subgrid model.

The first section of this introduction provides a summary of the large scale processes leading to galaxy formation. The second one, in contrast, concentrates on the processes inside galaxies and the influence of various processes on their evolution. Finally, we discuss related literature and give a motivation for our work with an outline of the following chapters in the end.

1.1 A short history of the universe

In this section, we give an overview of the current understanding of the formation of the universe in general. For this, we introduce the redshift z and the scale factor $a = \frac{1}{1+z}$. The scale factor describes the relative expansion of the universe. As we will see in the following chapter, we can use both quantities as time coordinates. The evolution of the scale factor is governed by general relativity (GR). Together with the cosmological principle, GR is the basis of cosmology. The resulting theory is, nevertheless, nearly newtonian, as we will see in chapter 2.1, where we give a rigorous definition and discussion.

Inflation

Although other scenarios are still under discussion, the most widely accepted models for the formation of the universe assume a very early phase of rapid, exponential expansion, called inflation. During this period, the universe is stretched over 50–70 e-foldings[1]. Therefore, microscopic quantum fluctuations are stretched out to cos-

---

[1] One e-folding corresponds to the multiplication by e; the actual number of e-folding is highly model-dependent.

mological scales. Current observations of the cosmic microwave background (discussed in the following section) measure a scalar spectral index of $n_S \approx 0.96$ [74], which is predicted by the simplest models of inflation. Furthermore, observations find that the universe today is spatially flat, i.e. the curvature of the universe is zero to within per mil accuracy [74]. This finding is called the flatness problem. It is solved by inflation: Due to the rapid expansion, every kind of field except the inflaton field is diluted to very small densities. Additionally, the (quantum-) perturbations of the inflaton field are stretched out and are thereby frozen. They act as seeds for structure formation described in later sections. At the end of inflation, a process referred to as reheating produces standard model particles from the decaying inflaton field.

Big Bang nucleosynthesis and Recombination

During the subsequent three minutes, the universe goes through the electro-weak and the QCD phase transition, and the big bang nucleosynthesis forms hydrogen, helium, and traces of light metals [112].

During this time, also dark matter is formed. Dark matter is a matter component in the universe that by definition does not interact with photons in the way baryonic matter does, which makes it invisible or "dark". However, as we will see later, it plays an important role in modern cosmology.

The following era is dominated by matter, which is kept ionized by the still abundant photons. According to the Friedman equation, discussed in the next chapter, the universe expands up to the point at which it becomes cold enough for neutral hydrogen to form, which is called the era of recombination and takes place around $z = 1100$ [112]. The photons emitted during this process are redshifted and constitute, today, the cosmic microwave background (CMB). The CMB is an invaluable source for cosmological observations since the fluctuations in its temperature are directly connected to the quantum fluctuations in the early universe (as described in the previous section). Among the problems posed to cosmological theories by observations is the fact that the CMB has the same temperature of 2.7 K everywhere with deviations of order 10^{-5} [75]. Without the assumption of inflation, the different parts of the sky could not have had causal contact during the lifetime of the universe. This is called the horizon problem.
Additionally, measurements of the CMB have led to very precise determinations of the cosmological parameters. The power spectrum of the anisotropies in the CMB also gives one of the most striking arguments in favor of dark matter. For our purpose, we assume dark matter to be cold dark matter which interacts only via gravity.

Dark ages and reionization

Following recombination, the primordially produced species are in a neutral state. The universe does not contain stars or galaxies yet but only diffuse matter. Most emitted photons would be captured by the neutral medium, which is why this phase is called dark ages. Subsequently, gravitational collapse becomes important and forms first structures with enhanced density [112]. These objects eventually form the first stars which then ionize their immediate surroundings by forming ionized bubbles which merge into larger bubbles over time. This process is called reionization. Moreover, these first stars, forming around $z = 15 - 20$, also produce the first metals and start enriching their environment with elements [116].

It is assumed that stars alone can not reionize the universe as a whole. One solution is the assumption of the formation of early black holes, which help reionizing by emitting huge amounts of radiation [116]. The sequence of star and black hole formation and their possible interplay is not clear and subject to active research. At the end of this epoch, most of the matter is ionized again, hence the name reionization. The end time of reionization is not yet known. Different observations give values between $z = 9$ and $z = 6$, some even up to $z = 15$ [116].

Structure formation

Chronologically speaking, structure formation has already started with the formation of first stars and black holes in early haloes. Structure formation is widely thought to happen bottom-up. This means that small structures form first. They are seeded by density perturbations with a small wavelength (which corresponds to small scales) [112]. After recombination, these structures are formed from baryonic and dark matter simultaneously [116]. Eventually, larger perturbation modes become unstable, and small objects consequently merge to form larger ones. This way of formation is one of the most important. Additionally, mass is also accumulated by gas accretion from the surrounding medium. The initial perturbations are related to the perturbations in the CMB and, therefore, well-understood. As these initial pertubations are small in amplitude, they can be treated in linear perturbation theory, a method also being used for the generation of initial conditions for the cosmological simulations described in this work. As soon as cooling becomes efficient, the baryonic matter collapses further and forms dense objects in the potential wells of dark matter haloes [112]. These dense baryonic objects eventually become galaxies. On the background of structure formation, a rich collection of phenomena occurs in the newly formed galaxies. These include galaxy formation and evolution and, consequently, star formation and stellar feedback.

At late times (i.e. $z < 0.5$), one would expect the expansion of the universe to slow down due to gravity. In contrast, the expansion accelerates. This is attributed to the so-called Dark Energy, which makes up 76% of the current universe [24].

1.2 Galactic processes

For some time, galaxies have been treated as static objects or have been simulated in a closed box, without contact to an environment. But it is known by now that their evolution is highly dynamical and governed by the interplay of many processes, which we are going to discuss in this section, in which we broadly follow [65].

The fundamental process to many of the following mechanisms is cooling. The atomic processes which allow gas to cool differ depending on gas temperature and composition. Above 10^7 K, gas is fully ionized and cools via bremsstrahlung. Between 10^6 K and 10^4 K, excitation and deexcitation processes of hydrogen and helium are most important. Below 10^4 K, pristine gas cannot cool since hydrogen and helium do not have corresponding transitions [40].[2] If cooling becomes efficient so that the cooling time becomes smaller than the sound crossing time of the gas, it is no longer supported by thermal pressure and catastrophic collapse sets in. It is important to note that cooling becomes more effective, the denser the gas gets for increasing gas density in the regime of cosmic structure formation. This enables the gas to form dense cores in the centers of their dark matter host haloes.

One of the most important processes in galaxies is star formation. Star formation is the formation of hydrostatic objects, namely stars, from cold gas that collapses under its own gravity because self-gravity is no longer counteracted by thermal pressure. The stability of a system in this regard can be quantified by the Jeans criterion. Cooling is an important aspect here since it reduces thermal pressure and thereby enhances gravitational collapse [60]. Once nuclear fusion in the star is ignited, it reaches a hydrostatic equilibrium. Stars heat up their surroundings through UV radiation and supernova explosions and produce metals during their lifetime. Many aspects of star formation, such as stellar lifetime, metal production, properties of stellar winds, and the initial mass function (number of stars produced per mass bin), are not well-known and therefore have to be modeled in numerical simulations.

Cooling – and the ensuing gravitational collapse of cold gas – alone would render star formation far more efficient than the observed amount. Therefore, a process counter-acting star formation is needed. Sufficiently violent processes are stellar feedback and feedback from active galactic nuclei (AGN). Both heat the gas in their surrounding and thereby stop star formation. In this work, we focus on stellar feedback, which comprises of stellar winds and supernova explosions, and completely neglect AGN.

Stellar feedback has another effect: It enriches the surroundings with metals. During primordial nucleosynthesis, mostly hydrogen ($\approx 75\,\%$) and helium ($\approx 25\,\%$) are formed [112]. Heavier elements initially only make up traces and are subsequently formed in stars. From a galaxy evolution perspective, metals enhance

---

[2] Molecular hydrogen, in contrast, can cool below 10^4 K, if it is not disassociated by radiation.

star formation. This is due to the fact that metals provide additional atomic processes which work as cooling channels. Below 10^4 K, rotational and vibrational transitions and de-excitation of metals are the dominant processes contributing to cooling rates [99]. Therefore, feedback not only suppresses but also enhances subsequent star formation. With increasing enrichment, star formation becomes more efficient.

The momentum injected by stellar feedback leads to the creation of shock fronts and introduces turbulence into the medium. Turbulence induces an effective pressure and decays into heat, corresponding to higher thermal pressure. Both effects work against collapse and therefore reduce star formation. On the contrary, turbulence induces density variations, which may help in increasing the efficiency of cooling and thereby collapse. Additionally, turbulent flows transport material. This is especially interesting for metals, as turbulent transport smoothes the metallicity distribution, which may have two effects: On the one hand, it enriches pristine gas and therefore boosts cooling and star formation. On the other hand, it decreases the metallicity of strongly enriched gas and thereby decreases cooling. Which of both effects is more important shall be investigated in this work.

In the previous section, we noted that structure formation is largely due to merger events. These merger events have significant influence on the evolution of galaxies. If both objects are of similar mass, the galaxies get disrupted and may form ellipticals afterwards. During merger events, the gas of the galaxy gets shock-heated. This leads to density enhancements, which can trigger a star burst or AGN activity via the cooling instability. Mergers with smaller objects do not have such drastic consequences. In most cases, the smaller object is disrupted and feeds the larger one with gas. Nevertheless, merging events with small objects happen frequently and are an important source of matter in galaxies.

The processes and their aspects briefly discussed here will be addressed in the following chapters. Turbulent effects, their modeling, and their influence are the main topic of this work, as we will motivate in the next section.

1.3 Motivation

In recent years, the circumgalactic medium (CGM) has gained a lot of attention since only then it has become feasible to observe it in detail. The CGM connects the intergalactic medium (IGM) on larger scales with the small-scale dynamics of the interstellar medium (ISM) inside galaxies. The IGM is often defined by an overdensity of less than 10 and is metal-poor, while the CGM is more enriched and denser (e.g. up to overdensities of 300). For details on the definitions, see section 5.1.

The IGM is well-described by (mostly linear) perturbation theory and is observed intensely through Lyman-α forest absorption (e.g. Busca et al. [9], Lee et al. [48], Rauch [81], Slosar et al. [98]). These observations can even be used to measure fundamental cosmological parameters and may even allow for the measurement of fundamental physical parameters, like the neutrino mass (e.g. Viel et al. [110]). On the other hand, the IGM can be modeled well by simulations (e.g. Lukić et al. [53], Machacek et al. [55], Meiksin [62]).

The situation is somewhat similar for galaxies, although the number of processes and their interplay, as described in the previous section, is a lot more complex. Nevertheless, theoretical models describe galactic key properties quite accurately (e.g. Braun and Schmidt [6], Chabrier [13], Krumholz and McKee [45], Krumholz et al. [46], Mac Low and Klessen [54], McKee and Ostriker [61]), and statistical properties, star formation rates, and mass functions are known observationally (e.g. Baldry and Glazebrook [3, 3], Behroozi et al. [4]). Computer simulations employing the theoretical models are used with success and reproduce observational facts (e.g. Braun et al. [8], Hopkins et al. [32], Kim et al. [42]). However some simulations only deal with isolated galaxies, neglecting most of their surroundings. In this work, we simulate galaxies in a cosmological volume.

In contrast to galaxies and the IGM, observing the CGM is relatively complicated. It can only be seen at redshifts $z = 2 - 3$ in the absorption spectra of a background quasar (Steidel et al. [102, 103]). Nevertheless, a concept of the CGM is an important component for a full understanding of galaxies. Galaxies interact with their surroundings through a number of processes, like accreting gas from the CGM and expelling shock-heated, possibly enriched gas into the CGM. The accretion mechanism itself and the importance of accretion from the CGM for galaxies are open questions. Often, the efficient accretion of cold, non shock-heated gas is proposed (Martin et al. [58]), although this is not fully accepted. A number of simulations have already been done to study the CGM and the CGM galaxy interaction (Fielding et al. [23], Pallottini et al. [72], Shen et al. [95]). Furthermore, Hummels et al. [34] propose to use the comparison between observations and simulations of the CGM as a method to calibrate feedback models.

In this work, we focus on turbulence in the CGM and in galaxies. We also aim to develop the methods necessary to perform the corresponding simulations. Turbulence has been studied in isolated galaxies by Braun et al. [8] using a sophisticated model for star formation and feedback. As against, turbulence has been studied in the IGM (Iapichino et al. [36]) and in the CGM (Iapichino et al. [37]) while the influence of star formation and feedback have mostly been ignored. In this work, we do both. We combine a model for star formation and feedback with a turbulent subgrid model. Furthermore, we couple both by turbulent feedback. Using this, we can study the influence of explicit turbulent feedback and turbulent transport processes on star formation, feedback, and the CGM.

Simulations employing a turbulence subgrid model and star formation have rarely been performed – due to the lack of codes modeling both processes. Nevertheless, these simulations can offer a number of interesting effects: The turbulent pressure and the additional (turbulent) energy budget may have an influence on star formation and on the efficiency of stellar feedback. Explicit turbulent feedback (for which a part of the stellar feedback energy is directly fed into the turbulent subgrid energy) is expected to help additionally with suppressing star formation and the expulsion of enriched gas into the CGM and IGM due to the slow dissipation of turbulent energy into heat. Any of these processes could pose a natural way to overcome the overcooling problem, according to which stellar feedback is cooled away artificially fast and thereby becomes inefficient. Turbulent diffusion might mix out metals to larger radii and thus enrich the CGM and IGM. The assessment of these hypothetical mechanisms is the main motivation for this work.

The structure of this work is as follows: In this first chapter, we have given an overview on the topic and a phenomenological description of the processes involved. In the second chapter, we introduce the methods fundamental to this work and the numerical techniques applied. Chapter three deals with a subproject on cosmological initial conditions that supplements the following study. The fourth chapter is central to this work. We explain the models and their implementation which we developed for this work. In the fifth chapter, we show the applicability of our models and analyse the influence of the various turbulent processes. In the last chapter, we give a summary.

Throughout this work, we use the first person plural, although most of the work was done by the author alone. Parts of this work are reproduced in Engels et al. [20].

2 Basic methods for cosmological simulations

The turbulence deep inside
That takes hold of our lives
— Dream Theater, *Loosing Time / Grand Finale*

As a starting point, we are going to discuss the basics of this work in this chapter. For each of the physics modules, we give the equations and a short motivation. All methods are described elsewhere in great detail.

The simulations described in this thesis are based on the Nyx code described in Almgren et al. [1]. Nyx is a block-structured adaptive mesh refinement (AMR) code designed to be efficient and massively parallel. AMR describes that finer grids and thereby resolution is added in regions of interest and block-structured stands for the fact that whole blocks are refined and not single cells. Nyx heavily relies on the facilities given by BoxLib (last described in [118]).

The content of this chapter is restricted to what is used in Nyx. Additionally, we set a focus on the modelling of turbulence since this is going to play a major role in this work. Nyx is particularly suitable for doing simulations of cosmological structure formation with a focus on the scales of the intergalactic medium. For an example, see Lukić et al. [53]. All ingredients used in their simulations are explained in this chapter, except cosmological initial conditions. As they are generated using a separate code, initial conditions are discussed in the next chapter.

2.1 Cosmology in a nutshell

The so called ΛCDM model is the currently most widely adopted cosmological model. It assumes that the universe is homogeneous and isotropic on the largest scales (i.e. more than 100 Mpc). Its evolution can be described using the Friedmann equation, which allows only for expansion and contraction:

$$H := \frac{\dot{a}}{a} = H_0 \sqrt{\frac{\Omega_M}{a^3} + \Omega_\Lambda}, \tag{2.1}$$

where we neglect both curvature and radiation contributions: The universe can safely be assumed to be flat and radiation contributions are only important at very early times.

H is the Hubble parameter and $H_0 = H(\text{today})$ is Hubble's constant. a is the scale factor. The Ω_i denote the relative contributions to the critical density ρ_c:

$$\Omega_i = \frac{\rho_i}{\rho_\mathrm{c}}\,, \tag{2.2}$$

$$\rho_\mathrm{c} = \frac{3H_0^2}{8\pi G}\,. \tag{2.3}$$

The values for Ω_i and H_0 used throughout this work are taken from Komatsu et al. [44] and are given in table 2.1. We are aware of the updated values by Planck Collaboration et al. [74] and Planck Collaboration et al. [75] but are confident that our result would not significantly change by adopting them.

Cosmological simulations solve the Friedmann equation concurrently and make use of comoving coordinates to model the expansion of the universe. Comoving coordinates are given by

$$r = x \cdot a. \tag{2.4}$$

where r is the proper or physical distance and x the comoving distance. a is a function of the cosmic time t and thereby introduces a redundant time coordinate, which is usually expressed in terms of the redshift $z = 1/a - 1$.

Turning to velocities one finds:

$$\dot{r} = x\dot{a} + a\dot{x}. \tag{2.5}$$

The first term is called Hubble flow and is a contribution due to the accelerated expansion of the universe. In most cosmological simulations, proper peculiar velocities v are employed:

$$v = a\dot{x} = \dot{r} - x\dot{a}, \tag{2.6}$$

in which the Hubble flow is subtracted. Similarly, the density can be transformed into a comoving quantity using the fact that mass is conserved:

$$\rho_\text{physical} = \frac{\rho_\text{comoving}}{a^3} \tag{2.7}$$

In the following, we employ comoving positions, proper peculiar velocities and comoving densities, except where otherwise noted. For convenience, we drop the subscripts.

2.2 Gravity

Gravity is weak compared to the other three forces, but it is a long range force which is dominant on cosmological scales. It is described by the Poisson equation:

$$\Delta\phi = \frac{4\pi G}{a}(\rho_\text{total} - \overline{\rho}_\text{total}) \tag{2.8}$$

Ω_Λ	0.725
Ω_M	0.275
Ω_b	0.046
H_0	70.2 km/Mpc/s
σ_8	0.816

Table 2.1: The cosmological parameters as measured by Komatsu et al. [44]. This set of parameters is employed in all of the simulations described in this work.

Here ϕ is the gravitational potential, G the gravitational constant, and $\rho_{\text{total}} = \rho_B + \rho_D$ the total mass density. The mean density is subtracted since otherwise the periodic boundary would lead to an infinite potential. Or using a more physical motivation, the mean density describes the homogeneous background, which we separate into the comoving coordinates framework.
This equation is discretized and solved on grids using a multigrid technique, which employs a Gauss-Seidel red-black relaxation [1].

2.3 Dark matter

Dark matter is the dominant mass component of the universe. ΛCDM cosmology assumes cold dark matter, which can be described by a pressureless fluid. This corresponds to the Vlasov equation, which is solved by sampling the corresponding distribution function with an ensemble of N-body particles. The resulting equations of motion for the particle i are:

$$\frac{d\mathbf{x}_i}{dt} = \frac{1}{a}\mathbf{u}_i, \tag{2.9a}$$

$$\frac{d\mathbf{u}_i}{dt} = -(\nabla\phi)(\mathbf{x}_i). \tag{2.9b}$$

Since we adopt a grid-based approach in which all non-particle quantities are sampled on a grid, we use a particle-mesh method with cloud-in-cell interpolation to calculate the dark matter density ρ_D. The gravitational potential is calculated on the grid and subsequently interpolated back onto the particles employing the same mechanisms. This approach of combining particles with force calculation on a grid is called particle-in-cell (PIC) or more specifically particle mesh (PM) method. The time integration of the equations of motion is done with a kick-drift-kick algorithm (e.g. see [100]). The methods described here are also applied for the star particles, which are described in chapter 4.

2.4 Baryonic matter

Although baryonic matter makes up only one fifth of the matter content in the universe, it is very important since it is the only component which emission we can directly observe. It is modelled as a hydrodynamic fluid, governed by the Euler equations, to which we add models describing additional effects. These are covered in the remainder of this chapter and in chapter 4.

All of the hydrodynamics equations are conservation equations. The first one is a reformulation of mass conservation:

$$\frac{\partial \rho}{\partial t} = -\frac{1}{a}\nabla(\rho \mathbf{u}) + s_\rho \tag{2.10a}$$

ρ is the baryonic density (we drop the subscript B for convenience) and $\mathbf{u}$ the velocity of the baryons. The source term s_ρ is used to transfer baryonic mass into stellar particles and vice versa. Therefore, it does not lead to the production or consumption of baryonic matter.

The second equation is the conservation of momentum and is often called Euler equation:

$$\frac{\partial a \rho \mathbf{u}}{\partial t} = -\nabla(\rho \mathbf{u} \otimes \mathbf{u}) - \nabla p - \rho \nabla \phi + \mathbf{s}_{\rho u}. \tag{2.10b}$$

The pressure p is computed using the equation of state $p = (\gamma - 1)\rho e$ with the internal energy e and the adiabatic index γ. Sources for momentum ($\mathbf{s}_{\rho u}$) are the turbulence subgrid model (Schmidt and Federrath [89], see the next section) and, once again, stellar particles.

The last set of equations deals with the conservation of the internal energy e and total energy E:

$$\frac{\partial a^2 \rho e}{\partial t} = a\left[-\nabla(\rho \mathbf{u} e) - p\nabla \mathbf{u} + \dot{a}\left(3\left(\gamma - 1\right)\rho e\right) + s_{\rho e}\right], \tag{2.10c}$$

$$\frac{\partial a^2 \rho E}{\partial t} = a\left[-\nabla(\rho \mathbf{u} E) - p\nabla \mathbf{u} + \dot{a}\left(3\left(\gamma - 1\right)\rho e\right) - \mathbf{u}\nabla p + \rho \mathbf{u}\nabla\phi + s_{\rho E}\right]. \tag{2.10d}$$

The equations are redundant since the total energy is given by $\rho E = \rho(e + \mathbf{u} \cdot \mathbf{u}/2)$. Nevertheless, it is useful to solve both since internal and kinetic energy can differ by several orders of magnitude. If, for example, the kinetic energy is large compared to the internal energy, round-off errors would significantly affect the internal energy and might even lead to negative internal energies. Both quantities are synchronized in each timestep. Sources ($s_{\rho e}$ and $s_{\rho E}$) in both equations are stellar particles, the turbulence subgrid model, and heating and cooling.

This set of equations is solved using a higher-order unsplit Godunov method [14]. The construction of the edge states is done using an unsplit piecewise parabolic method [63].

Additionally, the code is able to passively advect quantities. This is primarily used for species, but also for the modelling of stars. Species in our case are hydrogen, helium, and metals[1].

$$\frac{\partial \rho_i}{\partial t} = -\frac{1}{a}\nabla(\rho_i \mathbf{u}) + s_{\rho_i} \tag{2.11}$$

This equation satisfies mass conservation (equation 2.10a) for the species under consideration. Since the velocity and therefore all other quantities for the density fractions are the same as for the total density, the density fractions are transported passively. Sources for species (s_{ρ_i}) are the stellar particles.

2.5 Modelling of turbulence

Turbulence is characterized by random motions in a fluid over a wide range of scales. Although being random, turbulent motions exhibit a well-defined statistical behaviour. One popular definition of turbulence is using the Reynolds number as a proxy to determine whether a flow is turbulent (see e.g. [88]):

$$\mathrm{Re} = \frac{VL}{\nu} \tag{2.12}$$

In this formula, V is the characteristic velocity, L the characteristic length, and ν the viscosity. The Reynolds number compares the influence of non-linear interactions with viscous damping. A flow is turbulent if nonlinear interaction dominates, which is roughly the case if $\mathrm{Re} \gtrsim 10^3$.

Turbulence is important in many astrophysical phenomena, ranging from supernovae [90], over tidal stripping in mergers [35] and galactic star formation [8] to the intergalactic medium [36]. In this work, we are studying turbulence in the circumgalactic medium and the influence of stellar feedback on it. The general idea of turbulence is that turbulent energy is transported from large to small scales via increasingly smaller eddies. This effect is also known as the turbulent cascade, which is depicted in figure 2.1. Thus, turbulence is inherently a multiscale phenomenon since dissipation occurs on molecular scales whereas turbulence is produced on astrophysical scales.

Simulations attempting to resolve the complete energy cascade are called direct numerical simulations (DNS). These are not feasible for cosmological simulations since the dissipation scale is probably far below the grid scale – although the molecular viscosity of the medium is not yet fully determined [91]. If magnetic fields are present, they also reduce the viscosity and thereby the dissipation scale significantly. Consequently, most of the literature uses so called implicit large eddy simulations (ILES). This method focusses on the fact that numerical dissipation usually converts energy at the smallest numerically resolved scales into

---

[1] In the usual astrophysical sense: all atoms that are heavier than helium.

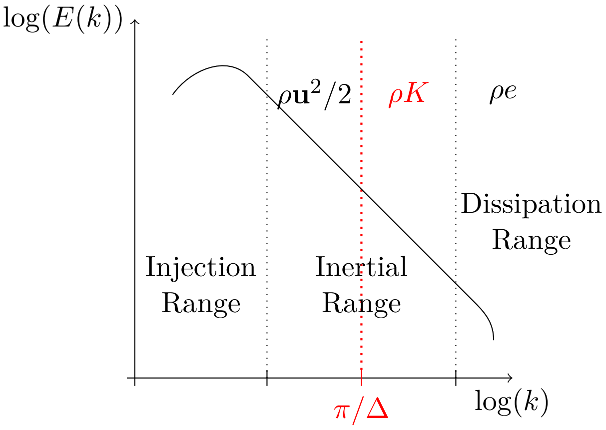

Figure 2.1: Sketch of the energy spectrum of a turbulent flow. The flow is driven in the injection range, and the energy cascades down to ever smaller eddies until it is eventually dissipated to heat in the dissipation range. The labels in the upper part of the image denote the corresponding energy budgets. Δ is the grid scale.

the internal energy budget. In contrast, we (and the literature mentioned above) use a procedure called large eddy simulation (LES). Herein, the influence of the turbulence below the grid scale is explicitly treated by a turbulent subgrid model[2]. This subgrid model emulates the effects of the turbulent motions on smaller scales statistically. We employ a so called one-equation model, which means that we introduce an additional energy budget for turbulence below the grid scale and a corresponding evolution equation. In figure 2.1 this is indicated in red. This turbulent energy budget is of special importance for us, since we are going to use it for explicit turbulent stellar feedback, which is described in chapter 4. The idea is that stellar feedback generates turbulence. Since this is happening far below the grid scale, we explicitly model the turbulence produced by these events and do not rely on indirect turbulence production.

In the remainder of this section, we introduce briefly the equations governing the subgrid model, and we motivate them. We describe the influence of the model on a qualitative level. We further note that in section 4.6 we are going to discuss some steps of the derivation in the context of turbulent mixing which also applies to the equations discussed in the following. For a detailed discussion, see [88], which we broadly follow in this section.

---

[2] In the literature most or all of what we call sources are often called subgrid models. We prefer using the term subgrid model only for the turbulence part.

2.5.1 Equations

Here, we give the full set of equations describing the turbulence subgrid model. They are derived by filtering the hydro equations at the grid scale.

The following equations are the usual equations of hydrodynamics (equations 2.10) plus the source terms from the turbulent subgrid model (in red), as described in [91]: The evolution equation for the density

$$\frac{\partial \rho}{\partial t} = -\frac{1}{a}\nabla(\rho \mathbf{u}) \tag{2.13a}$$

is not changed. We refer to section 4.6, where the reason for this and the implications for the species is discussed.

The modified momentum equation reads:

$$\frac{\partial a\rho\mathbf{u}}{\partial t} = -\nabla(\rho\mathbf{u}\otimes u) - \nabla p - \rho\nabla\phi + \nabla\cdot\boldsymbol{\tau}. \tag{2.13b}$$

The SGS term in the momentum equation is usually modelled as a viscosity term, analogous to the molecular viscosity term in the Navier-Stokes equations. The explicit form of the turbulent subgrid stress tensor τ is discussed in the next section. Its main task is the coupling of small scale turbulent motions to the model, but its trace also gives rise to turbulent pressure.

Internal energy

$$\frac{\partial a^2\rho e}{\partial t} = a\left[-\nabla(\rho\mathbf{u}e) - p\nabla\mathbf{u} + \dot{a}\left(3\left(\gamma-1\right)\rho e\right)\right] + a\rho\varepsilon \tag{2.13c}$$

is supplemented by the dissipation ε of turbulent energy. This effect corresponds to the dissipation of turbulent eddies due to molecular viscosity in a DNS.

For the total energy one finds the following additions:

$$\begin{aligned}\frac{\partial a^2\rho E}{\partial t} =& \, a\left[-\nabla(\rho\mathbf{u}e) - p\nabla\mathbf{u} + \dot{a}\left(3\left(\gamma-1\right)\rho e\right) - \mathbf{u}\nabla p + \rho\mathbf{u}\nabla\phi\right] \\ &+ a\left[\nabla\cdot(\mathbf{u}\cdot\boldsymbol{\tau}) - \Sigma + \rho\varepsilon\right].\end{aligned} \tag{2.13d}$$

The first additional term stems from the SGS turbulent stress term in the momentum equation. Furthermore, the total energy on numerically resolved scale is decreased by the production of turbulent energy Σ and increased by the dissipation.

The new equation is the evolution equation for the kinetic energy of turbulent motions below the grid scale K:

$$\frac{\partial a^2\rho K}{\partial t} = a\left[-\nabla(\rho\mathbf{u}K) + \Sigma - \rho\varepsilon + a\nabla\cdot(\rho\kappa_{\mathrm{SGS}}\nabla K) + S_{\rho K}\right]. \tag{2.13e}$$

The first term is the usual advection term. The second and third term correspond to production and dissipation, respectively. The fourth term describes the diffusion of turbulent energy. Turbulent diffusion is discussed in more detail in section 4.6. $S_{\rho K}$ describes sources of turbulent energy external to the turbulent subgrid model. We are going to use this mechanism for turbulent stellar feedback as described in section 4.5.[3]

The rate of production Σ is given by

$$\Sigma = \tau_{ij} S_{ij} \tag{2.14}$$

where the rate of strain tensor S_{ij} is defined by

$$S_{ij} = \frac{1}{2}\left(\frac{\partial u_i}{\partial x_j} + \frac{\partial u_j}{\partial x_i}\right) \tag{2.15}$$

All the terms mentioned so far can be derived by filtering the hydro equations (equations 2.10). To close the system of differential equations 2.13 the dissipation ε and the subgrid turbulence stress tensor τ are approximated by closures, which are discussed in the following.

2.5.2 Closures

Equation 2.13b has the same form as the Navier-Stokes equation, with the viscous stress tensor σ replaced by the subgrid turbulence stress tensor $\boldsymbol{\tau}$. For this tensor, we use the closure derived in [89]:

$$\boldsymbol{\tau}_{ij} = 2\rho\left(c_1 \Delta \sqrt{2K} S^*_{ij} - 2c_2 K \frac{u_{i,k} u_{j,k}}{|\nabla \otimes \mathbf{u}|^2} - \frac{1}{3}(1 - c_2) K \delta_{ij}\right). \tag{2.16}$$

Here $|\nabla \otimes \mathbf{u}| := \sqrt{2 u_{i,k} u_{k,i}}$ is the norm of the resolved velocity derivative $u_{i,k} = \partial u_i / \partial x_k$, $S^*_{ij} = S_{ij} - \frac{1}{3}\delta_{ij} d$ is the tracefree rate of strain tensor and $d = u_{k,k} \equiv \nabla \cdot \mathbf{u}$ the divergence of the velocity field. Δ is the grid scale. Data from simulations of forced compressible turbulence in periodic boxes yield coefficients $c_1 = 0.02$ and $c_2 = 0.7$.

The closure can be split into two parts: a linear part, of the turbulent viscosity type with $\nu_{\mathrm{SGS}} \propto \Delta\sqrt{K}$, and a nonlinear part. The viscous part models the viscous drag exerted by small scale turbulent eddies on the larger scales. Therefore, it is called eddy-viscosity closure. The second part is motivated by its ability to transport energy through an inverse cascade from small to large scales, which the eddy-viscosity closure can not do in the same way. In contrast, the eddy-viscosity closure is purely dissipative with respect to numerically resolved scales.

The dissipation rate ε is the amount of energy that is dissipated from turbulent energy into internal energy. For LES, the following closure is usually assumed

$$\varepsilon = \frac{c_\varepsilon K^{3/2}}{\Delta}. \tag{2.17}$$

---

[3] For clarity we omitted the sources in the other equations.

It is derived by assuming the Kolmogorov energy spectrum of statistically isotropic incompressible turbulence. As demonstrated in [89], this closure works reasonably well even in the case of compressible turbulence. The coefficient $c_\varepsilon \approx 1.58$ is calibrated under the assumption of an approximate balance between production and dissipation.
Given this dissipation rate, we can define a dissipation timescale by removing everything but the dissipation from the evolution equation for K:

$$\frac{\partial a^2 \rho K}{\partial t} = -\rho\varepsilon. \tag{2.18}$$

Substitution of 2.17 yields:

$$t_{\text{dissipation}} = \frac{1}{4}\frac{a^2\Delta}{c_\epsilon\sqrt{K}}. \tag{2.19}$$

The dissipation and its timescale is going to play a role when analyzing stellar feedback and its efficiency in later chapters.

As indicated above, the trace of the turbulent stress tensor acts as a turbulent pressure:

$$p_{\text{turb}} = \frac{2}{3}\rho K. \tag{2.20}$$

This pressure gives support against collaps of gas in addition to the thermal pressure.

2.5.3 Shear-improved model

Many of the approaches above have been developed using the assumption of homogeneous and isotropic turbulence. This is particularly true for the choice of constant coefficients. However, in cosmological simulations, this assumption is not met, as turbulence is confined to collapsing and merging structures [91]. To account for this Lévêque et al. [49] suggest to split the velocity into a mean flow and a fluctuating part. We exploit the fact that only the fluctuating part contributes to the production of turbulent subgrid energy. Moreover, it is ensured that turbulent subgrid energy production goes to zero if the flow is laminar. This approach is called the shear-improved model, Since replacing the velocity by fluctuating velocity in the first term of the closure (eq. 2.16) changes the shear. Furthermore, shear is the dominant source term in the regime, where turbulence is not fully developed.

Technically, the shear-improved model is implemented by employing a Kalman filter [38] to smooth the velocities in time [10]. The fluctuating shear is then used in the eddy-viscosity closure while the non-linear closure is computed from the full velocities. The Kalman filter contains two parameters: a timescale t_c and a velocity scale u_c. They have to be chosen according to the properties of the flow. In this manner, u_c is chosen to be similar to the velocity dispersion of the flow, and t_c is the timescale on which the turbulence evolves. Schmidt et al. [91] study the effects of different parameter choices for a cluster in a cosmological simulation. We adopt the values used in [92]: $u_c = 300$ km/s and $t_c = 5$ Gyr, since they have proven to work well for a similar problem.

Additionally, the shear-improved model allows for the computation of the local turbulent velocity dispersion [91]:

$$\sigma^2_{\mathrm{Turb}} = \mathbf{u}'^2 + 2K \tag{2.21}$$

where u' is the fluctuating component of the velocity field following from the subtraction of the filtered velocity from the local velocity.

Previous approaches either estimated the turbulent velocity dispersion only from resolved quantities (e.g. [16, 67, 109]) or only from subgrid quantities (e.g. [56, 89]). This approach attempts to combine both, contributions from resolved and subgrid components, and overcomes certain limitations of the previous models [92].

2.6 Heating and cooling

The most abundant elements in the universe are hydrogen and helium. The evolution of their chemical species can be calculated directly since the number of species is low and they form simple reaction networks. We use the approach described in Katz et al. [40] together with a modern integration scheme similar to the one described in Lukić et al. [53]. Gas at temperatures above 10^7 K is fully ionized. In this regime, bremsstrahlung is the most important cooling mechanism. For intermediate temperature between 10^4 and 10^6 K, excitation processes dominate the cooling. We also include ionization and recombination contributions, which are subdominant. Additionally, we consider Compton cooling off the CMB, which is only important at redshifts larger than $z = 6$. At temperatures below 10^4 K, the mentioned cooling rates become negligible. Apart from Compton cooling, all processes are two-body processes, and therefore cooling is more efficient at higher densities.

To account for photoionization one needs to specify an incident radiation field. Like most cosmological simulations, we assume a spatially uniform background of ionizing radiation, for which we use a Haardt and Madau [27] prescription. Their model accounts for ionizing photons from both star forming galaxies and active galactic nuclei. The inclusion of heating leads to the formation of an equilibrium point-dependent density, temperature, and redshift.

This approach, although it is quite standard in cosmological simulations in the literature, has some limitations. For this work, a treatment of cooling and heating by metals is needed, which is described in section 4.1. Metal cooling introduces additional processes which are effective even below 10^4 K. Furthermore, assuming the radiation field as uniform, is obviously an approximation, but tracing ionizing photons is not feasible in most cosmological simulations and would introduce additional complications. Vogelsberger et al. [111] claim that the assumption of an uniform radiation field becomes invalid for densities higher than $10^{13}\ \mathrm{M}_\odot/\mathrm{Mpc}^3$ because gas at such densities becomes optically thick. This effect is usually called self-shielding. Since we typically do not exceed this limit in our simulations – due to their limited resolution –, we ignore self-shielding. In self-shielded regions, the formation of molecular hydrogen becomes important but is ignored here. Dust cooling only becomes important in molecular clouds, which we do not resolve.

3 Cosmological initial conditions for zoom-in simulations

Addiert die Null zehntausend Mal!
Rechnet's nur gründlich aus!
Multipliziert's mit jeder Zahl!
Steht Kopf! Es bleibt euch keine Wahl:
Zum Schluß kommt Null heraus.
— Erich Kästner, *Kleine Rechenaufgabe*

Initial conditions for simulations of galaxy formation can be prescribed in different ways: simple density distributions leading to simulations of so-called isolated disk galaxies (IDG) or cosmological initial conditions representing a patch of the universe at early times. The latter can be either single-level or multi-level (zoom-in, nested) initial conditions. We explain all three variants and discuss their pros and cons.

The term cosmological initial conditions describes initial conditions for a large volume of the universe as given by primordial and early universe physics. The simulated volumes range from around $(10\ \mathrm{Mpc})^3$ (used in this work) to several Gpc^3. If we look at patches of this size in the universe today, we see the full range of cosmic structure: from $0.1 - 100$ kpc for galaxies and a few Mpc for galaxy clusters to filaments and voids filling the huge remaining volume. Although galaxies are comparably small, they contain significant amounts of mass and host particularly complex astrophysical processes. Therefore, galaxies are at the center of interest in most simulations. However, simulations of galaxy formation require high resolution to capture the relevant processes and their interplay.

One can avoid the very large range of scales in cosmological volumes by simulating only one galaxy without any surroundings, i.e. IDGs. Using IDGs, one can obtain resolutions below one parsec, which allows for sophisticated models of galaxy formation (for example, see [8, 43, 61, 101]). IDGs have been used extensively and successfully. However, they completely neglect the influence of the external environment, like accretion from the IGM and merging with other haloes, so this kind of simulation has a limited applicability.

The next step towards more realistic simulations is to simulate galaxies in their natural surroundings using cosmological initial conditions. However, one can not simply run a tiny cosmological patch and hope to find a realistic galaxy: The formation of haloes hosting a galaxy requires tidal fields on scales much larger than the size of the halo ([52]). Additionally, the galaxy needs a gas reservoir from the surrounding intergalactic medium. Furthermore, Power and Knebe [78] find that ommitting the large scale modes (which is equivalent to employing a smaller box) suppresses the formation of heavy objects. A last argument is based on the halo mass function (HMF): The HMF describes the number of haloes in a mass per unit volume. Employing an analytical prescription (like e.g. Sheth et al. [96]) one can calculate the propability of finding a number of n haloes of a given mass in a box with a given volume. For one halo of 10^{12} $\mathrm{M}_{\odot}$ this gives a volume of approximately $(10\ \mathrm{Mpc})^3$.

Using, as we do, a code with adaptive mesh refinement (AMR), one might simply generate initial conditions for an initially uniform grid and evolve them. According to the AMR approach, additional grids are added at runtime in regions which are overdense and possibly fulfill other criteria. Since cosmological initial conditions consist of small fluctuations, refinement is only applied once structure has formed. This approach works fine for a moderate number of additional levels; for simulations resolving galaxies in detail, it does not: Such simulations contain small scales that are not constrained by the initial conditions since these only contain information up to the Nyquist wavelength of the initial resolution. The small scales in the initial conditions are responsible for the formation of small haloes. To solve this, one has to sample the small scale modes already during the generation of the initial conditions. This is done by so-called zoom-in simulations. The idea is to add refinement already in the initial conditions. An initial conditions generator being capable of this approach is MUSIC (multi-scale initial conditions, [28]). Because of its portability to different simulation codes, MUSIC has gained a lot of attention in recent years.

The work described in this chapter was motivated by the AGORA code comparison project [42] dealing with well-resolved galaxy simulations. Moreover, a sophisticated model for the interstellar medium in galaxies was implemented into Nyx and tested in IDG simulations (Braun and Schmidt [6]). The next step would have been to apply this model in a cosmological setup by employing a zoom-in simulation. As a result of our efforts, Nyx is able to deal with initial conditions generated by MUSIC. However, when applying this new feature to cosmological zoom-in simulations, fundamental limitations of the code framework became apparent, which make zoom-ins to galactic scales prohibitively expensive. We discuss the nature of these limitations in a following section. As a consequence, this goal was postponed to future work. An application of nested initial conditions to galaxy clusters will be briefly discussed at the end of this chapter, which is structured as follows: In the first section, we give an overview of the generation of cosmological initial conditions, in the second section, we describe the modifications of Nyx. Finally, we analyze the Nyx-specific problems of this approach and describe results from cluster simulations, which have been obtained using this methodology.

3.1 Cosmological initial conditions

This section is dedicated to giving a short introduction on the computation of cosmological initial conditions. Since we are using MUSIC (Hahn and Abel [28]) in this work, we follow their notation. The level of details discussed here is rather general and by that we restrict ourselves to single-level (non-nested) initial conditions.

The starting point for generating cosmological initial conditions is the power spectrum of density fluctuations $P(k)$. It can be computed from the transfer function $T(k)$ using linear theory:

$$P(k) \propto k^{n_\mathrm{s}} T^2(k) D^2(z) \tag{3.1}$$

D is the growth factor of linear density perturbations independent of scales, n_s is the scalar spectral index. $T(k)$, the transfer function, describes the influence of different times of horizon crossing for the different wavelengths of fluctuations. Transfer functions can be computed by solving the Boltzmann equations in the early universe numerically. The most prominent code for this is CAMB (Lewis et al. [50]). For simplicity, we use fits to the transfer function by Eisenstein and Hu [18].

The power spectrum is sampled in Fourier space by an overdensity field δ:

$$\delta_\mathbf{k}(\mathbf{k}) = \sqrt{P(k)}\,\mu_\mathbf{k}(\mathbf{k}) \tag{3.2}$$

where μ is a Gaussian distributed random field with mean of zero and a variance of one. The transformation to real space implicitly assumes periodic boundary conditions, which we also employ in the subsequent evolution of the initial conditions.[1]

Using first order Lagrangian perturbation theory, we can compute positions and velocities of particles sampling the density field:

$$\mathbf{r} = \mathbf{q} + \mathbf{L}(\mathbf{q}) \tag{3.3a}$$

$$\dot{\mathbf{r}} = \dot{\mathbf{L}}(\mathbf{q}) \tag{3.3b}$$

$\mathbf{q}$ is the non-displaced or initial position and $\mathbf{L}$ is the displacement field. Dark matter particles are initially placed on a homogeneous grid and afterwards displaced according to this description. In practice, many codes, including MUSIC, use second order perturbation theory because it increases accuracy, especially for higher order moments of the density probability distribution function [28].

The displacement field is given by Zel'dovich [117]:

$$\mathbf{L}(\mathbf{q}) = \nabla_\mathbf{q}\Phi(\mathbf{q}). \tag{3.4}$$

---

[1] We note that [28] prefer to sample both the white noise field and the transfer function in real space. They claim this helps in getting the two-point correlation function right.

We note that $\mathbf{L} \propto D(z)$ is time-dependent. This ensures that equation 3.3b does not vanish.

The potential Φ (which is proportional to the gravitational potential) is calculated by:

$$\Delta_{\mathbf{q}}\Phi(\mathbf{q}) = -\delta(\mathbf{q})\,. \tag{3.5}$$

In this way, cosmological initial conditions for particles are computed. For the dark matter which we model as particles using a particle mesh approach we sample the position and velocity field given by the equations 3.3. For Eulerian fields, like the density in AMR codes, initial conditions generation is more complex. Hahn and Abel [28] show that one can not simply use the overdensity field $\delta_{\mathbf{k}}$ because it is inconsistent with the dark matter density, since this is generated using Gaussian distributed displacements and therefore non-Gaussian. Their solution is what they call Local Lagrangian Approximation:

$$\rho(\mathbf{q}) = \frac{\bar{\rho}}{\det\left[\delta_{ij} + \frac{\partial L_i}{\partial q_j}\right]}\,, \tag{3.6}$$

which was derived by formally evolving the continuity equation for a fluid element.

Additional complexity arises when initial conditions for more than a single grid are generated. For example, the white noise field on the finer levels has to be constructed in a way that it is consistent with the field on coarser ones. For the corresponding details, we refer to Hahn and Abel [28]. An example of nested initial conditions generated using their code (as well as the infrastructure described in the next chapter) is shown in figure 3.1.

3.2 Implementing zoom-in simulations in Nyx

The task of building an infrastructure for cosmological zoom-in simulations in Nyx can be split into three parts: First, the initial conditions generated by MUSIC have to be written in a format that Nyx can read. Second, Nyx has to be able to read initial conditions with several levels and at last we have to make sure that the regions for which we have refined initial conditions are never derefined. In this section we explain how we solved each step.

The first step was to extend MUSIC with a new output plugin for Nyx, similar to existing output plugins for several codes like Gadget, Enzo and ART. The central technical problem is the data format used by Nyx: It is a binary format only used by BoxLib-based codes. At this point we had three choices: Use a different, but simple file format, write our own implementation of the BoxLib-file format or link against BoxLib. The first one has the disadvantage that parallel reading in Nyx is difficult. The second is prone to errors and the third is technically complex, since

BoxLib is not a library, but a framework coming with its own build system. This build system had to be adapted to be usable with the MUSIC build system in a portable way. The solution was to select the BoxLib-specific object files required by MUSIC. The compilation of these object files is handled by the BoxLib make system. The MUSIC make system is then given a list of object files to link against. This rather complex solution is rooted in the fact that more than thirty files from BoxLib have to be compiled. The Nyx initial condition files are written by MUSIC in the usual VisMF format, which can also be read by visualization tools like VisIt[2].

Additionally, MUSIC was adapted to generate only grids divisible by the blocking factor. Since BoxLib is based on block-structured AMR, a grid with dimensions of blocking factor cubed is the smallest building block of a BoxLib grid and each grid consists of multiples of this building blocks.

Similar to the other output plugins, we wrote generators for all necessary parameter files. This significantly simplifies setting up a simulation, since all parameters are automatically set consistently with the initial conditions and for most general parameters reasonable defaults are defined. Moreover, it is ensured that the correct unit conversion factors and powers of scaling factors are used.

Although Nyx had an infrastructure for reading and setting up cosmological initial conditions earlier written by the author of this thesis, some significant changes had to be made, since the original methods were only capable of reading single-level initial conditions.

The algorithm works as follows: One level is read in and the grid based quantities are set using the input data. The dark matter particles are created in cell centers and are given displacement and velocity information using the initial conditions. The particle creation is restricted to regions which are not refined. The particle mass is adapted according to the grid scale since on every level one particle per cell is created and the cells on the finer levels are smaller. If a particle is shifted by the initial displacement into the refined region, we replace the particle with eight particles with a mass of one eighth (assuming a refinement factor of 2). This approach is repeated for every level. Since the non-base levels fill only a part of the domain, we obtain a hierarchy with ever smaller particles which only fills the domain if projected to the base level.

Finally, the algorithm for the placement of grids in BoxLib had to be adapted. Originally, it was able to run with a predefined grid setup or to determine the grid structure using refinement conditions. For nested initial conditions one usually wants both: Refined initial conditions (which are fixed) and dynamical additional refinement. Furthermore, refinement in the BoxLib framework is constrained by several obligatory rules. One example is that the coarse-fine boundary of level n to $n+1$ has to be surrounded by a minimum number of cells on level n, which is given by the blocking factor. This prevents large changes of the resolution scale

---

[2] `http://visit.llnl.gov`

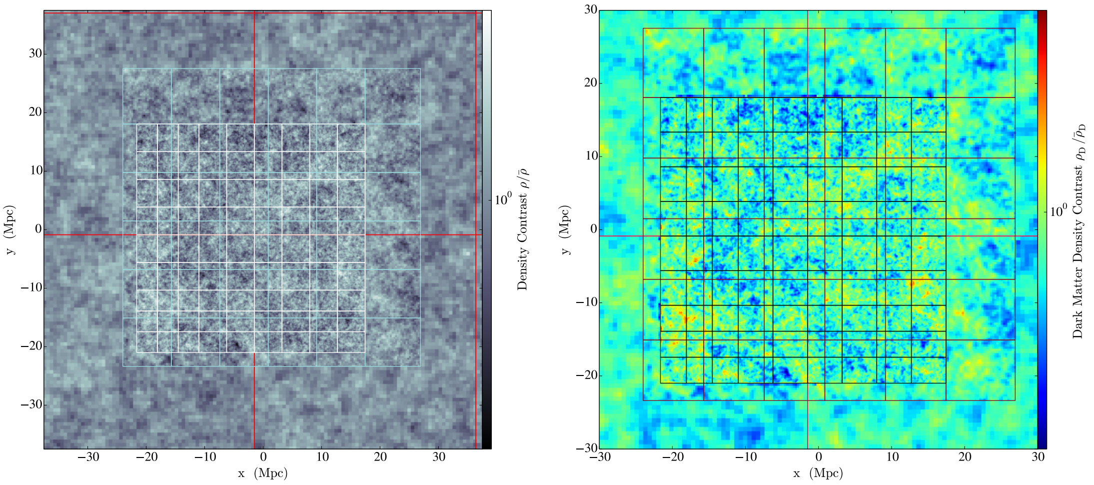

(a) Baryonic density contrast.

(b) Dark matter density contrast.

Figure 3.1: This figure shows nested initial conditions for baryonic and dark matter density at a redshift of $z = 99$.

over short distances. Or in other words: Two subsequent coarse fine boundaries have to be spaced by at least one grid block. To make sure that valid grids are used, we feed the fixed grids into BoxLib's grid placing algorithm. Consequently, the code does not differentiate between grids generated by tagging and the grids generated by MUSIC.

For performance reasons, the tagging of cells for refinement is only done for levels above the fixed grids. Since the algorithm in principle allows for refinement in regions that are not covered by the fixed grids, we explicitly disallow refinement in certain regions by clearing the tags. Tagging is forbidden everywhere apart from the regions covered by fixed grids on a particular level minus the buffer area of one blocking factor in each direction.

Figure 3.1 shows a slice of initial conditions after they have been read in and treated according to the prescription above. The level 0 grids are shown in red, the level 1 ones in pale green and the level 2 ones in white. One can clearly see the buffer area between level 1 and 2.

3.3 Potential applications

By now, the capability for reading MUSIC initial conditions has been used in a number of projects, but most of them only use the single grid initialization. Fixed initial grids have only been used in two projects, firstly in our participation in

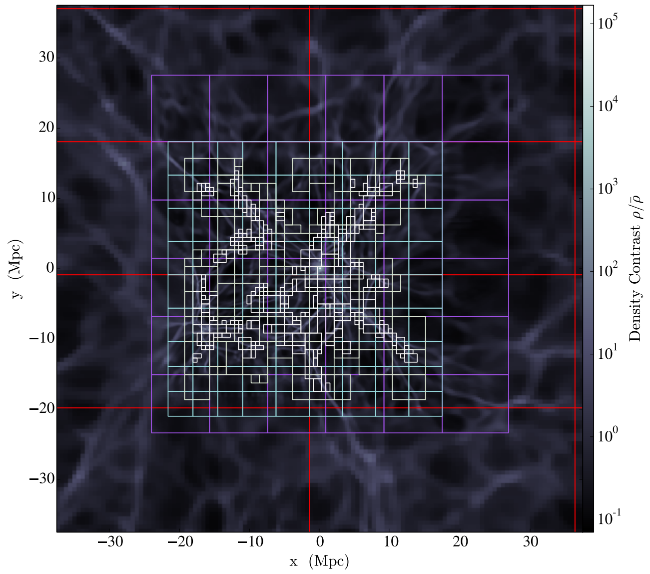

(a) Baryonic density contrast

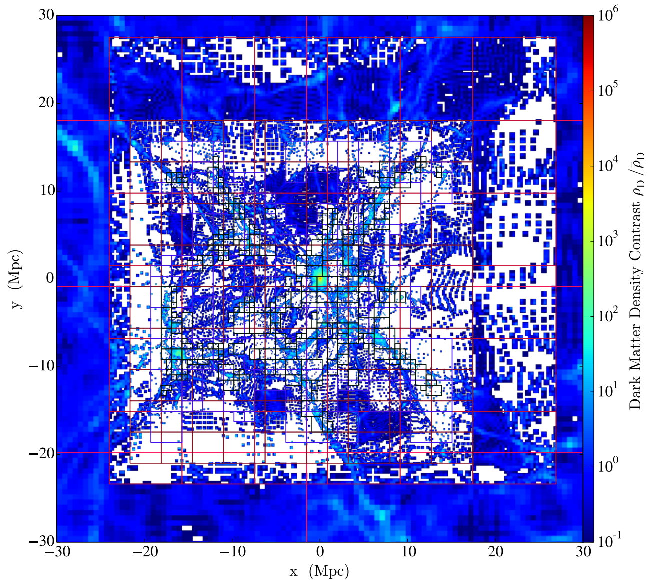

(b) Dark matter density contrast

Figure 3.2: This figure shows the initial conditions from figure 3.1 evolved to $z = 2$. Note that the colorscheme for (a) was chosen with a focus on the grid structure: You can clearly see the fixed grids and the added refinement. (b) highlights a central problem of particle mesh simulations using particle mesh: empty cells. For a detailed discussion see the text.

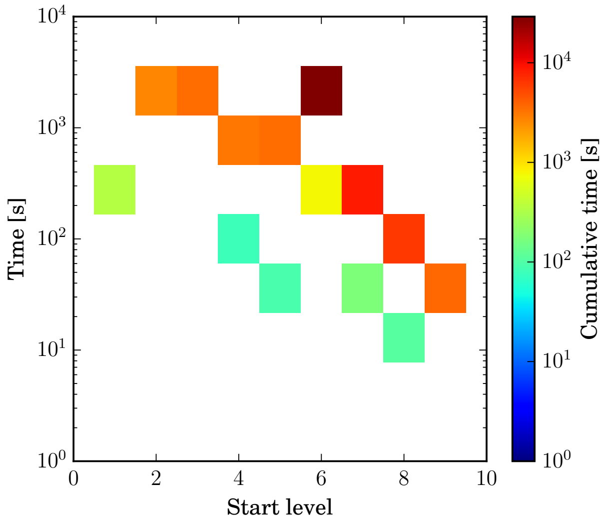

Figure 3.3: This figure shows a histogram of the times spend in the grid placement routine during one timestep in dependence of the level on which the placement routine is started (start level). The increase of occurences with increasing level number is due to the fact that we employ AMR with subcycling and do a regrid every two iterations on each level.

the AGORA code comparison project and secondly in a project performing cluster simulations by Schmidt et al. [93]. Additionally, this work also employs single-level initial conditions generated using MUSIC. While the second one demonstrated the basic applicability, the first one only gave insights into the needs for necessary optimisation of the BoxLib implementation. In this section we will discuss both projects and their results shortly.

3.3.1 AGORA code comparison project

The AGORA code comparison project [42] aims at comparing well-resolved (several 100 pc) galaxy simulations among different codes used by the astrophysical community. Since Nyx is a relatively new cosmology code with an advanced treatment of hydrodynamics, we wanted to take part in the comparison and study the impact of the unsplit hydro solver, particularly with regard to disk instabilities and turbulence.

For this, we ran the initial conditions described in [42]. For convenience, we list the key settings here: The simulation includes only dark matter in a box with a length of 85.47 Mpc and five levels of initial refinement generated using MUSIC at a redshift $z = 100$. The simulation is to be run to $z = 0$ using seven additional levels of refinement which makes 12 levels in total.

We stopped the simulation at $z \approx 10$, since already there a time step took about

max. level	fraction
5	1.1%
6	3.9%
7	25.2%
9	93.9%

Table 3.1: This table shows the fraction of the runtime of a coarse timestep that is spent for the grid placement routine depending on the finest level in the simulation. The values were taken in a simulation that was adding the grids because of progressing structure formation in the timestep before an additional level was added. In a simple model one may assume that the time needed for grid placement as well as the time needed for the time evolution scales with the number of cells. Since there might be additional effects, conclusions from this values should be drawn with caution.

18 h, although the maximum number of refinement levels was not reached yet. This runtime is obviously unfeasible. In the remainder of this section we discuss the probable causes for the inefficiency. First of all, our experience with various simulations showed that BoxLib-based codes become inefficient if one sets up more than 6 levels. For the AGORA runs performed with Nyx, this is shown in table 3.1. It is striking that at a higher number of levels most of the time is spent in the subroutine responsible for grid placement. This routine is part of the regridding that is started on each level every two iterations. It acts on a start level and all deeper levels.

The distribution of execution times for calls to the grid placement subroutine is shown in figure 3.3. The figure shows a 2d histogram of the run time with respect to the lowest level that is regridded (start level). As one would expect, the runtime decreases with increasing start level, simply because there are less grids to take care of. Apart from this trend, we see that there is a large scatter in the distribution, for example for start level 5 some calls need around 20 s while the majority needs around 450 s. The reason for this is unknown.

Since the runtimes presented here have been measured using only a moderate number of cores, one might attempt to solve the problem by largely increasing the computational power. However, this does not help, because grid placement is not parallelized. Using Amdahl's law [2] (which gives a simple estimate of the parallelization gain in dependence of the number of processors used and the fraction of the algorithm which can be run in parallel) and assuming all other parts of the code to be fully parallelized, increasing the number of cores by a factor of two would decrease the runtime by only about three percent.

The natural way forward would be to optimize the grid placement algorithm. Since this algorithm is very complex and the time to achieve significant improvements was highly uncertain, we decided to stop the project at this point. An additional argument was that even if this problem could be overcome, it was unlikely that performance issues in deeply refined simulations would be fully resolved, especially compared to codes that have been optimized for this task, such as Enzo. Furthermore, the main project described in this thesis does not depend on very deep refinement.

3.3.2 Cluster simulations

In this section we briefly discuss cluster simulations performed by W. Schmidt et al. for which my work on nested initial conditions helped to achieve higher resolution for a selected cluster. After briefly summing up the methods and results published in Schmidt et al. [92], we give preliminary results of an additional publication in preparation [93]. The cluster simulations use the methods described in chapter 2 and 3: e.g. cosmological simulations of dark matter and baryons using primordial radiative cooling and heating and the shear improved turbulent subgrid model. Both [92] and [93] use initial conditions generated with MUSIC and thereby the methods developed here, but only the second suite of simulations uses nested initial conditions.

Schmidt et al. [92] aim at understanding the relation between turbulent to internal energy in galaxy clusters. While cooling is taken into account the authors neglect stellar feedback and the influence of active galactic nuclei. Using the novel estimation of the turbulent velocity dispersion, we show correlations between the internal energy and the turbulent velocity dispersion. This is also analyzed with respect to the halo mass.

In a follow-up project, [93], we simulate the cluster with the most massive halo with four times higher resolution using nested initial conditions. In figure 3.1 and 3.2 we show slices of initial conditions and final density distribution taken from a test simulation for that project.

Figure 3.2b shows a general problem of particle mesh methods using attractive forces: The particles tend to concentrate in some cells. If the distance between particles gets larger than the smoothing length of the interpolation scheme, some cells become empty. In cosmological simulations, this unavoidably happens in strongly underdense regions and leads to tracelike patterns in the dark matter density distribution.

This problem gets more pronounced if refinement is introduced: If a particle crosses a coarse-fine boundary, the width over which it is interpolated is reduced by the refinement factor. This effect can clearly be seen at the level 0 to level 1 boundary in the top and in the right part of figure 3.2b. Figure 3.2b shows large regions with zero dark matter density and very steep gradients, which is not very physical. This effect could be reduced by using more particles, but is not a large problem, since most simulations focus on the baryonic density. The baryonic matter couples to the dark matter via gravity only. Due to the low-pass filtering nature of the Poisson equation, the gravitational potential is smooth, regardless of the steps in

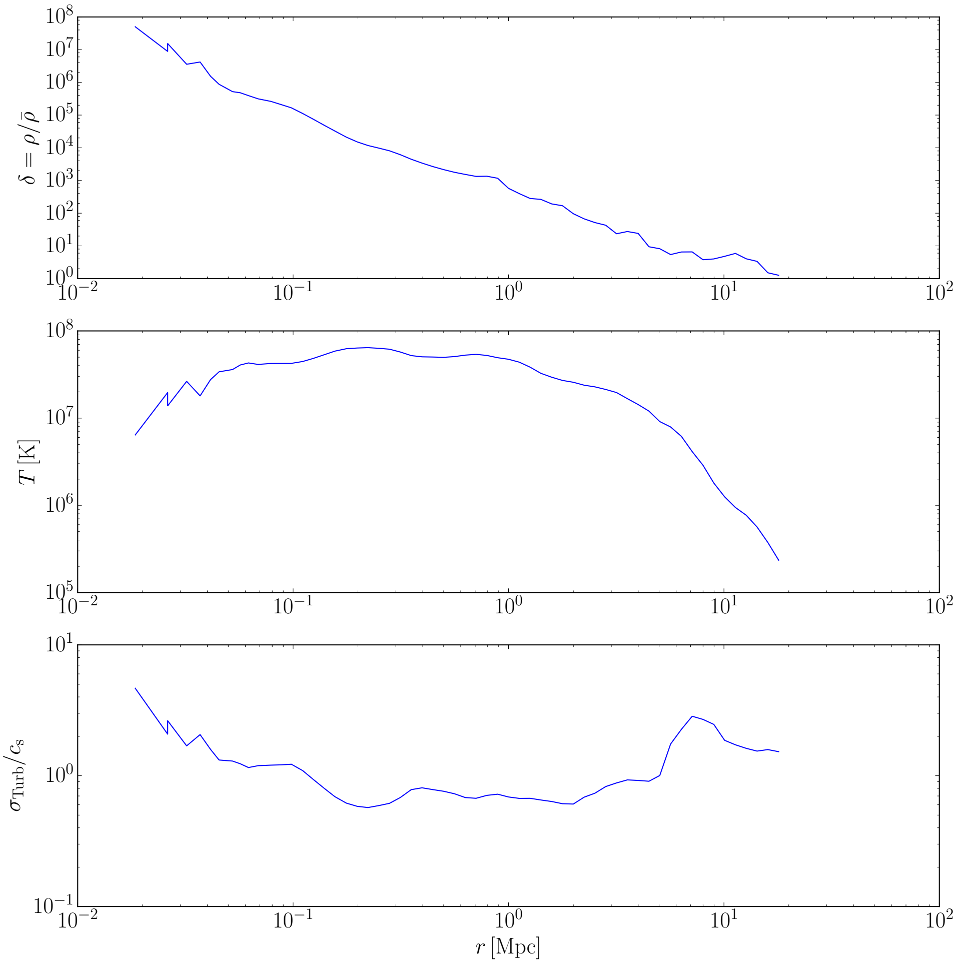

Figure 3.4: This figure shows profiles of the central cluster at $z = 0$ in a simulation using nested initial conditions. The data is taken from [87] and the cluster halo corresponds to halo 1 in [92]. The upper panel shows the overdensity δ, the central one the temperature T and the lower one the turbulent Mach number $M_{\mathrm{turb}} = \sigma_{\mathrm{turb}}/c_{\mathrm{s}}$.

the dark matter density. Therefore, the effects on the baryonic matter are small. This can also be seen in figure 3.2a.

In figure 3.4 we show representative radial profiles of the cluster. One can see a power-law decline of the overdensity in the upper panel. In the central panel one sees that the temperature is $\gtrsim 10^7$ K over very large radii extending far beyond the intracluster medium. This is caused by shock heating in the cluster outskirts. In the last panel, this is indicated by the steep increase of turbulent Mach number due to accretion shocks at the outer boundary of the cluster. However, the power-law density distribution and the low temperatures in the center of the halo are somewhat unphysical. This can only be solved by employing a star formation and feedback model. In chapter 5 we are going to discuss similar halo profiles for simulations done with the star formation and feedback model presented in chapter 4.

3.4 Outlook

In this chapter we have discussed cosmological initial conditions with a focus on zoom-in simulations and Nyx. We identified problems with parts of the code and discussed ways to solve them, but also showed that there are situations in which the zoom-in approach is applicable.

In the remainder of this work, we only employ single-level initial conditions. The main reason is that we are interested in the evolution of all haloes in the box. Furthermore, single-level initial conditions are sufficient for our resolution requirements.

4 Methods for simulations of galaxy formation

Hope is more than a postponed disappointment
— Epica, *Kingdom Of Heaven*

In this chapter, we discuss methods needed for simulations of galaxy formation. Compared to the methods described in chapter 2, this chapter mostly adds models for small scale physics. The methods given in chapter 2 are sufficient to simulate the intergalactic medium, whereas this work focusses more on galaxies and the circumgalactic medium. Furthermore, the methods presented in chapter 2 already existed when this work was begun while the methods in the following remained to be developed. We note that previous simulations in the literature use methods similar or identical to the ones described in sections 4.1–4.4, while the approaches in section 4.5 and 4.6 are new.

4.1 Metal cooling

In section 2.6, we discuss heating and cooling for the primordial species. Since star formation is producing a non-negligible amount of metals, these might give a relevant contribution on heating and cooling rates. Wiersma et al. [113] find that including metals changes the cooling rates by up to one order of magnitude. Furthermore, they claim that photoionization is equally important. Additionally, Smith et al. [99] find that omitting metal cooling results in a significant decrease of star formation.

Despite its importance, metal cooling is preferably ignored since it is hard to compute. Wiersma et al. [113] consider the eleven most abundant elements (H, He, C, N, O, Ne, Mg, Si, S, Ca, Fe) with countless species. Their evolution can not be computed on the fly, instead most of the literature uses precomputed heating and cooling rates. Specifically, we employ rates by Wiersma et al. [113] and Oppenheimer and Schaye [69]. Both compute the rates using Cloudy Version 10.00 [21, 22] while assuming (as we do for the primordial cooling in chapter 2) dust-free and optically thin gas in ionization equilibrium. They also expose the gas to an uniform ultraviolet background and the cosmic microwave background. Since the rates in Wiersma et al. [113] use the outdated Haardt and Madau [26] model for the UV background, we use the updated rates by Oppenheimer and

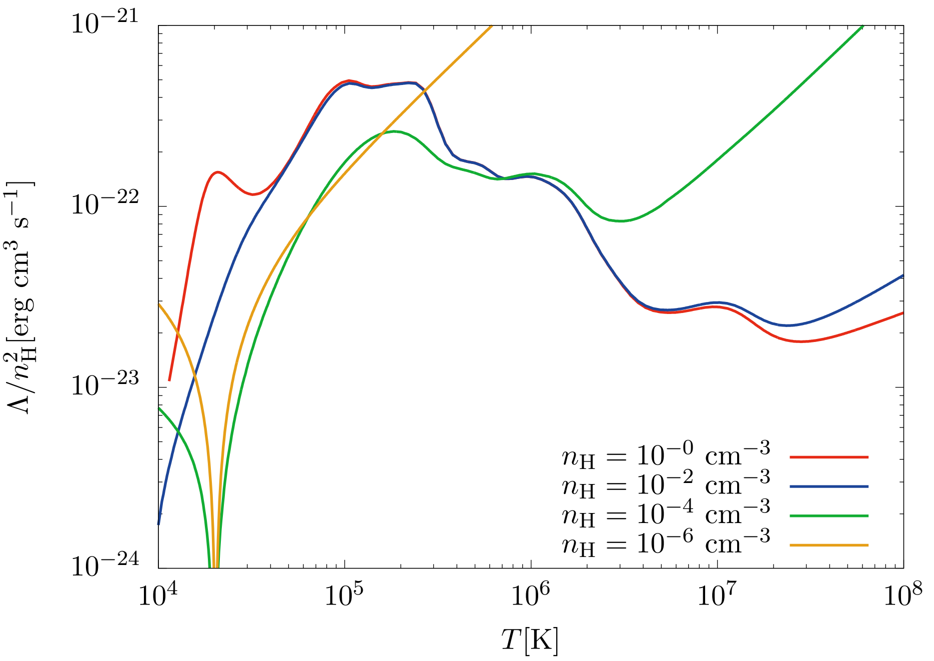

Figure 4.1: This figure shows the net cooling rates for the primordial plus metal cooling network at $z = 3$. This plot employs the same parameters as figure 2 in [113], to which it can be compared. The minor differences are due to the fact that we did not use their tabulated data, but instead the updated rates by Oppenheimer and Schaye [69].

Schaye [69], which assume the Haardt and Madau [27] radiation background. Their rates are tabulated for each element and combined for all elements with respect to temperature, hydrogen density, and redshift. We interpolate these values using a trilinear method. Since we only make use of one metallicity field, i.e. the ratios of the elements heavier than helium are assumed to be solar, we apply the combined net cooling rates.

The total net cooling rate Λ then becomes (eq. 5 in Wiersma et al. [113]):

$$\Lambda = \Lambda_{\mathrm{H,He}} + \Lambda_{Z_\odot} \frac{n_e/n_H}{(n_e/n_H)_\odot} \frac{Z}{Z_\odot}. \tag{4.1}$$

Herein, $\Lambda_{Z_\odot}$ is the interpolated value, and $\Lambda_{\mathrm{H,He}}$ denotes the value obtained from the primordial cooling network. We neglect the $(n_e/n_H)/(n_e/n_H)_\odot$ term in that equation. Wiersma et al. [113] state that this leads to errors of less than factor 3. Furthermore, they report that, for the collisional ionization equilibrium case, the difference of cooling rates between different codes is a factor of 2. This justifies our simplification.

We have thoroughly tested our implementation. For illustrative purpose, we show the net cooling rates for the full network in figure 4.1.

4.2 Star formation

This section explains the star formation prescription used in this work. We start by giving a small introduction into star formation (see Mac Low and Klessen [54] and Hennebelle and Falgarone [30] for detailed reviews of the physics of star formation, which we broadly follow) and the theoretical approaches relevant here. In the course of this section, the focus shifts more and more to numerical aspects of star formation modelling.

Star formation is complicated and not well understood, due to the high number of competing processes. Speaking generally, star formation happens when gravity overcomes the support by thermal and turbulent pressure and, to a lesser degree, magnetic fields. Modern theories focus on supersonic turbulence as a key ingredient to star formation and its regulation: On the one hand, turbulence supports the gas against collapse while, on the other hand, turbulent density enhancements (mostly via shocks) trigger a self-amplifying loop of radiative cooling and gravitational collapse. The turbulence is thought to be sourced by supernova explosions and galactic rotation. Additionally, merging events generate a lot of turbulence and often trigger a starburst. Furthermore, we note that the molecular clouds in which star formation happens exhibit a two-phase structure, with a cold phase from which stars are formed and a warm phase. These molecular clouds are of parsec size, whereas actual stars are smaller by several orders of magnitude. This set of arguments requires the star formation to be treated by a subgrid model. In simulations of galaxy formation, the different phases of the interstellar medium are often treated by multiphase models, see, for example, Springel and Hernquist [101] and Braun and Schmidt [6]. However, these models require resolutions that we can not reach.

4.2.1 The initial mass function

One important aspect of the description of star formation is the initial mass function (IMF). It gives the number of stars per mass bin $\partial N(m)/\partial m$ before stellar evolution (and, with it, mass loss) sets in. It is widely assumed that the basic structure of the IMF is universal, at least for present-day galaxies. Determination of the IMF by observation is pretty complicated, and a full theory of it might not exist [54].
Our model employs the IMF only in the feedback part, which is described in section 4.3. Nevertheless, we discuss it in the context of star formation.

A popular choice is the Chabrier [13] IMF, which we adopt here:

$$\xi(m) = \frac{\partial N}{\partial m} = \begin{cases} \frac{1}{m} 0.158 \exp\left(-\left(\frac{\log(m)-\log(0.079)}{\sqrt{2}\cdot 0.69}\right)^2\right) & m < 1\ \mathrm{M}_\odot \\ 4.43 \cdot 10^{-2} m^{-2.3} & m > 1\ \mathrm{M}_\odot . \end{cases} \tag{4.2}$$

We normalize the IMF by computing the mean while assuming a minimal and a maximal mass of 0.1 $\mathrm{M}_\odot$ and 100 $\mathrm{M}_\odot$, respectively:

$$\langle m\xi \rangle = \int_{0.1\ \mathrm{M}_\odot}^{100\ \mathrm{M}_\odot} m\xi(m)\,\mathrm{d}\,m, \tag{4.3}$$

$$\tilde{\xi} = \frac{1}{\langle m\xi \rangle}\xi. \tag{4.4}$$

Note that the unit of the normalized IMF $\tilde{\xi}$ is $\frac{1}{\mathrm{M}_\odot^2}$.

The lower mass limit is the transition mass from ordinary stars to brown dwarfs. In contrast, the value of the upper mass limit is in some sense arbitrary. Our choice follows Pallottini et al. [71] and Vogelsberger et al. [111].

4.2.2 Star formation laws

Theoretical/empirical star formation laws

Star formation laws describe the amount of stars produced. From observations, we have an empirical relation specifying the star formation rate column density $\dot{\Sigma}_*$ of galaxies as a function of the baryonic column density Σ_B, the Kennicutt-Schmidt law [41, 86]:

$$\dot{\Sigma}_* = \tilde{A}(\tilde{b} \cdot \Sigma_\mathrm{B})^{\tilde{N}} \tag{4.5}$$

with an exponent $\tilde{N} = 1.4$, a normalization factor $\tilde{A}$ and a factor $b = 1\ \mathrm{M}_\odot^{-1}\mathrm{pc}^2$ to get the units correctly (cf. [83]). The problem with this kind of law is that it employs column densities instead of volume densities, which are needed in theoretical as well as in numerical models. Instead, many models employ a Schmidt law [86] of the form:

$$\dot{\rho}_* = A\left(b \cdot \rho_\mathrm{B}\right)^N, \tag{4.6}$$

using definitions analog to the ones in equation 4.5. Even more widely adopted is the theorically expected form:

$$\dot{\rho}_* = \epsilon_\mathrm{FF}\frac{\rho_\mathrm{B}}{t_*} \tag{4.7}$$

in which ϵ_FF is an efficiency parameter and in which one can set the star formation time scale t_* to the free-fall time t_FF[1]:

$$t_\mathrm{FF} = \frac{1}{\sqrt{4\pi G\rho}}. \tag{4.8}$$

---

[1] We note that this choice of constants is rather unusual, it probably goes back to [51]. The more common form is $t_\mathrm{FF} = \sqrt{3\pi/32G\rho}$ (e.g. [46]). Nevertheless, we stick to the above definition for historical reasons and point the reader to the fact that the only change would be a renormalization of ϵ_FF by $\sqrt{8/3\pi^2} \approx 0.45$.

This is the description we are going to use as it is also employed in most of the coarsely resolved simulations in the literature [33, 99]. For simulations with subgalactic resolution, a broad range of refinements exists, which may have a significant influence [7].

The similarity between equation 4.7 and 4.8 becomes clear as soon as one inserts the free-fall time into the star formation law. This leads to an exponent in the Schmidt-law of $N = 1.5$. It is tempting to neglect the difference between N and $\tilde{N}$ but one should be aware that the conversion involves a smoothing scale. Schaye and Dalla Vecchia [83] derive analytic relations between the two laws, assuming the Jeans scale of the diffuse neutral gas as smoothing scale, which coincides with the scale height of galaxies (a few hundred parsec). Using this for a Kennicutt-Schmidt law with $\tilde{N} = 1.4$, they obtain $N = 1.2$. In the case of starting with the volume density parameter $N = 1.5$ as found in the free-fall model, they calculate $\tilde{N} = 2$, which is not compatible to the observed value $\tilde{N} = 1.4$. At this point, we should note that in our simulations with a resolution of $\Delta x \approx 10$ kpc, we do not resolve the corresponding scales, therefore the smoothing scale in our problem is dependent on the resolution of the simulation.

Another important parameter is the star formation efficiency. In the literature, its value is usually estimated as $\tilde{\epsilon}_{\mathrm{FF}} = 0.01$ (e.g. [45]). Once again, the literature value is based on column densities, so we can not directly use it as an input. Furthermore, since we do not resolve the relevant scales, we introduce the grid scale as smoothing scale. This makes the efficiency dependent on resolution. Therefore, we treat it as a free input parameter[2].

Implemented star formation law

Given the star formation laws discussed above, this section is devoted to calculating the star formation density in a cell. As indicated above, we use equation 4.7 and 4.8. Since stars are modelled as stellar populations represented by a star particle, we need to calculate the mass of stars formed in a cell during a time step Δt. For this, we use a simple integration scheme, assuming a constant slope during the time step:

$$\langle n \rangle = \frac{\rho_{\mathrm{B}} (\Delta x)^3}{m_*} \frac{\Delta t}{t_*}, \tag{4.9a}$$

$$m_* = \delta_{\mathrm{SF}} \cdot \bar{\rho}_{\mathrm{B}} \cdot (\Delta x_{\mathrm{min}})^3, \tag{4.9b}$$

$$t_* = \frac{t_{\mathrm{ff}}}{\epsilon_{\mathrm{ff}}}. \tag{4.9c}$$

In this set of equations (which is basically a reformulation of equation 4.7 and 4.8), $\langle n \rangle$ is the mean number of stellar ensembles with mass m_* formed during a time step, and δ_{SF} refers to the overdensity needed to form stars (see above). The

---

[2] We note that Pallottini et al. [71] present a similar argument for their parameter t_*.

introduction of a mean number of stars becomes plausible as soon as we introduce the concept of stochastic star formation. This approach is widely used in the literature [31, 68, 71, 83, 84, 101, 111]. Sampling star formation stochastically can be motivated in two ways: First, star formation driven by supersonic turbulence is stochastic by nature. Second, the stochastic process produces more stellar mass at once (but more rarely), which is favorable in many numerical setups.

Our approach follows Pallottini et al. [71] with regard to the stochastic parts but replaces their constant star formation timescale t_* by the free-fall time. As random distribution, they (and consequently we) use a Poisson-distribution since it describes the number of occurences in a time span for events that are independent and happen with a given rate:

$$P(n) = \frac{\langle n \rangle}{n!} \exp\left(-\langle n \rangle\right) \tag{4.10}$$

We sample the distribution using inversion by sequential search [15]. This particular algorithm is fast for small $\langle n \rangle$ (which we find to be the case for most star forming cells) and consumes only one random number. The random numbers are generated using a Merssenne Twister. To get some kind of repeatability, we initialize the Mersenne-Twister only at the beginning of the simulation and keep its internal state in the checkpoints.

Given a Poisson-distributed number n, the resulting stellar mass is:

$$m_{\text{formed}} = n \cdot m_* \tag{4.11}$$

This approach is similar to recipes employed by [31, 68].

We note that this kind of star formation recipe is not fully deterministic, despite the efforts described above. The reason is that random numbers are drawn on all processors on a patch-per-patch and cell-by-cell basis. Therefore, a change in the grid distribution leads to a change in the random numbers. If OpenMP is used it gets even less predictable: If a patch has more than one cell in which star formation is allowed, the sequence in which the random numbers for the cells are drawn is not determined.

Furthermore, the non-continous nature of stochastic star formation leads to some kind of noise in the simulation, which manifests itself in the star formation rates.

4.2.3 Star formation criteria

It is obvious that the Kennicutt-Schmidt law does not hold in regions with arbitrarily low densities. Therefore, Schaye and Dalla Vecchia [83] assume a column density threshold of $3\,\mathrm{M}_\odot\mathrm{pc}^{-2}$, which corresponds (using their assumptions) to a density of $8 \cdot 10^{13}\,\mathrm{M}_\odot/\mathrm{Mpc}^3$. Again, we note that this quantity is resolution-dependent since collapse is inhibited near the grid scale. Consequently, we employ the following criteria:

Overdensity All cosmological simulations use a density criterion for star formation. In contrast to the suggestions by Schaye and Dalla Vecchia [83], most of them employ an overdensity criterion [33, 40, 71, 99]. This criterion is sensitive to the comoving density and not to the physical density. We also use this approach and allow star formation in cells with

$$\rho > \delta_{\mathrm{SF}}\bar{\rho} \tag{4.12}$$

Finest level Additionally, we restrict star formation to the finest level of our simulation. This is done mostly for technical reasons. Since we refine on density in all our simulations, we can safely assume that this criterion does not have an influence.

In the literature, there is a number of additional criteria, which we do not adopt, similar to the approach used in Ramses [17, 71]. Nevertheless, it is worth discussing them and finding out whether they have a significant influence on star formation. Our results on simulations using additional criteria are presented in section 5.2.5. As we will discuss there, some do have a significant influence. Nonetheless, we stick to the most simple formulation of star formation, since the focus of this work is on exploring turbulent effects connected to stellar feedback, where complicated star formation laws might be a distraction.

The selection of additional criteria follows Cen and Ostriker [12] but is representative.

Converging flow This criterion restricts star formation to cells in which the divergence of the velocity is negative. The motivation for this goes back to the fact that star formation is inherently a collapsing phenomenon.

Thermal restrictions Stars form from molecular gas, which shows temperatures of around 10 K. Since most simulations do not follow the hydrogen chemistry needed to obtain these low temperatures, the criterion is set to the temperature where the combined cooling rate drops. This happens at about $5 \cdot 10^4$ K, which is often used as a threshold for star formation.
Cen and Ostriker [12] extend this criterion by also checking whether the cooling time is smaller than the free fall time. If this is the case, they allow star formation, too.

Unstable against gravity Cells that are unstable against gravity, having a Jeans length[3] smaller than the cell size, are no longer well-resolved in the simulation. Therefore, it is customary to transfer mass to a subgrid prescription of star formation. Additionally, star formation depends on gravitational collapse. As we will see later, this criterion is the only one having a significant influence on the star formation rate.

---

[3] The Jeans length scales with $\lambda_{\mathrm{J}} \propto \sqrt{T/\rho}$.

In this section, we have explained under which conditions our simulation forms stars. The star formation model has two free parameters: δ_{SF} and ϵ_{FF}. Their meaning and influence is discussed in section 5.2.3.

4.3 Stellar feedback

In this section, we explain the feedback model used in this work. Stellar feedback refers to the fact that stars return metal-enriched matter, radiation, and momentum to the surrounding medium. Initially, an overview of the feedback processes of stars differentiated among mass groups is given. This part closely follows Portinari et al. [77].

Low and intermediate mass stars with masses $M \lesssim 5\ \mathrm{M}_\odot$ loose their envelope by stellar winds in a terminating asymptotic giant branch (AGB)-phase and end up as white dwarfs. These stellar winds are the most important source for enriching the interstellar medium although the momentum of the expelled gas is very low.

Quasi-massive stars with masses $6\ \mathrm{M}_\odot \lesssim M \lesssim 8\ \mathrm{M}_\odot$ become unstable to the electron capture instability and terminate in a supernova.

Massive Stars with masses $9\ \mathrm{M}_\odot \lesssim M \lesssim 120\ \mathrm{M}_\odot$ are the progenitors of classical Type II supernovae. Their remainders are neutron stars or black holes.

Very massive stars with even larger masses are pulsationally unstable and undergo a heavy mass loss during their life time. Since this kind of stars is quite rare, we do not consider it here.

Summing up, we note that low and intermediate mass stars are an important source of metals, while their momentum of expellation is not sufficient to drive material out of the galaxy. In contrast, quasi-massive and massive stars contribute less metals, but end in supernovae, which are very important for pushing material into the sourroundings of a galaxy. Accordingly, we assume in our model that supernovae are the dominant mechanism for expelling gas enriched by a combination of supernovae and stellar winds from AGB-stars.

In fact, stellar feedback, be it winds or supernovae, happens much below the grid scale in simulations of cosmological structure formation or galaxy formation. For this reason, they are treated by models. When looking at the literature, one finds a tremendous variety of those. Variations can be found in the description of the amount of feedback, its temporal distribution, and in the methods of transferring the feedback to the gas. The remainder of this section is organized according to these three aspects.

4.3.1 Temporal distribution

The description of the temporal distribution of feedback varies in the literature from the instantaneous recycling approximation [71, 107] (emitting all feedback immediately when stars are formed) over ad hoc functional descriptions (mostly Schechter functions with $\alpha = 1$ [85]) [12, 99] to prescriptions based on stellar models [111].

The instantaneous recycling approximation is crude, given stellar life times of 10^6 yr up to more than 10^8 yr (see also figure 4.2). Pallottini et al. [71] argue that the time step in their simulation is of the same order. Indeed, in our simulations we find rootgrid time steps in the order of 10^6 years. However, star formation and feedback happen on the finest level, which in our case is evolved with a time step of approximately 10^5 years. Since, apart from its simplicity, there is no argument in favor of the ad hoc variants, we chose to develop our own model based upon stellar models.

For the temporal distribution model, a description of the life time of a star τ is central, which we took from Raiteri et al. [80]. There, the life time of a star is a function of its mass and its metallicity. By inverting it, we obtained the function $M(t, Z)$, which describes the mass of a star dying after a given life time t. Using this and the IMF we can construct the change in the number of stars:

$$\begin{aligned}\frac{\partial N_{\text{Stars}}}{\partial t} &= -\frac{\partial N}{\partial m}\frac{\partial m}{\partial t} \\ &= -\tilde{\xi}(M(t, Z))\frac{\partial M(t, Z)}{\partial t} \cdot M_{\text{population}}. \end{aligned} \tag{4.13}$$

The minus sign is based on convention: We would like to have a positive number (of supernovae) although the number of stars is decreasing.

As mentioned above, the most important feedback process is feedback from type II supernovae. This is relevant for stars in a mass range from 6 to 100 $\mathrm{M}_\odot$ (similar to, e.g., [111]). If we restrict $M(t, Z)$ to that mass range, we obtain:

$$\frac{1}{M_{\text{population}}}\frac{\partial N_{\text{SNII}}}{\partial t} = -\tilde{\xi}(M_{\text{SNII}}(t, Z))\frac{\partial M_{\text{SNII}}(t, Z)}{\partial t}, \tag{4.14}$$

i.e. the number of supernovae per mass as a function of time and metallicity. This function is plotted for different metallicities in figure 4.2.

Since the supernova count depends only weakly on the metallicity, we use a description which is independent of it. As physically not all stars are formed at the same moment, we smoothed the supernova rate function using a moving average[4] over a period of $3.5 \cdot 10^6$ yr. This time scale coincides with the time scale on which

---

[4] The moving average $a(t)$ is given by $a(t) = (\sum_{t_i > t - \Delta t/2}^{t_i < t + \Delta t/2} v(t_i))/(\sum_{t_i > t - \Delta t/2}^{t_i < t + \Delta t/2} 1)$ for discrete values $v(t_i)$ and an averaging period Δt. Here, the term in the denominator is equivalent to the number of points in the averaging period.

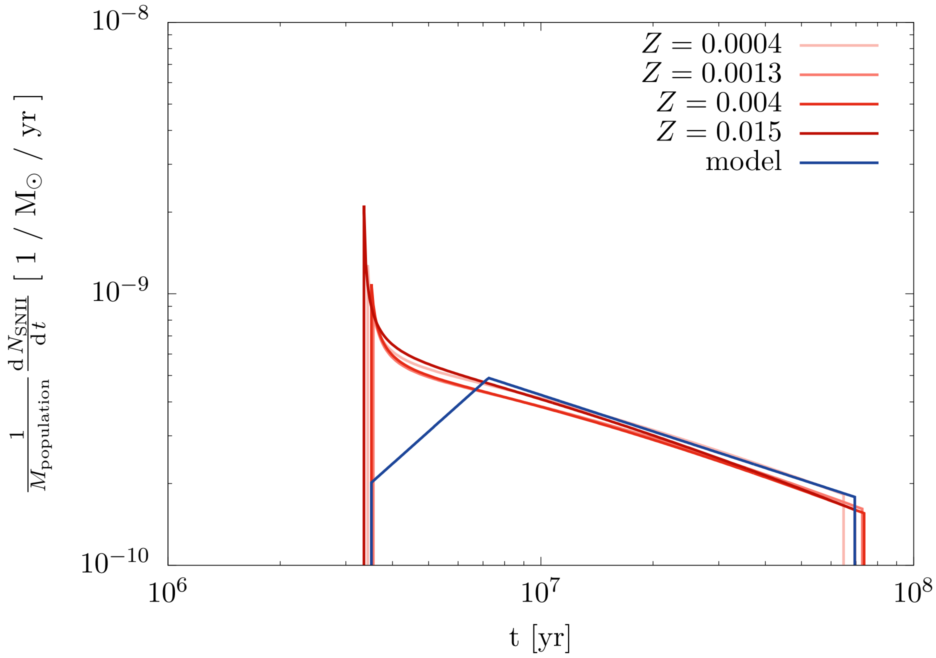

Figure 4.2: Time evolution of events as calculated in equation 4.14 for different metallicities and the final model for the temporal distribution of feedback. The model is based on a moving average of the supernova rate, which results in the slow increase between $3 \cdot 10^6$ yr and $8 \cdot 10^8$ yr. Particular care has been taken to make sure that the integral under both, the data (represented by the $Z = 0.0004$ case) and the model, is the same.

we allow accretion onto star particles (see section 4.4.1 for details) and with the time needed for the first supernovae to go off. To simplify the implementation, we fit a piecewise-defined function to the smoothed function:

$$\frac{1}{M_{\mathrm{population}}}\dot{N}_{\mathrm{SNII,model}}(t) = \begin{cases} t^a \cdot b & 3.5 \cdot 10^6 < t < 7.3 \cdot 10^6 \\ t^c \cdot d & 7.3 \cdot 10^6 < t < 7 \cdot 10^7 \\ 0 & \text{otherwise} \end{cases} \tag{4.15}$$

with

$$a = 1.23, \qquad b = 1.79 \cdot 10^{-18},$$
$$c = -0.45, \qquad d = 5.26 \cdot 10^{-7}.$$

The smoothing cuts off the sharp rise in the number of supernovae at the beginning of feedback. This is also beneficial from a numerical point of view: The slower start allows the hydro-solver to adapt the time step to the starting feedback. Otherwise, the large and spontaneous rise in temperature would result in a more

frequent violation of the CFL criterion and therefore in a crash of the code.
For usage in the subsequent parts of the model, we normalize the function:

$$\dot{\mathcal{N}}(t) = \frac{\dot{N}_{\mathrm{SNII,model}}(t)}{\int \dot{N}_{\mathrm{SNII,model}}(t)\,\mathrm{d}\,t} \tag{4.16}$$

with units yr^{-1}. Furthermore, we note that we need to integrate N to get the number of supernova explosions in a given time step:

$$N_{\mathrm{SNII}}(t, dt) = \int_t^{t+dt} \dot{N}_{\mathrm{SNII}}(t')\,\mathrm{d}\,t'. \tag{4.17}$$

With this at hand, we have a description for the temporal distribution of supernova feedback. This will be used in the following.

4.3.2 Amount of feedback

Analogous to the approach above, we once again use stellar models to determine the parameters of our feedback model. In detail, we want to calculate the following parameters:

- ϵ_{ret}, the fraction of mass that is returned to the gas via feedback.
- ϵ_{Z}, the fraction of metals in the returned mass.
- e_{ret}, the feedback energy per unit of returned mass.

Our approach is conceptually similar to those described in [71, 111] and various others.

As a first step, we derive the fraction of gas fed back to the interstellar medium (which we call $f_{\mathrm{ret}}(m, Z)$) and its metallicity ($f_{\mathrm{Z}}(m, Z)$) from stellar models. We obtain the data for low and intermediate mass stars from Karakas [39] and the data for quasi-massive and massive stars from Portinari et al. [77].

Feedback fraction

Given the prerequisites from above, we can compute the ejected fraction for a stellar population:

$$\epsilon_{\mathrm{ret}}(Z) = \int_{M(t_{\mathrm{max}}, Z)}^{100\ \mathrm{M}_\odot} m\tilde{\xi}(m) f_{\mathrm{ret}}(m, Z)\,\mathrm{d}\,m \tag{4.18}$$

which effectively is an IMF-average with certain mass boundaries. The upper bound is the same as for computing the temporal distribution. The lower bound is a little more involved: Instead of choosing a mass boundary directly, we opt for a maximum lifetime (t_{max}) for contributing stars. One natural option for this would be the end time of feedback. This choice would be equivalent to a lower mass bound of 6 $\mathrm{M}_\odot$ or counting only contributions from supernovae. Another natural choice would be 0.1 $\mathrm{M}_\odot$. Its downside is the large lifetime of such low mass stars, which is approximately 10 Gyr for stars with a mass of 1 $\mathrm{M}_\odot$ and a lot larger for very small masses and therefore comparable to or larger than the age of the universe. Instead, we chose to consider all stars with a lifetime of up to 1 Gyr. This figure is some kind of compromise between considering as much of the stellar population as possible while not having too big a span between the end of feedback and the maximum lifetime. We will investigate the influence of the maximum lifetime parameter in a later paragraph.

In figure 4.3, we show ϵ_{ret} for different metallicities and a linear fit to the data:

$$\epsilon_{\mathrm{ret}}(Z) = a \cdot Z + b \tag{4.19}$$

with coefficients

$$a = 0.402159, \qquad b = 0.35416.$$

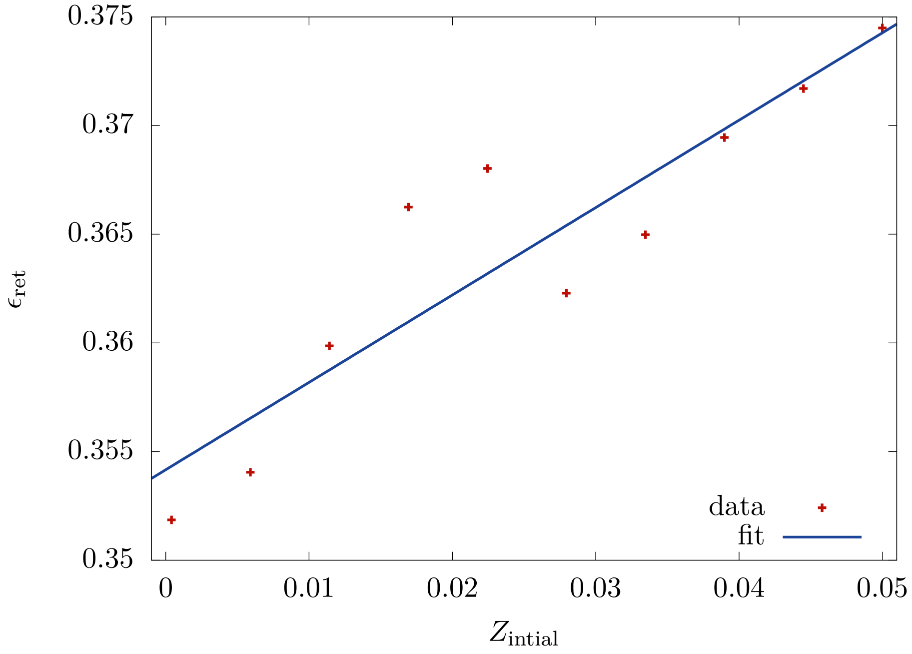

Figure 4.3: Data computed with equation 4.18 and the corresponding linear fit defined by equation 4.19. The fit is the metallicity-dependent matter return fraction used in the model.

In this paragraph, we are going to vary the two free parameters; the maximum stellar mass (usually chosen to be 100 $\mathrm{M}_\odot$) and the maximum lifetime of a star

($t_{\max} = 1$ Gyr) and see whether they show a strong influence.
When changing the maximum stellar mass from 100 $\mathrm{M}_\odot$ to 120 $\mathrm{M}_\odot$[5], we find an increase in ϵ_{ret} of up to 2 %. The minor influence is not unexpected since the IMF suppresses the very high mass end.
In contrast, a change in the maximum lifetime has a large effect: When reducing it to 0.1 Gyr (corresponding to a lower mass bound of 5 $\mathrm{M}_\odot$), the ejected fraction decreases by 30 % on average to a mean of 0.25, and when increasing the maximal lifetime to 10 Gyr (1 $\mathrm{M}_\odot$), the ejected fraction increases by 25 % to a mean of 0.45. This result confirms what has been stated above: AGB stars play an important role for feeding back material to the ISM.

Compared to feedback fractions chosen in the literature (see table 4.1), our choice is higher than most. Only Pallottini et al. [71] use even higher fractions, which goes back to the fact that they employ a lower mass limit of 0.1 $\mathrm{M}_\odot$. Nevertheless, assuming their mass limits, we obtain similar results which demonstrates the applicability of our model.

Feedback metallicity

For the feedback metallicity, we use the same type of model as for the feedback fraction above:

$$Z_{\mathrm{ret}}(Z) = \int_{M(t_{\max},Z)}^{100\ \mathrm{M}_\odot} m\tilde{\xi}(m) f_{\mathrm{Z}}(m, Z)\,\mathrm{d}\,m. \tag{4.20}$$

The resulting data is shown in figure 4.4. To approximate the data, we fit a third order polynomial to it

$$Z_{\mathrm{ret}}(Z) = a \cdot Z^3 + b \cdot Z^2 + c \cdot Z + d \tag{4.21}$$

and obtain the coefficients

$$a = 861.019, \qquad b = -70.5893,$$
$$c = 1.76586, \qquad d = 0.038915.$$

Since we use the same approach as for the feedback fraction, the model contains the same two undetermined parameters. To understand their influence, we employ the same analysis.

When increasing the upper mass limit from 100 $\mathrm{M}_\odot$ to 120 $\mathrm{M}_\odot$, we find a minor increase in the feedback metallicity of up to 4% with a mean of 0.042.

For the change in maximum lifetime from 1 Gyr to 0.1 Gyr, we obtain a decrease in metallicity by about 15–20 %, depending on the initial metallicity. For the comparison 1 Gyr to 10 Gyr, we obtain a moderate increase in the feedback metallicity of 7–10 % with a mean of 0.056. The mean metallicity for the fiducial

---

[5] The stellar data taken from [77] ends at 120 $\mathrm{M}_\odot$.

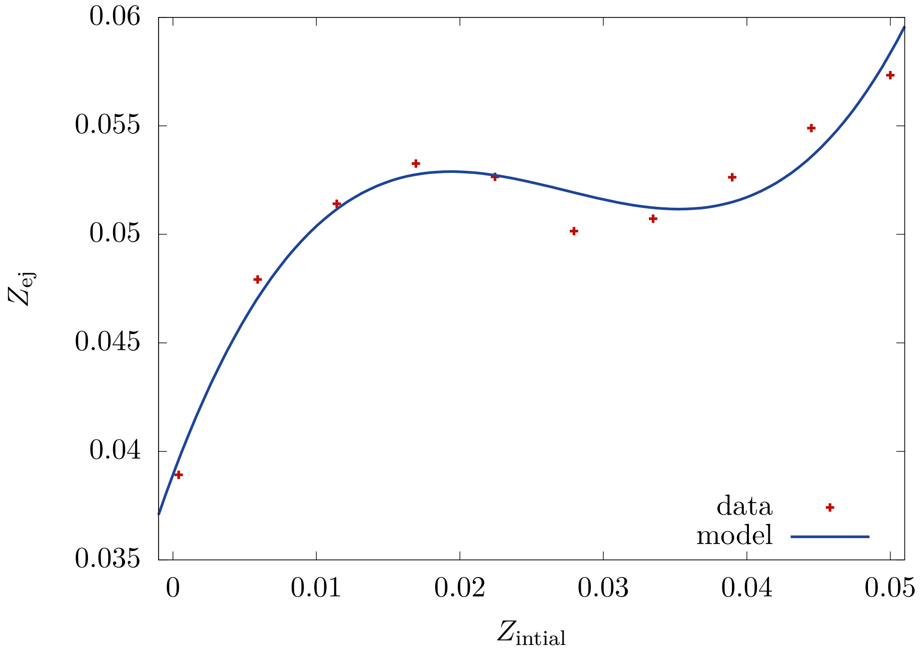

Figure 4.4: The feedback metallicity Z_{ej} as a function of the initial metallicity of the stars (equation 4.20) and the third-order polynomial fit (eq. 4.21) to it, which is used in the model.

case is 0.05. We note that the feedback fraction has a stronger dependence on the considered maximal lifetime than the feedback metallicity.

In table 4.1, we collected some parameters of simulations found in the literature. Our model gives metallicities very similar to the ones published by Pallottini et al. [71]. This is not unexpected since we share the approach for determining those. Two other publications use metallicities considerably lower. Martizzi et al. [59] employ a very high metallicity, but their very low return fraction compensates this. Therefore, the total metal mass given back to the sourrounding medium is similar.

The fact that the maximum lifetime is larger than the end time of the feedback implies that we enrich the gas too early. As a somewhat extreme case Pallottini et al. [71], assume a lower mass limit of 0.1 $M_\odot$ and therefore a maximum age of the stars way beyond the age of the universe while simultaneously adopting the instantaneous feedback approximation. Compared to that our approach seems to be well-motivated.

Publication	Fraction	Metallicity	Energy
[33], [34]	0.25	0.02	$5 \cdot 10^{48}$–$5 \cdot 10^{49}$ erg/$\mathrm{M}_\odot$ (varied)
[59]	0.1	0.1	10^{51} erg
[71]	0.47–0.50 (Z)	0.034–0.051 (Z)	$2.5 \cdot 10^{49}$ erg/$\mathrm{M}_\odot$
[99]	0.25	0.025	$1.78 \cdot 10^{49}$ erg/$\mathrm{M}_\odot$
Fiducial	0.35–0.375 (Z)	0.037–0.058 (Z)	10^{51} erg | $1.74 \cdot 10^{49}$ erg/$\mathrm{M}_\odot$
Low FB	0.088–0.094 (Z)	0.009–0.015 (Z)	$2.5 \cdot 10^{50}$ erg | $4.35 \cdot 10^{48}$ erg/$\mathrm{M}_\odot$

Table 4.1: Comparison of feedback parameters for different publications. Ranges marked with Z in parenthesis denote a metallicity-dependent prescription. The set called *Fiducial* is our main set of parameters, but some simulations have been done with the parameter set called *Low FB*. The two values for the feedback energy in our simulations are equivalent but necessary for comparison since some authors give the energy per supernova and others the energy per mass.

Feedback energy

In the first part of this section, we find that type-II supernovae are by far the most energetic feedback phenomenon. Therefore, we restrict our model to this. An usual supernova sets free an energy of 10^{53} erg, of which more than 99 % are emitted as neutrinos. The remaining 1 % is converted into kinetic energy, and 0.01 % are transferred into light in the optical window [29].

The only quantity to compute is the number of supernovae for a given stellar ensemble. It can be calculated using methods and mass boundaries discussed above:

$$\begin{aligned} n_{\mathrm{SNII}} &= \int_{6\ \mathrm{M}_\odot}^{100\ \mathrm{M}_\odot} \tilde{\xi}(m)\,\mathrm{d}\,m \\ &\approx 0.0174\ \frac{1}{\mathrm{M}_\odot} \end{aligned} \tag{4.22}$$

Note that this is the number of type-II supernovae per solar mass of stars. This approach is widely used in the literature. A collection of parameters is shown in table 4.1. Some authors prefer to write down the specific supernova energy for their model. For comparison, we compute $n_{\mathrm{SNII}} \cdot 10^{51}$ erg $\approx 1.74 \cdot 10^{49}$ erg/$\mathrm{M}_\odot$ and also note this in the table.

In the literature, it is quite common to assume some kind of coupling efficiency which we are going to discuss in a later chapter. To simplify comparison, we included them in the table.

In this work, we employ two sets of feedback parameters: *Fiducial* and *Low FB*. We note that our fiducial choice for the feedback energy lies well within the bounds set by the other publications. The *low FB* parameters are indeed low, but, apart from metallicity, they are not too far outside of the range found in the literature and just a little smaller than the low feedback variant in [34].

4.4 Star Particles

In the previous sections, we develope a model for star formation and stellar feedback, agnostic of simulation techniques. In this section, we are going to discuss the simulation techniques used to implement the model.

In simulations not resolving stars explicitly (i.e. not having a resolution below about one astronomical unit), these are modelled as collisionless particles. Each of these star particles represents an ensemble, usually chosen to be compliant with the IMF. This motivates our use of IMF-averaged quantities above. Here, we identify $M_{\text{population}}$ used in the previous sections with the mass of the star particle.

4.4.1 Life cycle of a star particle

Star particles are spawned according to the star formation recipe; ours is described in 4.2. Star formation models produce varying amounts of stellar mass. In contrast, the numerics of N-body simulations works best if all particles are of the same mass[6] [101]. Furthermore, some star formation recipes produce small amounts of stellar mass very often. To avoid this, some authors forbid star formation if the mass of the star particle would be below a minimum mass [105] or allow spawning in this case only with a certain propability [33, 34]. Our approach is different: We collect stellar mass in an additional field (governed by equation 2.11) and form stars or accrete to existing star particles from it. This approach is described in the remainder of this section.

The life cycle of a star particle is outlined in figure 4.5. We note that the approach described here is similar to the one described in Braun et al. [8] and shares some code with it. A new star particle is formed in a cell if more than the minimal mass M_{min} is present after the mass accreted by all other particles has been subtracted. Subsequently, the particle accretes further stellar mass until either the life time of the particle exceeds the accretion time scale (t_{acc}) or the maximum mass (M_{max}) is reached. All mass assigned to the star particles is taken out of the baryonic density, so that mass conservation is ensured. To avoid numerical problems, we limit the amount of mass taken out of a cell in one time step to half the available mass [17, 71]. In the next step, the feedback prescription takes over. After the feedback is done, the particle is either too heavy to accrete further, or its time is reset and it is set to wait for another cycle of accretion and feedback.

This part of the model has two free parameters: M_{min} and M_{max}. (t_{acc} and t_{fb} are set by the feedback model.) M_{min} is a purely numerical parameter; we choose $M_{\text{min}} = 10^4\ \text{M}_{\odot}$. This fits well with our star formation model since most events of star formation predicted by it produce a stellar mass of more than M_{min}. If we would not restrict the maximum mass of a star particle through M_{max}, they

---

[6] Technically, the star particles are treated like dark matter with respect to gravity.

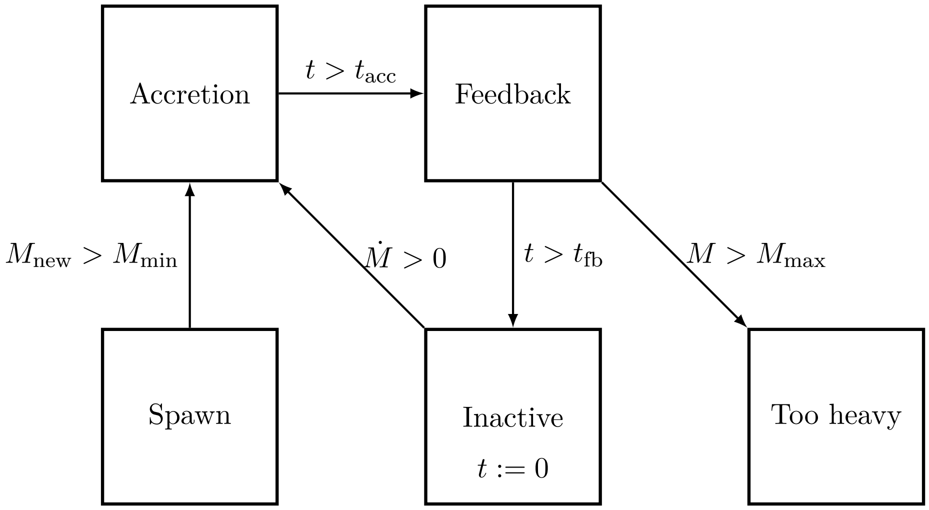

Figure 4.5: The life cycle of a stellar particle. Each square represents a state in which the star particles reside, and each arrow represents a transition. The terms labelling the arrows are the prerequisites of the state change. Each particle can only be in one state.

would accrete infinitely and gain masses far larger than the dark matter particles. This is unfavourable from a numerical point of view. Therefore, M_{max} is set equal to the mass of the dark matter particles. Furthermore, we varied the maximum mass and found that if the mass of dark matter particles is exceeded by two orders of magnitude, one can reach $z = 0$ with several thousand stellar particles while loosing only minor accuracy, mostly in the density distribution of the stars. With this choice, one can only gain a small amount of computational performance. Consequently, M_{max} does not have a large influence, and it seems most important to set it similar to the dark matter particle mass.

4.4.2 Feedback transfer

In the above sections, we determine the amount and temporal distribution of feedback. We also discuss a framework for stellar particles. This section deals with methods to apply the feedback. The central problem is to find a suitable subgrid prescription for the collective effects of many supernovae.

The simplest method is to just add the feedback to the cell in which the particle lives. The idea is that the injection of a lot of internal energy will lead to a huge increase in temperature and pressure and therefore will push out material. This approach is pretty old, but still widely used ([40, 71, 72, 99]), especially in low resolution simulations. However, it is well-known that this approach bears problems: The cooling time scales are usually a lot lower than the time scales on which the material is ejected. This effect is known as the overcooling problem.

There is a number of methods which are designed to avoid this.

One method, which is used especially in SPH simulations, is explicit kinetic feedback, instead of or in addition to the thermal one described above (e.g. [17, 101, 111]). In this approach, wind particles are spawned and given momentum. The downside of this is its complexity, especially for AMR codes. Additionally, one introduces a number of free model parameters.

Another manifest solution is cooling suppression, i.e. one switches off cooling in cells where feedback is active. Hummels and Bryan [33] justify this method by comparing it with a Sedov-Taylor blast wave solution, which is a model for the shock front of a supernova. They show that a time scale calculated using a Sedov-Taylor solution is too short to be effective. Williamson et al. [115] see cooling suppression as a simple way to mimic a turbulence subgrid model. For comparison we implement this approach[7]. Our solution simply switches cooling off in all cells that receive feedback. Therefore, we do not have an explicit cooling suppression time scale, since it is identical to the feedback time scale. In contrast to Hummels and Bryan [33] our cooling suppression therefore only starts when the feedback is beginning and not immediately after the star particle is born.
Although cooling suppresion is widely used in the literature (see references in [33] and [115]) it is an ad-hoc approach and in our opinion not well motivated. Instead, we advocate for explicit turbulent feedback, as we will explain in section 4.5.

In contrast to many other simulations, which add the feedback to the cell where the particle resides (nearest grid point, NGP), we distribute the feedback over 27 surrounding cells using cloud-in-cell (CIC). This approach is similar to Smith et al. [99], who, in turn, distribute the feedback equally over the same number of cells. Smith et al. [99] motivate this approach by the assumption that feedback material can move a significant distance away from the sources before cooling, which is what they try to mimic with this approach. They find that using their resolution (33 kpc/h $\approx$ 47 kpc and above) the distributed feedback alone is sufficient to avoid overcooling. For this reason we adopt this approach. Nevertheless, we did some simulations with NGP for comparison. We are going to discuss them and the critics of this method in section 5.2.6.

4.4.3 Single particle tests

To test the implementation of the star particles, we perform simulations in which a single stellar particle is formed in the center of the simulation and is evolved. The main goal of these simulations is to test the feedback prescription of the star particles by comparing it to the model plots shown above. For this, simulations with a simulated time longer than the end time of the feedback ($\approx 7 \cdot 10^7$ years) are performed.

---

[7] For a comparison, see the results section 5.3.5

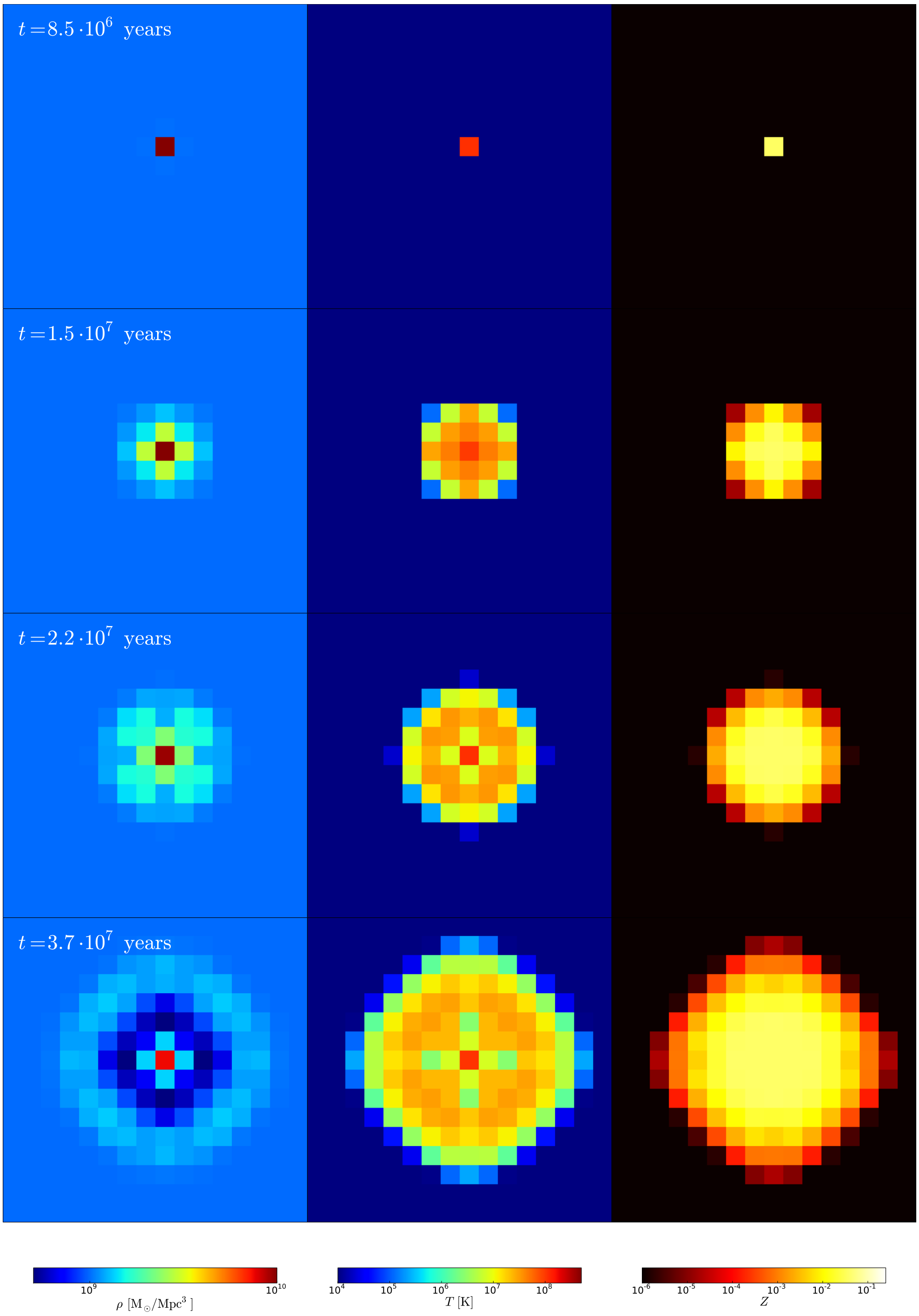

Figure 4.6: A simple test of the prescription of stellar particles. We set up single cell for star formation in the center of the domain and let the particle evolve. We note that even in the last slice the feedback is still active which corresponds to the position of the density and temperature maximum.

Additionally one can gain minor insights into the behaviour of feedback. To illustrate this, we show slices of one of the tests in figure 4.6. The resolution is the same as in our fiducial run and we use the full model of stellar feedback and (metal) cooling. In the first time step a star particle with 10^6 $\mathrm{M}_\odot$ is generated in a box with a uniform density of 10^9 $\mathrm{M}_\odot/\mathrm{Mpc}^3$. The feedback is not distributed, but only assigned to the cell containing the particle.

The feedback leads to a density wave propagating outwards. The wave is driven by the thermal pressure due to the thermal feedback. Furthermore the feedback enriches the gas inside the wave with metals. The feedback is exceptionally efficient since two counteracting processes are not active (inflowing gas) or weak (gravity; the stellar halo is very light compared to the feedback energy available).

4.5 Turbulent stellar feedback

One important problem in cosmological simulations is the efficiency of feedback or the avoidance of the overcooling problem. We discuss several well established solutions and their limitations in section 4.4.2. In this section we want to discuss an alternative approach: Explicit turbulent feedback. As we have seen in the previous chapters, turbulence is ubiquitous and fundamental in regions for star formation: Turbulence triggers star formation and stellar feedback via supernovae is considered to be an important source of turbulence.

Furthermore, we note that recipes like cooling suppression are seen as a way to mimic turbulence or its effects [33, 115]. Since our simulations feature a well-established subgrid model for turbulence, as described in section 2.5, we can simply use it to model the turbulent effects of stellar feedback.

The implementation of turbulent feedback is straight forward: We split the feedback energy into two components and add one to the internal energy and the other to the turbulent energy:

$$\begin{aligned} S'_{\rho e} &= (1-\epsilon_{\mathrm{SGS}})S_{\mathrm{FB}}, \\ S'_{\rho K} &= \epsilon_{\mathrm{SGS}} S_{\mathrm{FB}}. \end{aligned}$$

The primes on the left hand side indicate that this is only one contribution to the sources.

The central idea behind turbulent feedback is that the feedback energy is put into an energy reservoir which does not cool. Broadly speaking, we suppress cooling in a physically motivated way. The turbulent energy is then dissipated slowly into the internal energy. During this time the feedback energy is not only hidden from cooling, but also has dynamical effects: The turbulent pressure helps in pushing the gas outwards.

The fraction of turbulent feedback is a free parameter. Braun and Schmidt [6] use results by Thornton et al. [106] and argue that all of the kinetic feedback of a supernova is turbulent energy. With this assumption, they derive $\epsilon_{\text{SGS}} = 0.085$. Since our simulations are much more coarsely resolved, we assume that also the thermal energy deposited in the interstellar medium eventually contributes to the generation of turbulence. Therefore we set $\epsilon_{\text{SGS}} = 0.2$. Additionally, we vary ϵ_{SGS} to study its influence.

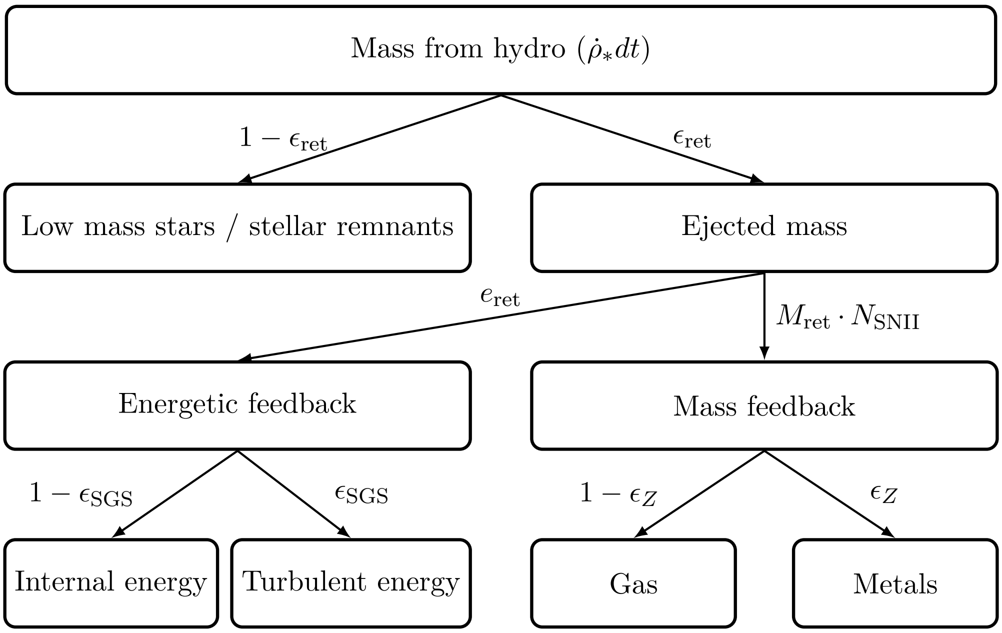

Figure 4.7: This figure sums up the feedback model. We note that it is slightly simplified.

Having discussed every aspect of the feedback model employed in this work, we summarize it in figure 4.7. It contains the processes and their corresponding parameters discussed in this chapter.

4.6 Turbulent diffusion

One important aspect of turbulence is its ability to homogenize properties of fluids like internal energy or its composition. Turbulence can achieve this mixing more efficiently than a laminar flow [76]. Metaphorically speaking, this is easy to explain: A turbulent eddy transports material on the eddies scale. In our simulations there is one quantity, whose production is highly localized and where a knowledge of its distribution is important: metallicity. However, this is not the only quantity being mixed. Also internal energy and turbulent subgrid energy have to be treated this way. In this section we are going to discuss turbulent diffusion with a focus on the mixing of species.

As a first step we derive the mixing term for species. For this, we look at the continuity equation:

$$\frac{\partial}{\partial t}\rho + \nabla \cdot (\rho \mathbf{v}) = 0. \tag{4.23}$$

The idea behind turbulent subgrid models (as mentioned in chapter 2) is to filter the hydro quantities at the grid scale and to derive equations for the filtered quantities. Filtering the continuity equation yields:

$$\frac{\partial}{\partial t}\overline{\rho} + \nabla \cdot (\overline{\rho \mathbf{v}}) = 0 \tag{4.24}$$

where $\overline{\rho \mathbf{v}}$ can be split into the resolved quantities $\overline{\rho}$ and $\widetilde{\mathbf{v}}$:

$$\overline{\rho \mathbf{v}} = \overline{\rho}\widetilde{\mathbf{v}} \tag{4.25}$$

using the definition of the Favre-filtered (or mass-weighted filtered) velocity [90]

$$\widetilde{\mathbf{v}} = \frac{\overline{\rho \mathbf{v}}}{\overline{\rho}}. \tag{4.26}$$

It is striking, that the filtered equation does not differ from the unfiltered one, so there are no source terms for the subgrid-model and we do not need to model turbulent diffusion of density fluctuations. This is due to the choice of the velocity filter and one central argument in favor of the Favre-filtering procedure.

But the situation is different if we split the density into species ($\rho = \sum \rho_{X_i}$, with in our case $X_i \in \{\mathrm{H}, \mathrm{He}, \mathrm{M}\}$). We obtain continuity equations for the different species:

$$\frac{\partial}{\partial t}\rho_{X_i} + \nabla \cdot (\rho_{X_i}\mathbf{v}) = 0. \tag{4.27}$$

After filtering these, we get:

$$\frac{\partial}{\partial t}\overline{\rho_{X_i}} + \nabla \cdot (\overline{\rho_{X_i}\mathbf{v}}) = 0. \tag{4.28}$$

The velocity for all species is the same, since they are part of the same fluid element and we neglect sophisticated plasma effects. To be consistent with the continuity equation for the total density, we have to use the Favre-filtered velocity. Plugging that in and rearranging the equations, we obtain a SGS source term on the right hand side:

$$\frac{\partial}{\partial t}\overline{\rho_{X_i}} + \nabla \cdot (\overline{\rho_{X_i}}\widetilde{\mathbf{v}}) = \underbrace{\nabla \cdot (\overline{\rho_{X_i}}\widetilde{\mathbf{v}} - \overline{\rho_{X_i}\mathbf{v}})}_{T_{\rho X_i}}. \tag{4.29}$$

When modeling this term, certain conditions have to be fulfilled:

1. If $\rho_{X_i} \to \rho$ then $T_{\rho X_i} \to 0$. (The reader is reminded that the SGS model does not allow for turbulent diffusion of density.)
2. $\sum \rho_{X_i} = \rho$ has to be fulfilled at all times.
3. The total mass of each species summed over the box has to be constant.

A common way of modelling turbulent diffusion is to use Fick's law. This is done for the diffusion of subgrid energy and internal energy e.g. in [88, 90] and in this work. The central assumption behind this is that phenomenologically turbulent diffusion can be modelled the same way as molecular diffusion. This approach is also called the gradient diffusion hypothesis [76, 90] (see the last term in equation 2.13e in section 2.5). The turbulent diffusivity is then estimated using the turbulent Prandtl number, which is usually considered to be of order one [76]:

$$\begin{aligned}\sigma_T &= \frac{\nu_{\mathrm{SGS}}}{\kappa_{\mathrm{SGS}}} \\ &\approx 1.\end{aligned} \tag{4.30}$$

After rearranging and inserting the definitions of ν_{SGS} we obtain the functional form of the turbulent diffusivity:

$$\kappa_{\mathrm{SGS}} = c_\kappa \Delta \sqrt{K}. \tag{4.31}$$

Herein, we introduced an additional constant $c_\kappa = 0.65$, which has been calibrated by Schmidt et al. [90]. We note that Pope [76] criticizes the gradient diffusion approximation, because in general the turbulent transport is not fully aligned with the gradient of the transported quantity. However, this approximation is widely adopted in the literature.

Having discussed turbulent diffusion in general, we return to the turbulent diffusion of species. Landau and Lifshits [47] give the following extended continuity equation for species concentrations $c_i = \frac{\rho X_i}{\rho}$:

$$\frac{\partial \rho c_i}{\partial t} + \nabla(\rho c_i \mathbf{v}) = -\nabla \mathbf{j_i}, \tag{4.32a}$$

$$\mathbf{j_i} = -\rho D \nabla c_i. \tag{4.32b}$$

For brevity we drop the bars and tildes denoting the filtered quantities from now on. Conveniently, this is a flux-formulation with the flux $\mathbf{j}$, which (if implemented correctly) automatically fulfills condition 3. Figure 4.8 sketches two cases for diffusion across a cell boundary and shows that using this formulation condition 1 is fulfilled. Since the hydro scheme takes care of the advection of species as described in equation 2.11, we implement the diffusion part as a source term:

$$S_{\rho_i} = \nabla \cdot \left(\rho \kappa_{\mathrm{SGS}} \nabla \left(\frac{\rho_i}{\rho} \right) \right). \tag{4.33}$$

A test of the implementation is shown in figure 4.9.

Diffusive initial value problems (like the one we discuss in this section) are best solved using implicit numerical methods. However, in our case this implies

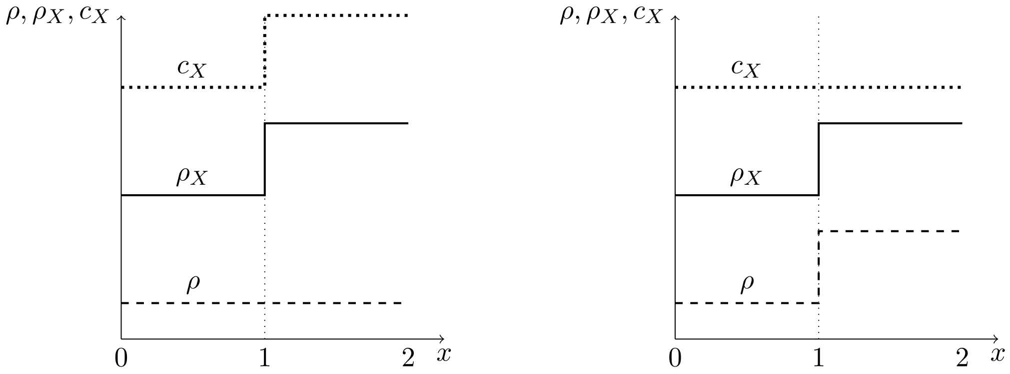

Figure 4.8: This figure shows the two limiting cases for diffusion across a cell boundary: The left one allows for maximum diffusion and the right one does not allow for diffusion at all, since there is no gradient in species and diffusion of density gradients is not allowed. This makes clear, that condition 1 is automatically fulfilled.

solving large matrix equations distributed over the whole grid. Although this can be done (the methods used for the Poisson equation could be applied here), it is computationally expensive and difficult to implement. Therefore, we use an explicit scheme. The main problem with explicit schemes is the fact that simulations have to obey comparatively small timesteps. Press et al. [79] give the condition

$$\frac{2D\Delta t}{(\Delta x)^2} \leq 1 \tag{4.34}$$

for an equation like

$$\frac{\partial f}{\partial t} = \frac{\partial}{\partial x}\left(D\frac{\partial f}{\partial x}\right) \tag{4.35}$$

with a constant coefficient D. In absence of a better approach we set $D = \rho\kappa_{\mathrm{SGS}}$ and thereby make the assumption, that D does not change rapidly. In the rare cases in which the timestep exceeds the one allowed by the above criterion, we do not decrease the timestep, but limit the diffusion. This way we make sure that our simulations do not suffer from very small timesteps.

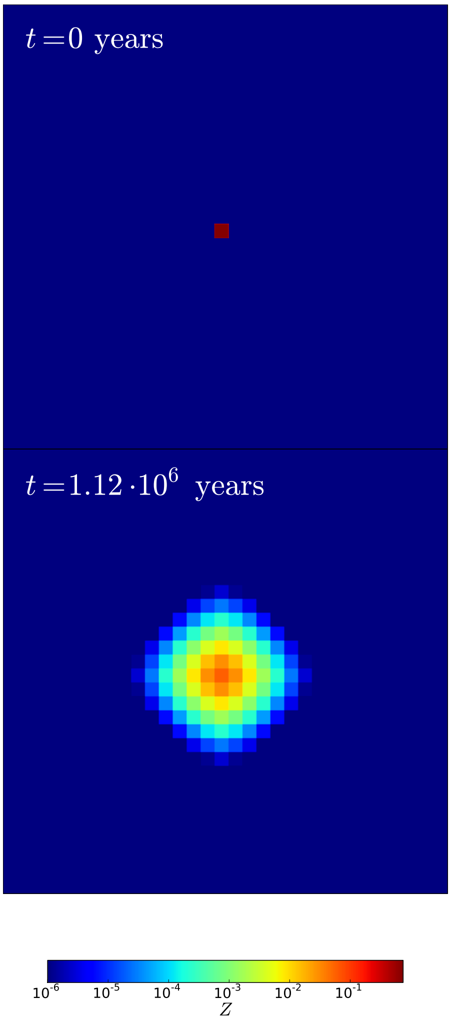

Figure 4.9: A simple test of the diffusion implementation. The grid is initialized with a uniform density $\rho = 10^{14}\ \mathrm{M}_\odot/\mathrm{Mpc}^3$ and uniform turbulent kinetic energy $K = 10^4\ \mathrm{km}^2/\mathrm{s}^2$. Both are typical values inside a simulated galaxy. The metallicity is chosen to be zero everywhere but in the central cell where it is set to 0.75. The system is evolved for 1.12 million years. During this time, the turbulence decayed to $K \approx 2 \cdot 10^3\ \mathrm{km}^2/\mathrm{s}^2$ which is to be expected. The boxsize is 400 kpc, the resolution $\Delta = 12.5$ kpc. This is approximately the finest grid resolution in most of the simulations presented throughout this work.

The figure shows that turbulent diffusion works and is able to reduce the metallicity to 7% of its initial value during less than one tenth of the feedback time under highly idealized conditions.

5 Results

> *„Woran arbeiten Sie?“ wurde Herr K. gefragt. Herr K. antwortete:*
> *„Ich habe viel Mühe, ich bereite gerade meinen nächsten Irrtum vor.“*
> — Bertolt Brecht, *Geschichten von Herrn Keuner*

In this chapter we present a large number of simulations using the model developed in the previous chapter and employing the methods discussed in chapter 2 and 3. It is structured as follows: The first section presents the simulation which we find to represent the observations best. We point out the limitations of that simulation and compare our results to the literature. Meanwhile, we document the analysis methods we employ in the following. In the second section, we vary the fundamentals of the model to explain our choice of parameters and to show the robustness of our model. The third section is the key part of this work, where we discuss the influence of turbulence and turbulent mixing processes on star formation and stellar feedback.

All simulations are documented in table 5.1. In the figures as well as in the text, the names of simulations as given in that table are written in italic. Furthermore, a fixed color is assigned to the six most important simulations, which is used in all corresponding plots. Since the model and our understanding of it evolved with time, not all simulations presented in this chapter share the same physics, initial conditions, and parameters. Therefore, it is important to pay attention to the differences in the setup of certain simulations.

5.1 Validation & analysis techniques

In this section, we discuss the properties of the simulation labeled *fiducial* in table 5.1. As the name suggests, we compare most of our results with this simulation. Therefore, it is important to show that this simulation gives reasonable results. Furthermore, this section aims to give reasons for the applicability and validity of our model in general.

Additionally, we explain the analysis techniques we use in the subsequent sections. The modus operandi established in this section is to start with global observations and then move on to more local ones. We will keep this approach in the following sections although we will not show every plot for every simulation.

	Name	l [Mpc]	N_{level}	IC	SGS	Int. E Diffusion	Species Diffusion	Turbulent Feedback	Cooling Suppression	ϵ_{ff}	δ_{SF}	ϵ_{SGS}	α_{FB}	Additional
🟩	*fiducial*	12.5	2	A	✓	X	X	✓	X	0.005	10^4	0.2	1	
🟨	*esgs0.0*	12.5	2	A	✓	X	X	X	X	0.005	10^4	0.0	1	
🟩	*esgs0.5*	12.5	2	A	✓	X	X	✓	X	0.005	10^4	0.5	1	
🟦	*specdiff*	12.5	2	A	✓	X	✓	✓	X	0.005	10^4	0.2	1	
🟥	*intediff*	12.5	2	A	✓	✓	X	✓	X	0.005	10^4	0.2	1	
🟪	*alldiff*	12.5	2	A	✓	✓	✓	✓	X	0.005	10^4	0.2	1	
	nosgs	12.5	2	A	X	X	X	X	X	0.005	10^4	-	1	
	coolsupp	12.5	2	A	✓	✓	✓	✓	✓	0.005	10^4	0.2	1	
	ic_b	12.5	2	B	✓	X	X	✓	X	0.005	10^4	0.2	1	
	ic_c	12.5	2	C	✓	X	X	✓	X	0.005	10^4	0.2	1	
	nometalcool	12.5	2	A	✓	✓	✓	✓	X	0.005	10^4	0.2	1	no metal cooling
	ngp	12.5	2	A	✓	✓	✓	✓	X	0.005	10^4	0.2	1	no distribution of feedback
	sf_calib1	12.5	2	A	✓	✓	✓	✓	X	0.01	10^4	0.2	1	
	sfc_fid	12.5	2	A	✓	✓	✓	✓	X	0.01	10^4	0.2	0.2	
	sfc_therm	12.5	2	A	✓	✓	✓	✓	X	0.01	10^4	0.2	0.2	a)
	sfc_therm+conv	12.5	2	A	✓	✓	✓	✓	X	0.01	10^4	0.2	0.2	b)
	sfc_all	12.5	2	A	✓	✓	✓	✓	X	0.01	10^4	0.2	0.2	c)
	calib_x_y	12.5	2	B	X	X	X	X	X	x	y	-	0.2	

Table 5.1: Overview on the properties and parameters of all simulations presented in this work. a) thermal restrictions, b) thermal restrictions and converging flow, c) converging flow, thermal restrictions, and jeans criterion

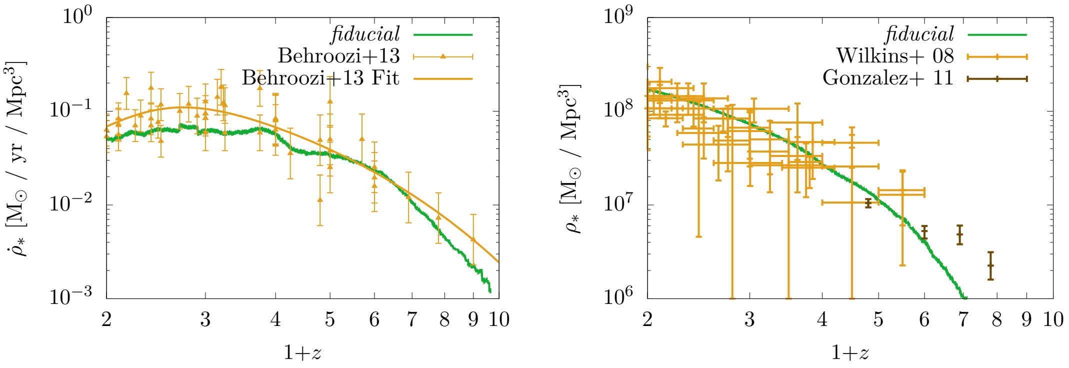

(a) Global star formation rate

(b) Global stellar density

Figure 5.1: Stellar history in the *fiducial* simulation. The star formation rate was post-processed using a moving average over 200 Myr. It is compared to data compiled by [4]. The stellar density is an integrated quantity and therefore smooth by itself. For comparison, we show data compiled by Wilkins et al. [114] and González et al. [25]. The conversion to a Chabrier IMF was done using the methods described in [82].

5.1.1 Stellar history

Cosmological simulations employing star formation have to be calibrated to match star formation and stellar densities as observed in the universe. We demonstrate in figure 5.1 that the *fiducial* simulation reproduces the observed stellar history quite well. The star formation rates are compared to a compilation of observations by Behroozi et al. [4] and to a fit to this data from the same source. The star formation rates in the simulations are very spiky due to the random nature of star formation. Therefore, we smooth the data by applying a moving average with a width of 200 Myr. It has to be noted that our model slightly underpredicts star formation. On the contrary, our model fits the observed stellar densities by González et al. [25] and Wilkins et al. [114] very well. Both figures show that star formation starts rather late and should be more efficient at early times. This is due to the fact that we use a rather small box and an intermediate resolution. Following the bottom-up paradigm of structure formation, massive objects are rare at early times. Schaye et al. [84] find that star formation is therefore dominated by small mass haloes, which need a very high resolution to be sufficiently resolved. For late times, in contrast, Schaye et al. [84] show that a large box is needed to obtain a converged star formation rate. At late times, star formation is dominated by the most massive objects which are seeded by large scale perturbations. As discussed in chapter 3, the size of the box corresponds to the size of the largest mode. Additionally, Vogelsberger et al. [111] find that at $z \lesssim 2$, star formation is significantly suppressed due to feedback from active galactic nuclei (AGN).

Our simulated star formation rate density does not show a distinct peak around $z = 2$, but rather a plateau. We attribute this to missing AGN feedback and the problems discussed in the following section. Nevertheless, we find the stellar histories to be well-converged with respect to our choice of observations.

In the following sections, we also present figures in which we show quantities q (i.e. star formation rates or stellar densities) relative to a fiducial q_{fiducial} using the following definition:

$$\begin{aligned} q_{\text{relative}} &= \frac{q - q_{\text{fiducial}}}{q_{\text{fiducial}}} \\ &= \frac{q}{q_{\text{fiducial}}} - 1. \end{aligned} \tag{5.1}$$

5.1.2 Mass functions

The halo mass function of the *fiducial* simulation at $z = 2$ is shown in figure 5.2a and compared to an analytical description by [96]. We compute the halo mass function by running HOP [19] as part of the yt-toolkit [108] and by subsequently binning the data. We find deviations from the analytical formulation in haloes with less than 10^9 $\mathrm{M}_\odot$, which corresponds to approximately 300 dark matter particles. This is comparable to other particle mesh simulations, e.g. [99]. On the high mass end, we see too few massive haloes and a drop-off at a few times 10^{12} $\mathrm{M}_\odot$. This is due to the small box size; the analytical halo mass function only drops off around 10^{15} $\mathrm{M}_\odot$.

Figure 5.2b shows the stellar mass function at $z = 2$. We compute the stellar mass function by integrating the stellar mass in all haloes from the center of the halo (as given by the halo finder) to the virial radius $r_{vir} = r_{200}$. We compare the stellar mass function to observational data and to a fit by Pérez-González et al. [73]. The fit is a modified Schechter function [85] as given by [57]. Our simulation contains too many haloes with low stellar masses. The detailed results are discussed in the following paragraph since the stellar mass-halo mass relation and the stellar mass function are somewhat redundant.

In figure 5.2c, we show the stellar mass-halo mass relation at $z = 2$. We compute this relation from the data of the previous two plots and show the median of all data points in each mass bin. All haloes in our simulation contain too much stellar mass, which is consistent with figure 5.2b. Furthermore, this mass overprediction is more severe at the low mass end. The problems mentioned here are not unexpected since we calibrated the star formation prescription on the global quantities star formation rate and stellar mass density (see figure 5.1) which fit the data pretty well. Additionally, the halo mass function only drops off significantly around 10^{15} $\mathrm{M}_\odot$. Therefore, our simulation misses three orders of magnitude in halo mass. Only a volume sampling the full range of halo masses can fit both the global quantities (star formation rate and stellar density) and the local one (stellar

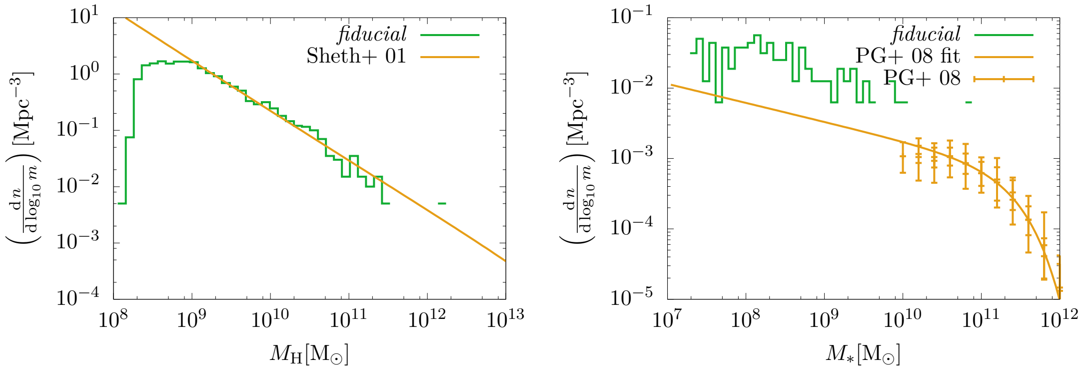

(a) Halo mass function

(b) Stellar mass function

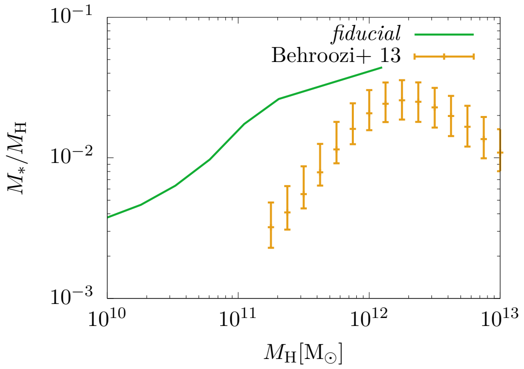

(c) Stellar mass-halo mass relation

Figure 5.2: Different mass functions for the *fiducial* simulation at $z = 2$. In figure a, the halo mass function is shown and compared to an analytical description by Sheth et al. [96] (computed using [66]). In figure b, we show the (global) stellar mass function, which we compare to observational data and a fit to this data by Pérez-González et al. [73]. Figure c shows the mean of stellar mass-halo mass relation together with data from Behroozi et al. [4].

name	density criterion	temperature criterion
warm	$\delta < 10^3$	$T < 10^5$ K
WHIM	$\delta < 10^3$	10^5 K $< T < 10^7$ K
hot	$\delta < 10^3$	$T > 10^7$ K
condensed	$\delta > 10^3$	none

Table 5.2: The definition of the phases used in this work. We follow [99].

mass function and stellar mass-halo mass relation). In simulations discussed in the following sections, we show that the stellar mass-halo mass relation is independent of initial conditions (section 5.2.1). Furthermore, heavier haloes exhibit higher virial temperatures, which help in reducing star formation.

5.1.3 Phase plots

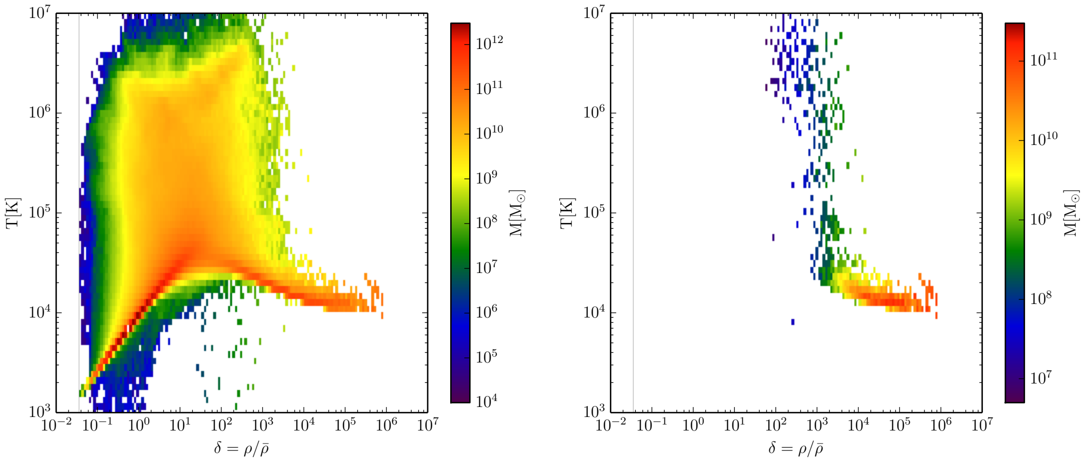

(a) Full box

(b) Cells with active feedback

Figure 5.3: Phase diagrams (temperature versus overdensity) for the full box and restricted to cells with active stellar feedback at $z = 2$.

Figure 5.3 shows ρ-T phase diagrams for the *fiducial* simulation at $z = 2$. The phase diagram in figure 5.3a shows the expected behaviour, as demonstrated in previous publications [40, 53, 92]. Below overdensities of 10^1, one finds a well-established line obeying a gamma-law relation, the so-called ρ-T relation of the intergalactic medium (IGM) [53]. For plots in the following section, we adopt one of the many definitions for gas phases, grouping the baryonic content of the universe by temperature and density, as defined in table 5.2. Going to high densities ($\delta > 10^3$), we find again a mass concentration in a line-like structure with roughly constant temperature of approximately 10^4 K. This phase is called the condensed

phase and is the gaseous constituent of the galaxies. We note that we find a significant fraction of gas above the density threshold for star formation ($\delta > 10^4$). This is due to the low star efficiency. Furthermore, we remind the reader of the fact that this line is rather broad compared to a simulation without stellar feedback.
The region above 10^5 K is called the warm hot intergalactic medium (WHIM). The WHIM mostly consists of gas that is shock-heated during the accretion to a filament or halo. The hot fraction ($T > 10^7$ K) is rather small, which we attribute, similar to [99], to the small box, in which haloes with virial temperatures in this range are not found. A halo with 10^7 K has $\sim 10^{15}$ $\mathrm{M}_\odot$ at $z = 0$ and $\sim 10^{13}$ $\mathrm{M}_\odot$ at $z = 2$ using the approximations by [64]. Our most massive halo has a virial temperature of $2.5 \cdot 10^6$ K.

In figure 5.3b, we show the same diagram, but restricted to cells with active feedback. Most of the feedback happens in the condensed phase, leading to the fuzzyness of the high-density line. Furthermore, we find cells with low densities and high temperature, which would usually be attributed to the WHIM or the hot phase. This does not mean that our model forms stars outside of galaxies, but that cells in or around galaxies are massively heated up by the feedback and thereby blow out matter, leading to high temperatures and low densities. Publications describing cluster simulations (for example [92]) use slightly different definitions of the phases and assigned most of the higher temperature gas in this figure to the intracluster medium (ICM, $\delta > 10^3$, $T > 10^5$ K). Our simulation does not contain a massive cluster, this fraction is basically empty in our simulations and therefore neglected.

5.1.4 Individual haloes

Slices

Having discussed the global quantities, we focus for the remainder of this section on the haloes. Foremost, we show slices through the centers of the five most massive haloes at $z = 2$ in figure 5.4. The slices are annotated with density contours (in white) and the black circle represents the virial radius. The numbering of the haloes is ordered by decreasing halo mass, the mass range depicted in the figure is $1.5 \cdot 10^{12}$ $\mathrm{M}_\odot$ to $2 \cdot 10^{11}$ $\mathrm{M}_\odot$.

The figure shows that the haloes have very different morphologies. Furthermore, the morphology seems to be independent of the halo mass.
Halo 0 and halo 2 show large outflows, hot surroundings and very complex structures in the distribution of the turbulence indicated by the subgrid energy K, even beyond the field of view of the figure. This is possibly related to a recent merger event. Furthermore, the distance between both is about 800 kpc. Therefore, halo 2 is not only surrounded by its own outflows, but also by the outflows of halo 0. Halo 1 does not have a similarly violent history, instead it seems not to have merged for quite a while. We see cold, pristine inflows from filaments from above

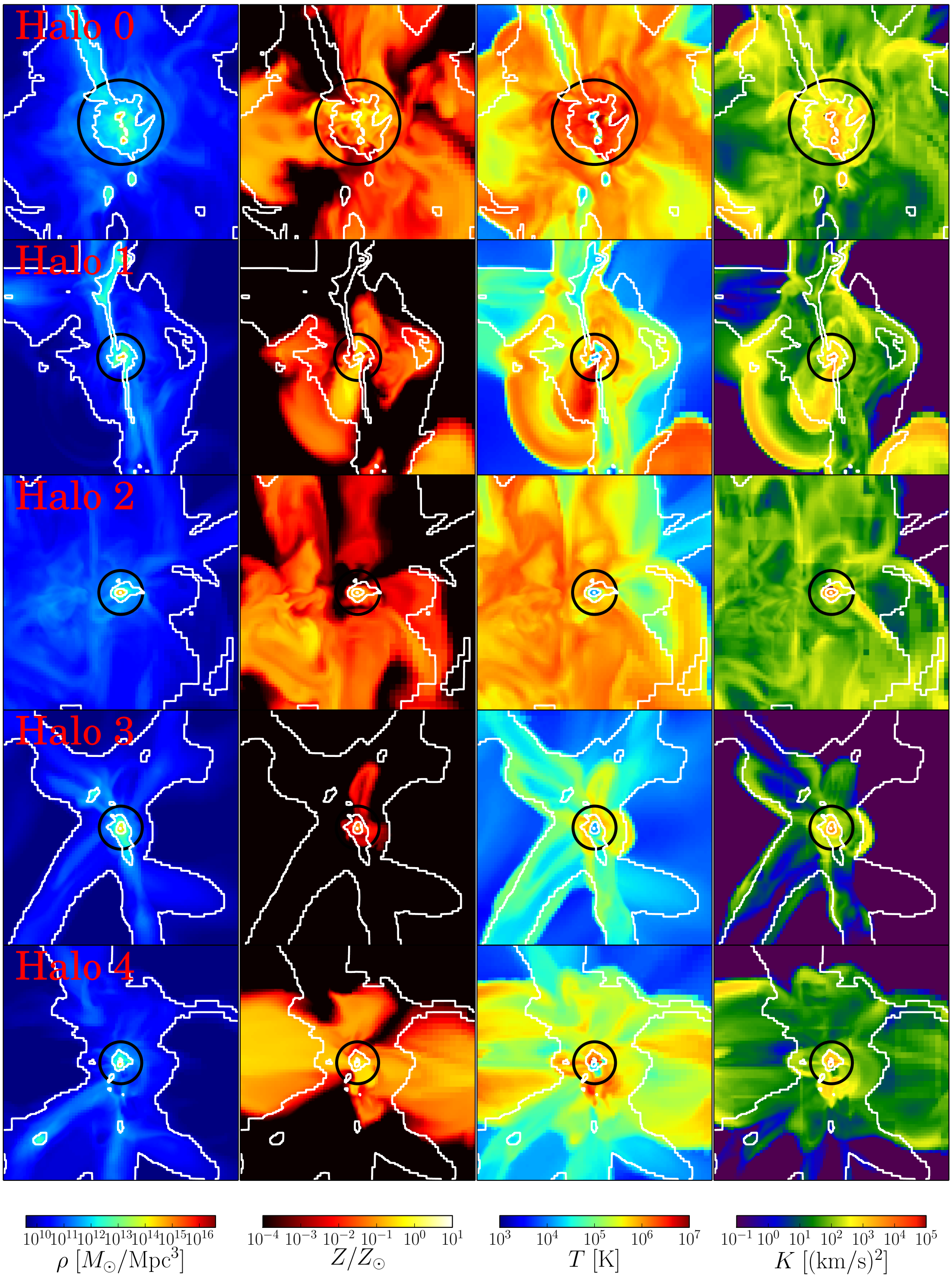

Figure 5.4: Slices of the five most massive haloes in the *fiducial* simulation at $z = 2$. Each panel has a width of 2 Mpc. The black circles represent the virial radii, the white contours are iso-density contours. The plot shows the baryon density ρ, the metallicity Z, the temperature T, and the turbulent subgrid energy K.

	IGM	CGM	ISM
Pallottini et al. [72]	$\delta < 10$	$10 < \delta < 10^{2.5}$ & $Z > 10^{-7} Z_\odot$	$\delta > 10^{2.5}$ & $Z > 10^{-7} Z_\odot$
Hummels et al. [34]	$r > r_{200}$	20 kpc $< r < r_{200}$	$r <$ 20 kpc

Table 5.3: Two definitions for the circumgalactic medium (CGM) in comparison to the intergalactic medium (IGM) and the interstellar medium (ISM). The baryonic cosmic mean is $\bar{\rho} \approx 6.3 \cdot 10^9$ $\mathrm{M}_\odot/\mathrm{Mpc}^3$; $10^{2.5} \cdot \delta \approx 2 \cdot 10^{12}$ $\mathrm{M}_\odot/\mathrm{Mpc}^3$.

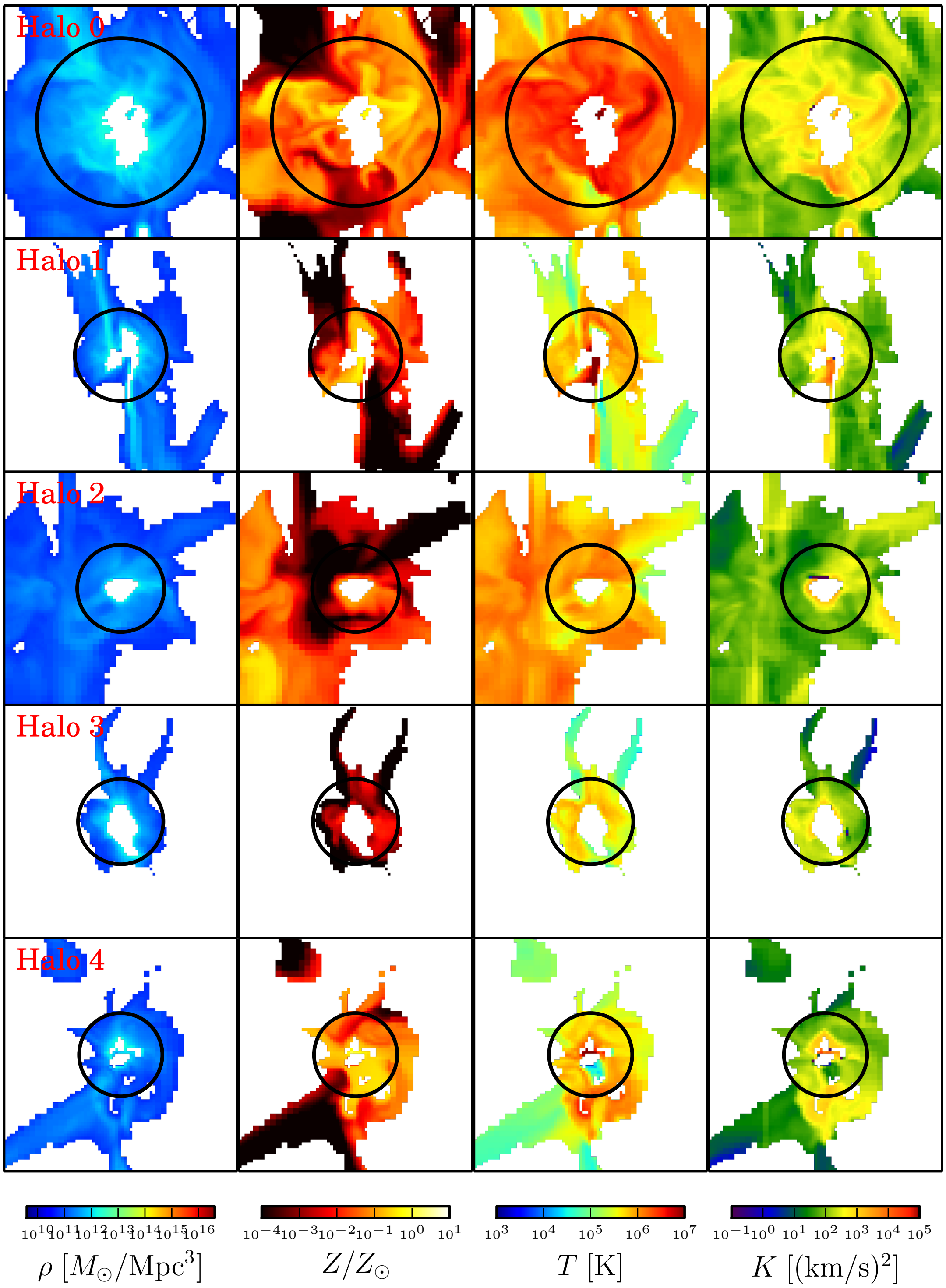

Figure 5.5: This figure is similar to figure 5.4, but only shows the CGM according to the definition by Pallottini et al. [72]. Again, we show the virial radius but omit the density contours. The width of each panel is 1 Mpc.

and below the galaxy and strong outflows next to the accretion stream below the galaxy. This outflow transports hot and metal-rich gas outwards. When this gas hits the gas accreted from the IGM, a shock front builds up. This front can be clearly seen in the turbulent energy, temperature, and metallicity and leads to a distinct drop-off in all those quantities. Even in the density, the bow shock is slightly visible. This object is a good example to illustrate why stellar feedback can enrich the surroundings of a halo but not arbitrarily far regions. Halo 4 is somewhat similar to halo 1, except that the feedback has pushed the gas farther out and the shock is not explicitly visible. Moreover, the density plot shows small objects that are in the process of merging. Halo 3 is the least active halo in our collection. The accretion shocks are due to pressure-stabilized gas. The enrichment with metals is only very weak, which is indicated by the very similar shape of the density contour compared to the shape of the drop-off edge of temperature and turbulent energy.

As discussed in the introduction, the CGM recently raised a lot of attention. In the literature, one finds several definitions for the CGM, of which we give two in table 5.3. Figure 5.5 shows a zoom-in of figure 5.4 while neglecting everything that does not belong the CGM as defined by Pallottini et al. [72]. We note that the original definition of Pallottini et al. [72] includes an additional criterion, which groups the simulation volume into connected patches with a metallicity of more than 10^{-7} $Z_\odot$. Since the slices do not show isolated patches of CGM, we can safely neglect this metallicity criterion.

The figure allows for a comparison of the CGM definitions, since the Hummels et al. [34] definition assumes the transition to the IGM at the virial radius, which we show in black. The ISM, according to this definition, is barely resolved and consists of a few pixels in the center of each panel. Both definitions agree pretty well for haloes that do not show intense outflows, like haloes 1, 3, and 4. In any case, the definition by Pallottini et al. [72] includes a significant amount of the filaments. In halo 0, the CGM according to Pallottini et al. [72] is significantly larger. This also holds for halo 2. Interestingly, the hot and metal-rich outflows of halo 1 are not seen as part of the CGM. Consequently, we also conclude that the CGM is not a homogeneous medium, but contains complex structures and a large range of metallicities, temperatures, and turbulent energies.

Profiles

Figure 5.6 shows profiles of the five most massive haloes in the *fiducial* simulation, which can be directly compared to the slices in figure 5.4. The profiles are obtained by radially averaging the quantities. The center for the profiling is defined as the point with the highest density in a sphere with virial radius and the dark matter center of mass as the spheres center. The vertical lines give the virial radius of the corresponding halo.

A number of conclusions can be drawn from the profiles. First of all, the evo-

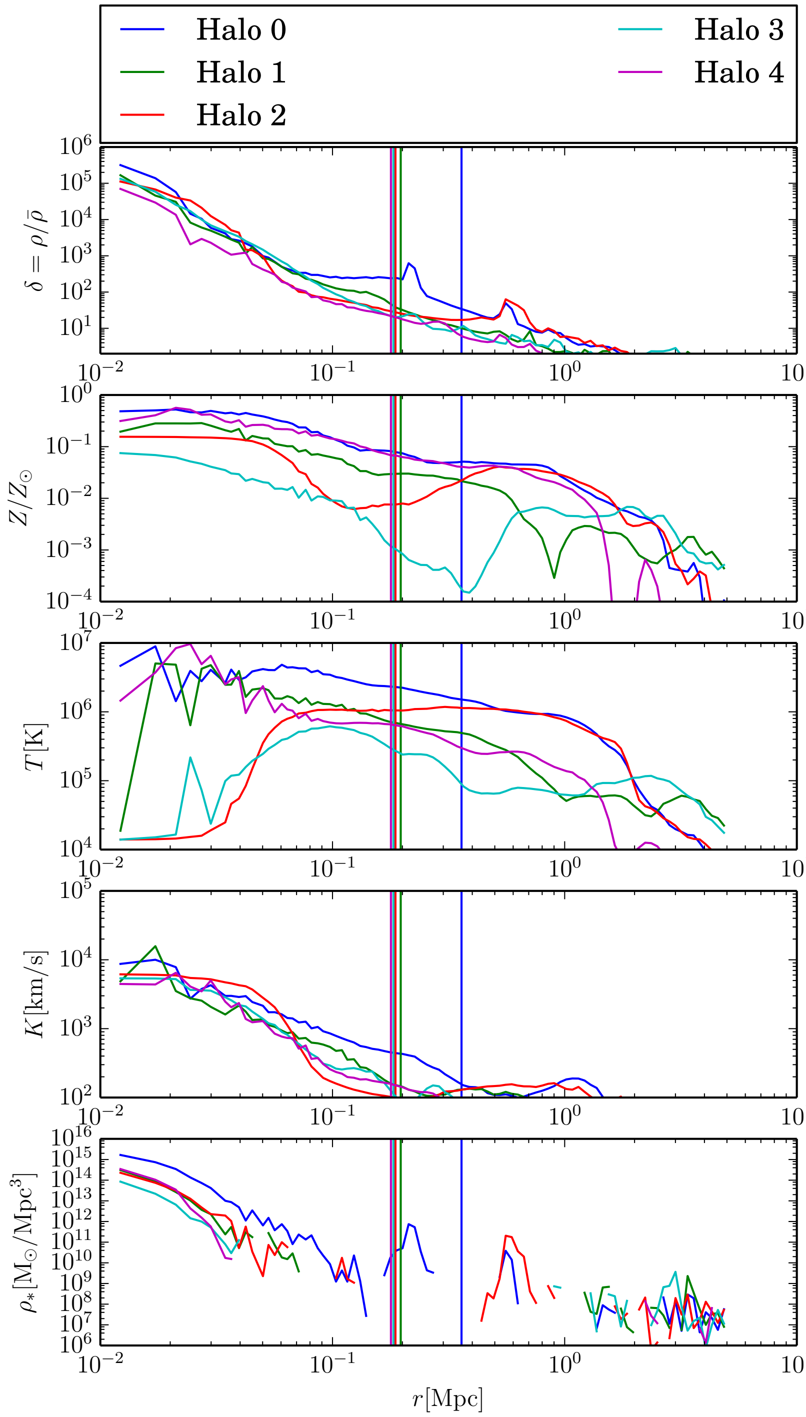

Figure 5.6: Profiles of the five most massive haloes in the *fiducial* simulation. The vertical lines correspond to the virial radii. The center for each profile is chosen to be the maximum of baryonic density inside the virial radius. The quantities given in the figure are baryonic overdensity δ, metallicity in units of the solar metallicity $Z/Z_\odot$, the temperature T, the turbulent subgrid energy K, and the density of stars ρ_*.

lution of density with radius is remarkably similar, although the slices show very different morphologies. The peak in the profile of halo 0 around 200 kpc indicates an infalling object and supports our hypothesis above. The peak at 600 kpc is due to the close proximity of halo 2.

The difference in metallicities is large, but this is expected from the slices. The slices show distinct cold central cores in all haloes, which is not reflected in the profiles. This is due to the fact that the cold spots are not necessarily at the point of highest density and that there are very hot outflows right next to the cold spots. Consequently, the temperature profiles get very spikey. This makes it hard to draw conclusions from the inner 100 kpc. The profile of turbulent subgrid energy shows that the turbulent energy is concentrated inside the virial radius. The profiles of stellar density give an indicator where metals were produced. The larger peaks in there are traces of infalling haloes.

Again, we discuss the two CGM definitions given in table 5.3. Here, we apply them to the profiles, rather than the raw data. Comparing those definitions, we find that they agree for the boundary between IGM and CGM but differ significantly for the CGM to ISM transition. This is explained in part by the fact that the ISM as defined by [34] is only coarsely resolved. Given any of these definitions, we find that we can use the profiles to give estimates for quantities like density and subgrid turbulent energy as a function of the radius. This is not the case for temperature and metallicity. Above, we concluded that the CGM is not homogeneous. Therefore, we point out that profiles and results concluded from profiles have to be used with care.

5.1.5 Stacked halo profiles

We discussed the profiles of the five most massive haloes in the previous section. To infer common properties of many haloes, we employ stacked profiles. We select haloes by their dark matter mass and bin their data in mass ranges. Additionally, only haloes with stars in the center and a minimal metallicity are considered. Both conditions are obviously satisfied for significantly massive haloes. In each mass bin, we collect the quantity of interest in radial bins, for which we normalize the radius by the virial radius. Afterwards, we plot the median of the data in each radial bin. We restrict this to bins to which all haloes contributed. This approach neglects some data at the inner and outer ends of the plots, but if we allowed for changes in the number of haloes contributing, we would obtain systematic deviations. A halo at the higher mass end of its mass bin, for example, contains probably more stellar mass and thereby more metals. Due to its higher mass, it has a larger virial radius, which leads to a contribution in sparsely filled bins at the low r/r_{vir} end. This leads to a bias in metallicity. Furthermore, extrapolating halo data in the binning process leads to similarly misleading results. A constant extrapolation, for example, would give the impression of flat cores with respect to density.

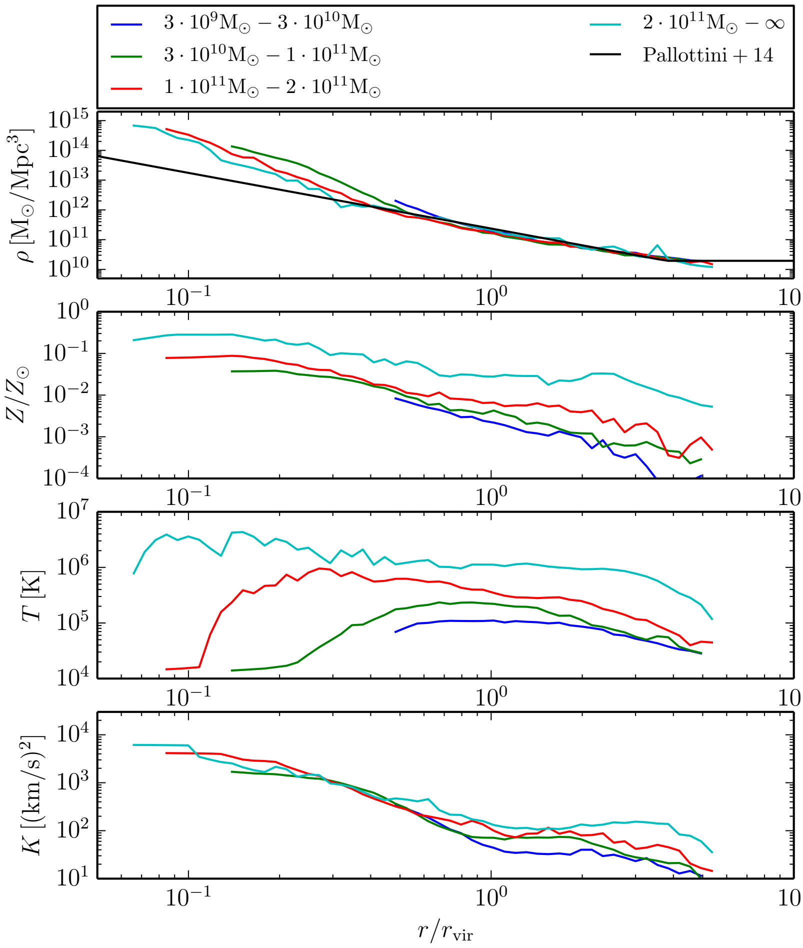

Figure 5.7: Stacked halo profiles for a number of mass bins at a redshift $z = 2$, including the fit by [72]. We show the quantities baryonic density ρ, the metallicity in units of the solar metallicity $Z/Z_\odot$, the temperature T, and the turbulent subgrid energy K.

Pallottini et al. [72] argue that density profiles are selfsimilar for a broad range of haloes and halo masses, once the radius is normalized by the virial radius. They define the "self-similar quantity" $x = r/r_{\mathrm{vir}}$ and give the following fitting formula for density:

$$\rho(x) = \rho_{\mathrm{vir}} \cdot \begin{cases} x^{-\alpha} & x < x_{\mathrm{IGM}}\,, \\ x_{\mathrm{IGM}}^{-\alpha} & x > x_{\mathrm{IGM}}\,, \end{cases} \tag{5.2}$$

using the parameters:

$$\alpha = 1.87, \qquad \rho_{\mathrm{vir}} = 37.5 \cdot \bar{\rho}, \qquad x_{\mathrm{IGM}} = 3.8.$$

Figure 5.7 shows stacked halo profiles for a number of mass bins. For comparison, we also plot the fit by Pallottini et al. [72]. The density profile is indeed very similar to the fit for all mass bins but the data shows a mass dependent turn-off. The higher the halo mass, the lower the radius at which the turn-off occurs. This effect may be partly explained by the resolution of the simulation. The heavier a halo is, the better resolved it is, and, consequently, effects due to the grid scale are reduced.

The metallicity is increasing with halo mass, which is to be expected. Stellar content scales with halo mass, and metallicity is (neglecting enrichment of the surroundings and recycling of material) a direct function of stellar mass. The more interesting part is that metallicity is not only higher in the central parts of a halo, but also on the outside. This suggests that more massive haloes are more effective in enriching the surroundings. Although our findings are more in favor of a late enrichment scenario, no final conclusion can be drawn since our resolution of the small haloes at early time is insufficient.

The temperature shows a similar behaviour as the metallicity, i.e. the higher mass haloes are hotter. For most mass bins, we find evidence of cold cores. The exception is the highest mass bin. The result for this mass bin is misleading since we know of the existence of cold cores from the previous sections.

The turbulent energy in turn shows similar profiles in the inner part for all mass bins. Above the virial radius, the level of turbulence seems to depend slightly on the mass but appears to form a plateau. This is probably due to infalling material being shocked by outflows or the galaxy itself.

Figure 5.8 shows a similar plot for $z = 4$ since the fit by [72] was derived at this redshift. Most of our observations for $z = 2$ are true for this plot, too. The exception is the metallicity profile. The most massive mass bin shows metallicities significantly higher while the lower mass haloes show very similar behaviour.

Fielding et al. [23] study the influence of star formation and feedback on the CGM using IDGs. They claim that the CGM and its physics change significantly around a halo mass of $10^{11.5}$ $\mathrm{M}_{\odot}$. Above this mass, the gas is supported by thermal pressure due to virial shocks. Below this mass, the gas is not thermally supported, but instead supported by turbulence and outflows. They attribute this to the fact that the virial temperature of a halo of this mass coincides with the maximum of the cooling rate. A halo with a mass below the limit has a smaller ratio of cooling time to free-fall time than a more massive one does. This argument has been known for simulations without feedback for some time (e.g. [5, 97]). Fielding et al. [23] claim that it is also valid for simulations with feedback.

We should therefore see a significant difference in the stacked halo profiles between the highest mass bin and the remainder of the bins. We do see a somewhat steady evolution of the quantities with halo mass. There is a change in temperature and metallicity for the highest mass bin, but it does not seem to be significant. Furthermore, when we go back to individual haloes and compare figure 5.4 to figure 3 in [23], we find that halo 0 and 4 are similar to their haloes with more than $10^{11.5}$ $\mathrm{M}_\odot$. In contrast, halo 3 looks similar to results of [23] for a 10^{11} $\mathrm{M}_\odot$ halo. According to their mass limit, halo 3 would have to be lighter than $10^{11.5}$ $\mathrm{M}_\odot$, which it is not. We conclude that haloes in a cosmological environment do not clearly show the behaviour noted by [23] but have a more complex nature instead. For a definite conclusion on that topic, we need a better statistic of haloes above the mass limit.

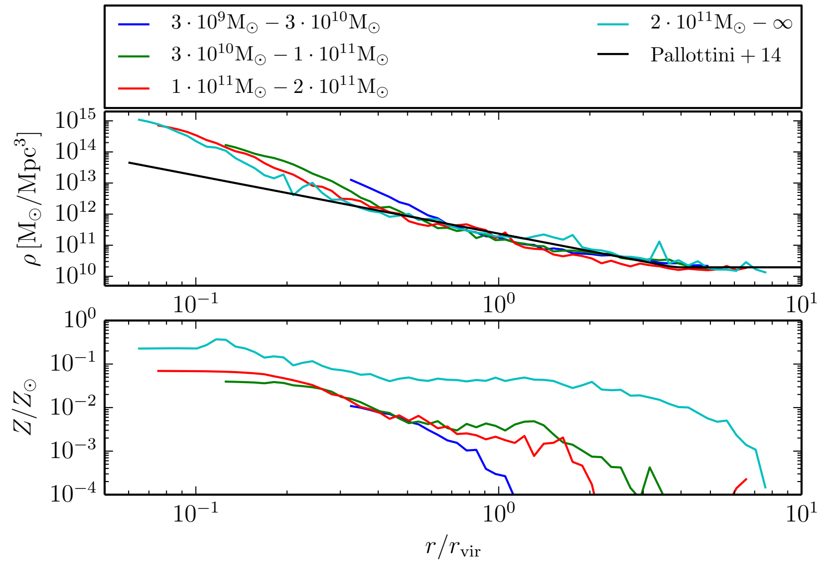

Figure 5.8: Stacked halo profiles similar to 5.7 but for a redshift of $z = 4$ and only showing baryonic density and metallicity.

5.2 Varying the fundamentals

In the previous section, we introduced our analysis methods and showed that our fiducial model gives reasonable results. In this section, we are going to discuss the basic parameters and other influences. This collection of rather different topics can also be seen as an argument in favor of the robustness of the results presented in the following section. In many cases, we vary one parameter independently of all others to quantify its influence, although there are other parameters which are deeply connected to the studied ones. In this section, we do not only compare to the *fiducial* simulation but to a number of other simulations from different stages of our research project. For example, we use the *alldiff* simulation as "old fiducial". The difference between both is discussed in section 5.3.1.

5.2.1 Sample variance

In this section we analyse the influence of the initial conditions while keeping the parameters fixed. Technically, we vary the random seed for the generation of initial conditions. Or from a more physical point of view: we look at three different patches of the universe. Figure 5.9b shows the evolution of the stellar density for three different initial conditions. Two of them (*fiducial* and *ic_c*) are similar and reproduce the observations pretty well, while *ic_b* significantly underpredicts the stellar density. Turning to star formation rates, we find similar results. *ic_c* shows lower star formation rates than *fiducial* at early times and higher ones at late times. The star formation in *ic_b* is again off by far.

Figure 5.9c compares the halo mass functions for the three initial conditions at $z = 2$. Up to $2 \cdot 10^{11}$ $M_\odot$, the halo mass functions do not differ significantly. At higher masses, the simulation *ic_b* does not have any haloes while the other two contain up to two haloes with more than $5 \cdot 10^{11}$ $M_\odot$.

Turning to figure 5.9d, we find that the stellar mass-halo mass relation shows corresponding similarities in the mass range up to halo masses of 10^{11} $M_\odot$. At higher halo masses, *ic_b* does not produce stars since it misses haloes of this mass. We conclude that in our model star formation depends on the available gas, proxied by the halo mass, in the expected way. This also explains the rather large differences in the stellar density, since the stellar mass in haloes of more than $3 \cdot 10^{11}$ $M_\odot$ in the *fiducial* simulation easily accounts for the difference. Furthermore, this result supports our analysis in section 5.1.2.

5.2.2 Reducing stellar feedback

Figure 5.10 compares a simulation with full feedback with one in which feedback is scaled down by 0.2. One can clearly see that the deficient feedback variant is producing more stars, whereas the former simulation exhibits a little more spikey behaviour. The increase in star formation happens at early times while, at late

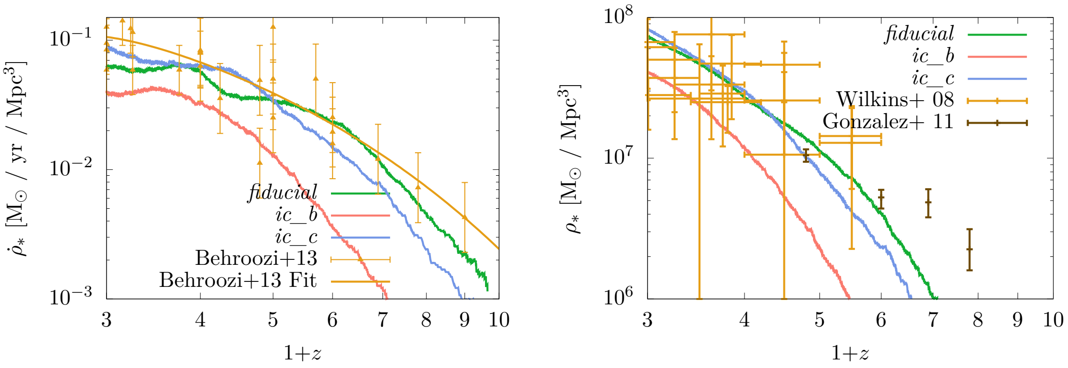

(a) Global star formation rate

(b) Global stellar density

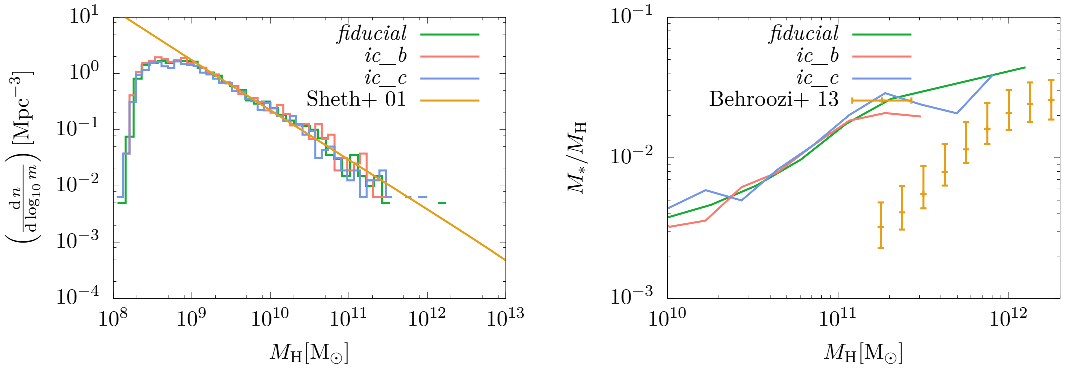

(c) Halo mass function

(d) Stellar mass-halo mass relation

Figure 5.9: Stellar history and mass functions for different initial conditions. The mass functions are given at $z = 2$. For details of the plots, see figure 5.1 for the upper ones and figure 5.2 for the lower ones.

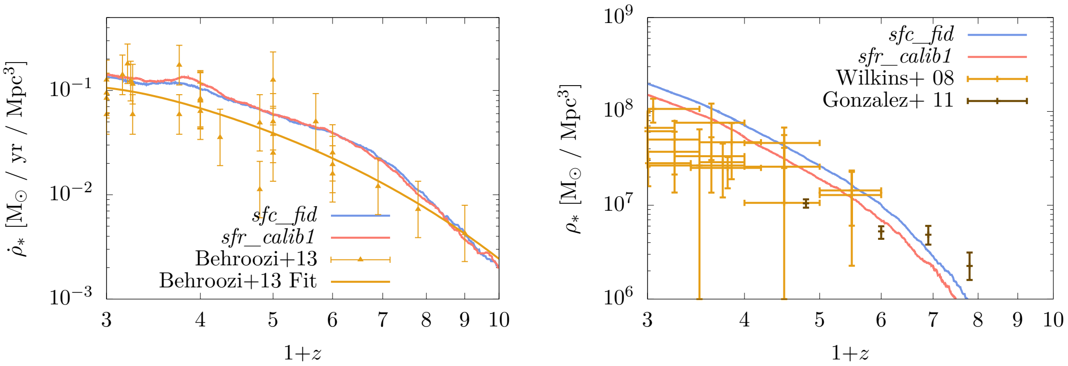

(a) Global star formation rate

(b) Global stellar density

Figure 5.10: Stellar history when artificially reducing the feedback using the parameter α_{FB}, which scales all feedback. The *sfc_fid* simulation features $\alpha_{\mathrm{FB}} = 0.2$ while the *sf_calib1* simulation is using the full feedback ($\alpha_{\mathrm{FB}} = 1$). The plot is of the same type as figure 5.1.

times, the star formation rates of the simulation with full feedback exceed the other one from time to time. This indicates that feedback is most important in early, low-mass haloes.

5.2.3 Calibrating star formation

In this section, we investigate the influence of the two free parameters in our star formation prescription, δ_{SF} and ϵ_{FF}. δ_{SF} is the overdensity (compared to cosmic mean) above which star formation is allowed, and ϵ_{FF} is an efficiency parameter, determining how much of the gas available for star formation is actually transferred to stars. For details on our star formation prescription, see section 4.2.

For star forming cells, we find a simple relation between the two parameters and the local production of stars. We start our analysis with the set of equations 4.9 and equation 4.11. Assuming a star forming cell (i.e. $\rho \geq \delta_{\mathrm{SF}}\bar{\rho}_{\mathrm{B}}$) and a time average, we find

$$\begin{aligned} \langle \dot{m} \rangle &= \langle n \rangle m_* \\ &\propto \frac{\rho_{\mathrm{B}}\epsilon_{\mathrm{FF}}}{t_{\mathrm{FF}}} \\ &\propto \rho_B^{1.5}\epsilon_{\mathrm{FF}} \,. \end{aligned} \tag{5.3}$$

This shows that star formation locally scales with efficiency. When looking at global quantities, i.e. the star formation rate or the stellar density, we find that this scaling is not obeyed. In figure 5.11, we see that increasing the efficiency by a factor of 2 only leads to an increase in stellar mass by a factor of ~ 1.5[1]

---

[1] We refer the reader to our definition of relative quantities, as given in equation 5.1.

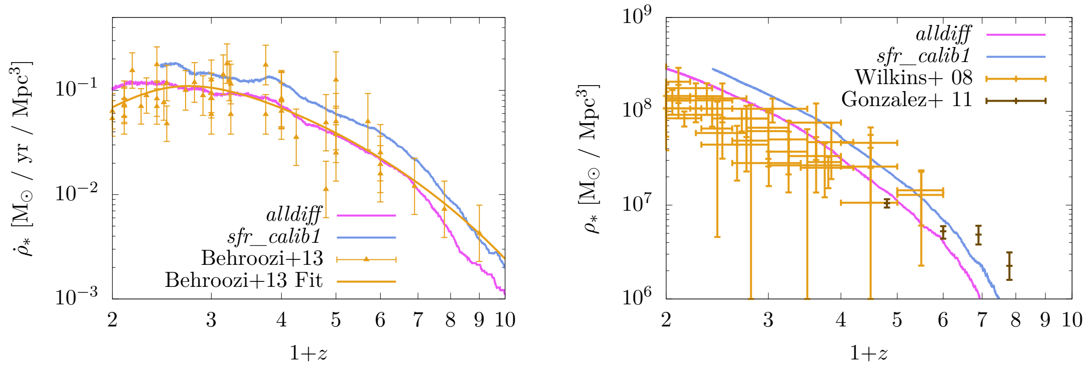

(a) Global star formation rate

(b) Global stellar density

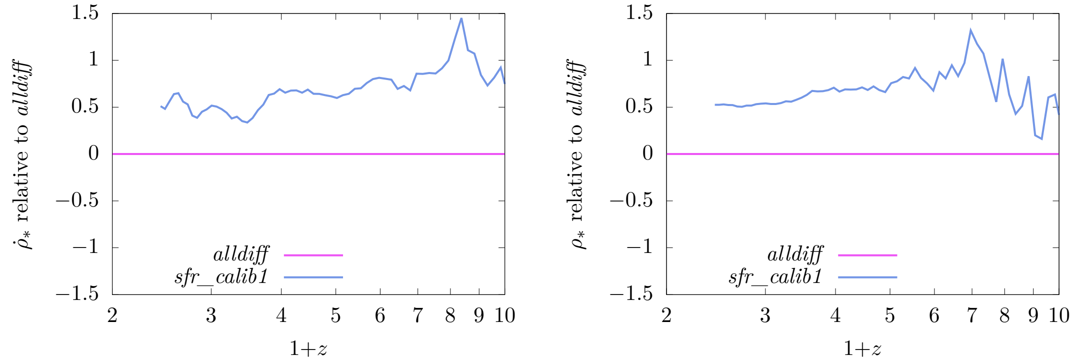

(c) Star formation rate relative to *alldiff*

(d) Stellar density relative to *alldiff*

Figure 5.11: Stellar history when varying the star formation efficiency ϵ_{FF}. *sf_calib1* employs $\epsilon_{\mathrm{FF}} = 0.01$, and *alldiff* $\epsilon_{\mathrm{FF}} = 0.005$. For details on these plots, we refer to figure 5.1 and equation 5.1.

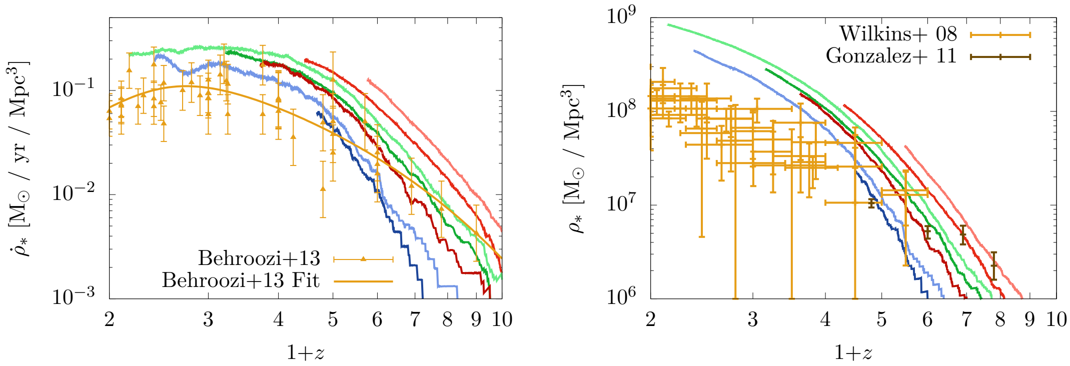

(a) Global star formation rate

(b) Global stellar density

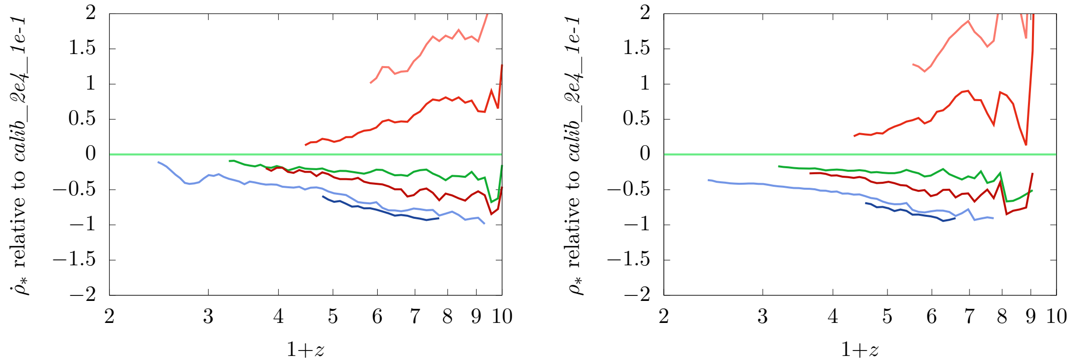

(c) Relative star formation rate

(d) Relative stellar density

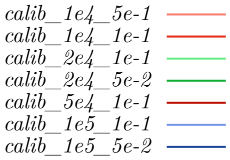

(e) Legend

Figure 5.12: Simulations sampling the δ_{SF}-ϵ_{FF} parameter space. The first number in each simulations name is the assumed value for δ_{SF}, while the second one is the efficiency ϵ_{FF}. The figure is of the same type as 5.11.

at redshifts below 5. At higher redshifts, the relative changes are dominated by the randomness of star formation. The difference between local scaling and global results is expected since star formation is the result of a complex network of interdependent processes. An increase in star formation, for example, also leads to an increase in stellar feedback which inhibits or decreases further star formation.

In figure 5.12, we show a comprehensive suite of simulations covering a large part of the parameter space. As the influence of the SGS model will be extensively discussed in the next subsections, we initially explore here the effect of star formation and stellar feedback in the absence of SGS models. The feedback in these runs is artificially reduced by a factor of 0.2, which has made these simulations computationally more efficient. While this set of simulations employed a different realization for the initial conditions, they nevertheless give a good impression on the influence of the relevant parameters. Some of the simulations have been terminated as soon as it became apparent that they would not deliver a good fit to the observed star formation rate.

First of all, all simulations presented in figure 5.12 significantly overpredict star formation and stellar density. This is partly due to weak feedback and due to the initial conditions. As we demonstrate in section 5.2.1, the initial conditions B lead to dense structures only rarely and at unusually late time. Therefore, the shapes of the star formation rates and stellar densities do not reproduce the observations. Most important, these simulations do not employ the SGS model, which has a significant influence, as we will see in section 5.3

When comparing the simulations with different star formation density thresholds, one can see that star formation starts later for a higher threshold. This can be understood easily since strong density peaks need time to form. In order to get the early star formation right, we choose a rather low density threshold.

Having fixed one parameter, we can use the efficiency ϵ_{FF} to tune the star formation rate to the observed behaviour. Figure 5.12 indicates that, independently of the large initial deviations, all of the simulations eventually converge to similar star formation rates (and to a lesser degree similar stellar densities). This is probably due to our sampling of the parameter space, which keeps the product of ϵ_{FF} and δ_{SF} within one order of magnitude. This behaviour can be understood by using equation 5.3, especially if we assume a density exponent of one, which is obtained for a constant star formation time scale.
Another, more physical, explanation is that self-regulation between star formation and stellar feedback leads to similar star formation rates. In the case of a low density threshold, strong initial star formation leads to strong stellar feedback which in turn decreases star formation subsequently. On the contrary, for high density thresholds, star formation and therefore stellar feedback are initially weak. Following this line of argumentation, a decrease of star formation at low redshift has to be obtained by stronger feedback.

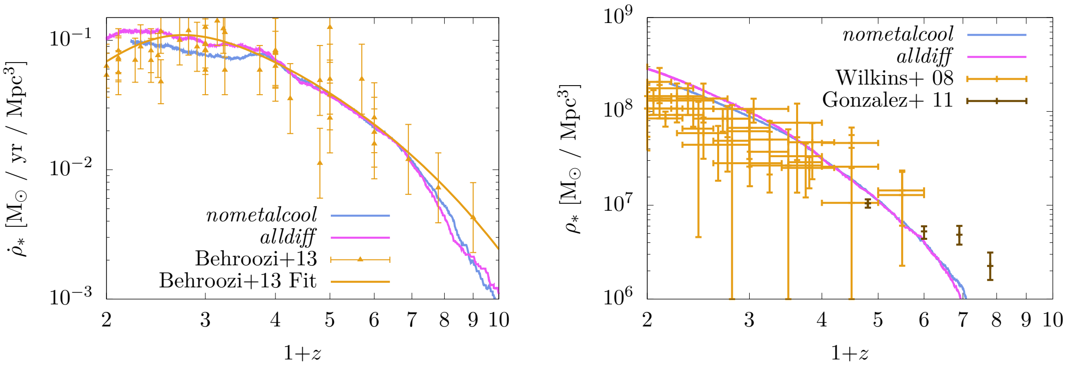

(a) Global star formation rate

(b) Global stellar density

Figure 5.13: Stellar history for a simulation with and without metal cooling. For a detailed description of the plot, see figure 5.1.

Having discussed the influence of the two parameters ϵ_{FF} and δ_{SF}, we focus on our choice for these parameters for the remainder of this section. As discussed above, we employ a low threshold density and a low efficiency, to get an early onset of star formation and a well-converged star formation rate throughout the simulation, as demonstrated for the *fiducial* model in section 5.1.1.

5.2.4 Metal cooling

Figure 5.13 shows the stellar history for two simulations, which only differ in whether metal cooling is switched on or off. We find that the effect of metal cooling is rather small, which is comparable to findings of Shen et al. [94]. In contrast, Smith et al. [99] find a larger deviation although at a coarser resolution. In both simulations we employ turbulent internal energy diffusion, which means that the internal energy is distributed by turbulent mixing. As we will discuss in section 5.3.1, turbulent internal energy diffusion strongly decreases the efficiency of feedback. Furthermore, Schaye et al. [84] find that metal cooling is an important channel for radiating away the energy injected by stellar feedback. For this reason, we are confident that a corresponding pair of simulations without turbulent internal energy mixing would give a stronger suppression of star formation when metal cooling is switched off, as the literature indicates, since in section 5.3.1 we find that turbulent internal energy diffusion enhances cooling significantly.

5.2.5 Star formation criteria

In the literature, there is a number of different criteria for star formation in cosmological simulations, a selection of which is discussed in section 4.2.3. We run a suite of four simulations to determine whether any of these additional criteria has

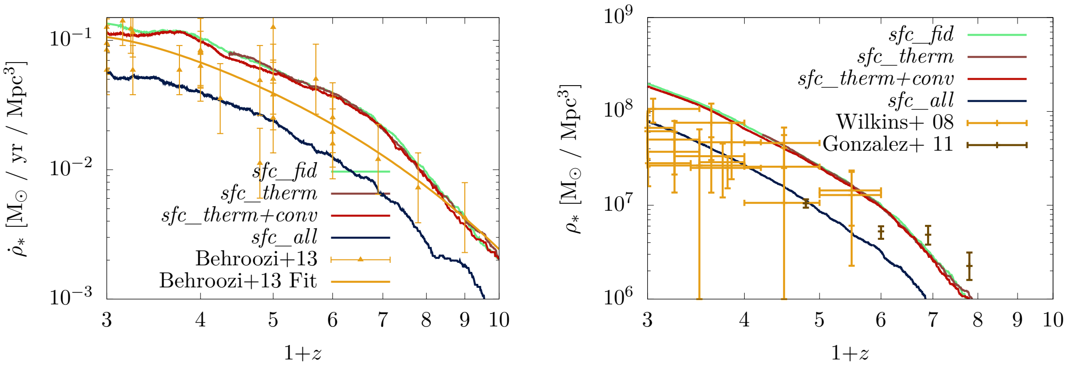

(a) Global star formation rate (b) Global stellar density

Figure 5.14: Stellar history for simulations with the same star formation parameters but different star formation criteria. The plot is of the same type as figure 5.1.

name	thermal restrictions	converging flow	Jeans criterion
sfc_fid	X	X	X
sfc_therm	✓	X	X
sfc_therm+conv	✓	✓	X
sfc_all	✓	✓	✓

Table 5.4: Overview over the different simulations performed for studying the influence of different star formation criteria.

an influence. Again, these simulations employ artificially reduced feedback and turbulent internal energy diffusion.

Figure 5.14 shows the resulting stellar histories when successively enabling additional star formation criteria. An overview over the simulations and the criteria is given in table 5.4. We find that the thermal restrictions do not make a difference. The thermal restriction criterion allows star formation in cells where the cooling time is faster than the free-fall time or the temperature is below $5 \cdot 10^4$ K. The ρT plot in figure 5.3 shows that, at $z = 2$, the latter criterion is fulfilled for all cells meeting the density threshold for star formation. Therefore, the result that thermal restrictions do not make a difference, is not too surprising. When we add the necessity for a converging flow to the list of criteria, we, again, do not find a significant difference. The only criterion making a difference is the Jeans criterion. It allows for star formation only in cells where the Jeans length is smaller than the cell size. The Jeans criterion is similar to the thermal criterion since it sets a combined limit on the temperature and density of a cell. Nevertheless, the concrete limits imposed by it are different from the other criteria.

Our result contradicts the one by Smith et al. [99], who find that, for large scale simulations, the Jeans criterion can be omitted safely as a cost-saving measure.

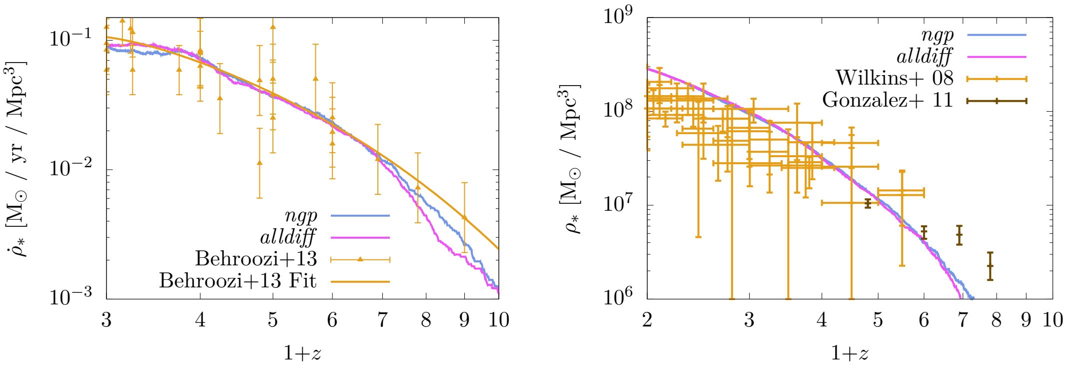

(a) Global star formation rate

(b) Global stellar density

Figure 5.15: Stellar history for a simulation with distributed feedback (*alldiff*) and without (*ngp*). For details of the plot, see figure 5.1.

This is probably due to the fact that we use a higher resolution. With respect to higher resolution (i.e. smaller cell-sizes), the Jeans criterion enforces the Jeans length to be smaller. This leads to increasingly stronger bounds on both temperature and density. If we assume the gas to be in photoionization equilibrium, temperature is approximately constant and higher resolution leads to a scaling of minimal density with $1/(dx)^2$.

5.2.6 Feedback distribution

Our model distributes the stellar feedback on 27 cells using the cloud-in-cell formalism. It is not a priori clear whether this has an influence on the resulting distribution of metals in a halo or the efficiency of feedback. Our approach is similar to the one by [99] and [11]. Smith et al. [99] argue that distributed feedback is able to overcome the overcooling problem since injecting all feedback into one cell would "unphysically" increase the temperatures and thereby the cooling rates. We do not find the influence to be that strong, i.e. the star formation rate is affected only mildly and the stellar density is unaffected. Oppenheimer et al. [70] explicitly criticize the distributed feedback in Smith et al. [99] as artificially smearing out metals. In contrast, figure 5.16 shows for a particular halo that in our case distributed feedback does not introduce a bias. This conclusion holds for all haloes.

5.2.7 Box size and resolution

Star formation is highly resolution-dependent, therefore one has to calibrate each resolution. This is due to the fact that higher resolution allows for stronger gravitational collaps and higher density peaks. Higher densities lead to an increase

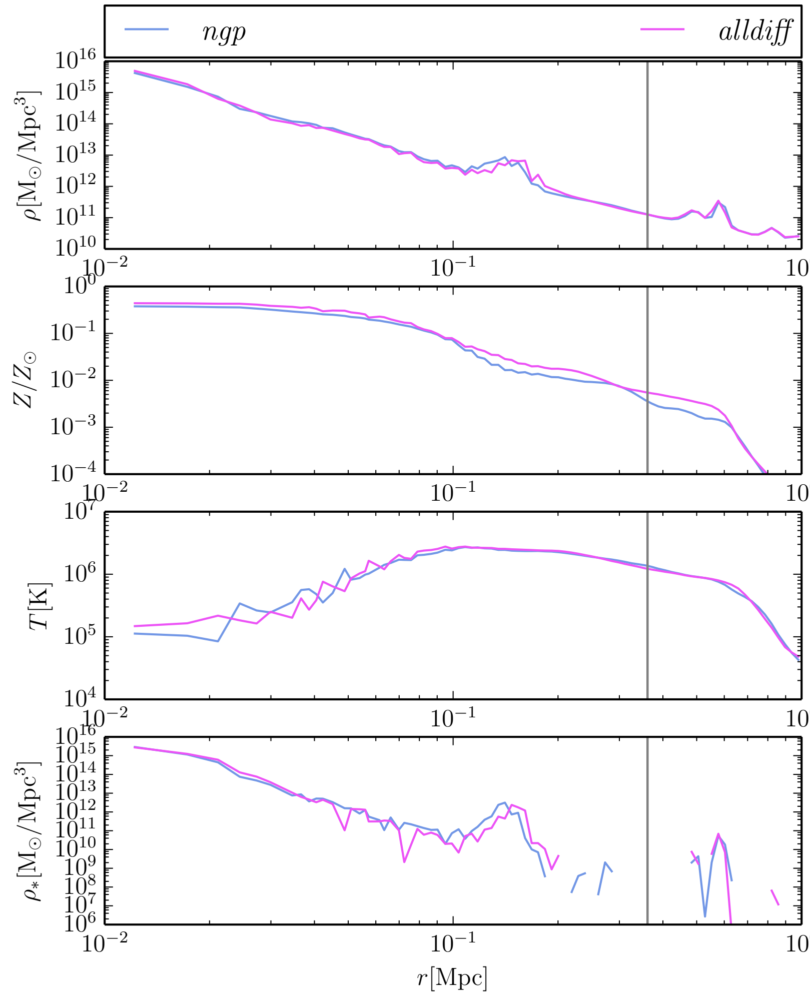

Figure 5.16: Profiles of halo 0 when varying whether the feedback is distributed over several cells (*alldiff*) or not (*ngp*). This plot is of the same type as figure 5.6.

in star formation, which, in turn, is not compensated with the same efficiency by stronger feedback. This effect is well-known in other simulations. For example, Dubois and Teyssier [17] find that “the two parameters [. . .] are poorly known and scale-dependent”. This scale-dependence is especially severe in our case, which might be overcome by including a scale-dependent star formation criterion.

For box size, we refer to section 5.1.2 where most of the effects of different box sizes are already discussed.

5.3 The influence of turbulence and mixing processes

In the previous two section, we discussed validity and robustness of our model in general and when varying fundamentals. In contrast, we focus on the influence of the various turbulent ingredients of our model in this section. Since turbulence in the context of star formation and stellar feedback has rarely been studied in the literature, this section is the heart of this work. For this, we keep fixed the parameters discussed in the previous section (especially star formation efficiency, star formation overdensity and initial conditions).

5.3.1 Turbulent internal energy diffusion

In this section, we analyze the influence of turbulent internal energy diffusion (TIED). Although being a standard ingredient of turbulent subgrid models, we find that it has a large impact on all kinds of quantities in our simulations. To analyse this, we performed four simulations, one without any turbulent diffusion at all (*fiducial*), one with internal energy diffusion (*intediff*), one with turbulent diffusion of species (*specdiff*), and one where both kinds of turbulent diffusion are enabled (*alldiff*). We discuss the influence of turbulent species diffusion in the following section (5.3.2) and focus on the influence of TIED here.

Figure 5.17 shows the stellar history of the four simulations in question. It shows that switching on turbulent internal energy diffusion greatly enhances star formation. At $z = 1$, star formation rates for both simulations with TIED each are larger by a factor of two than the rates for the simulations without turbulent diffusion. The result for stellar mass is similar, both simulations with TIED contain about 70 % more stars. At first glance, this is an unexpected result.

For a better understanding, we look at the probability distribution function (PDF) of temperature in the four simulations at $z = 2$ in figure 5.18. Towards the low end, we find a small number of cells at very low temperatures when TIED is switched off. When switched on, that amount of cells is significantly smaller. Therefore, TIED smears out temperature fluctuations, just as we expected. Turning to the high end of the PDF, the simulations with TIED exhibit a volume at 10^6 K smaller than the simulations without TIED. Additionally, their maximal temperatures are significantly lower. The reason behind this is again the very nature of TIED: The hot cells are heated up by stellar feedback and become very turbulent. Therefore, they efficiently distribute feedback energy to their surroundings and thereby lower temperature. Additionally, the nonlinear nature of the cooling function comes into play. Figure 4.1 shows that hot dense gas is cooling inefficiently and that its cooling rates increase with decreasing temperature. Through this mechanism, the cooling time scale for cells with temperature peaks is significantly decreased.

Figure 5.19 compares the temperature versus overdensity phase plots when switching turbulent internal energy diffusion off (*fiducial*) and on (*intediff*). First

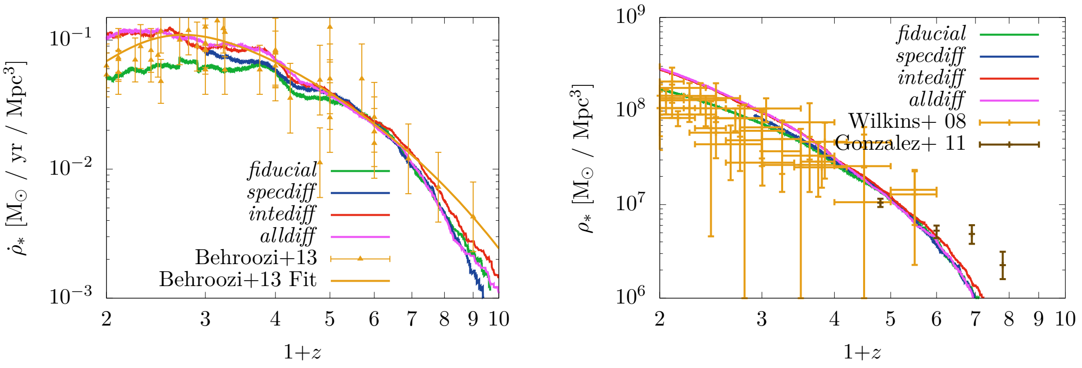

(a) Global star formation rate

(b) Global stellar density

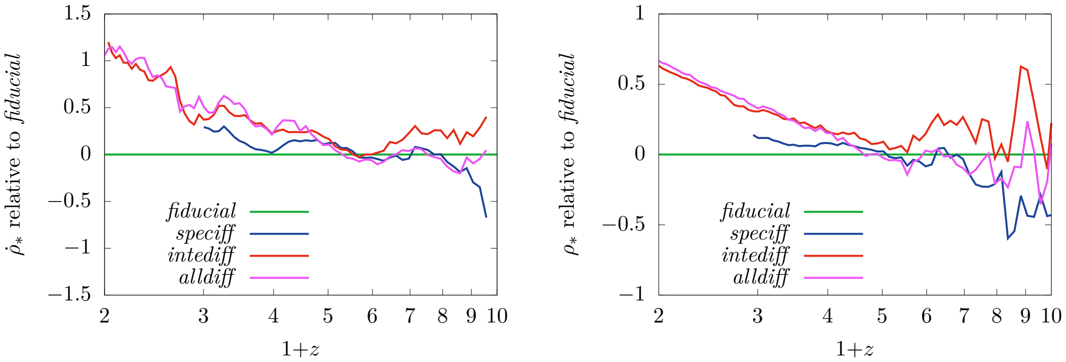

(c) Star formation rate relative to *fiducial*

(d) Stellar density relative to *fiducial*

Figure 5.17: Stellar history when simulating all combinations of de/activated turbulent diffusion. For simulation names, we once again refer to table 5.1, for details of this figure, we refer to figure 5.11.

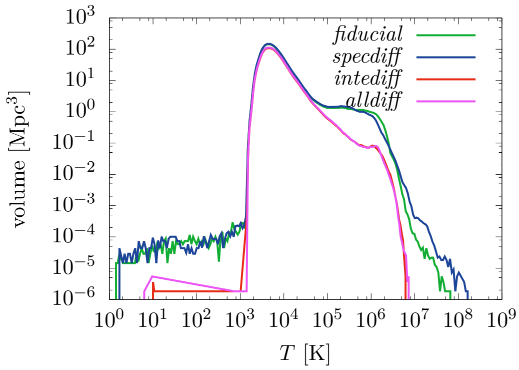

Figure 5.18: Probability distribution functions of temperature at $z = 2$ for the set of simulations dealing with turbulent diffusion.

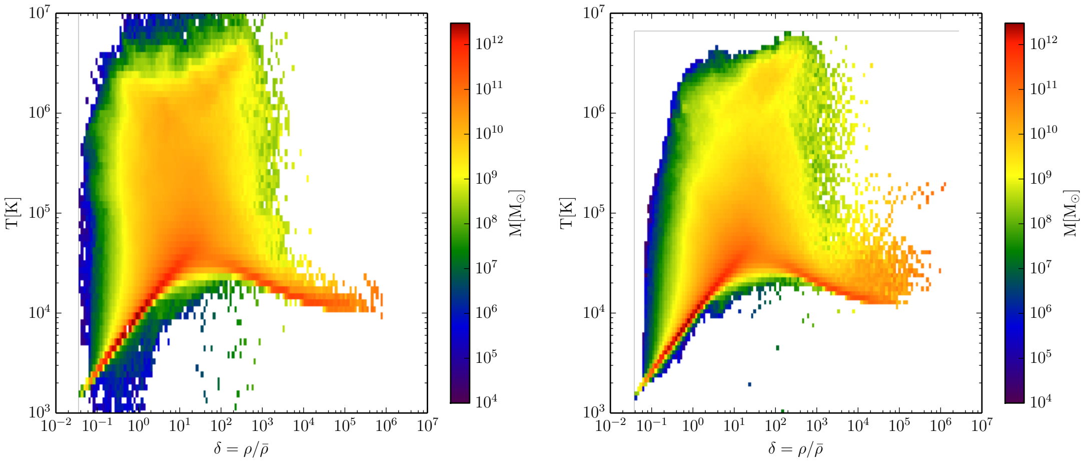

(a) Full box / *fiducial* (b) Full box / *intediff*

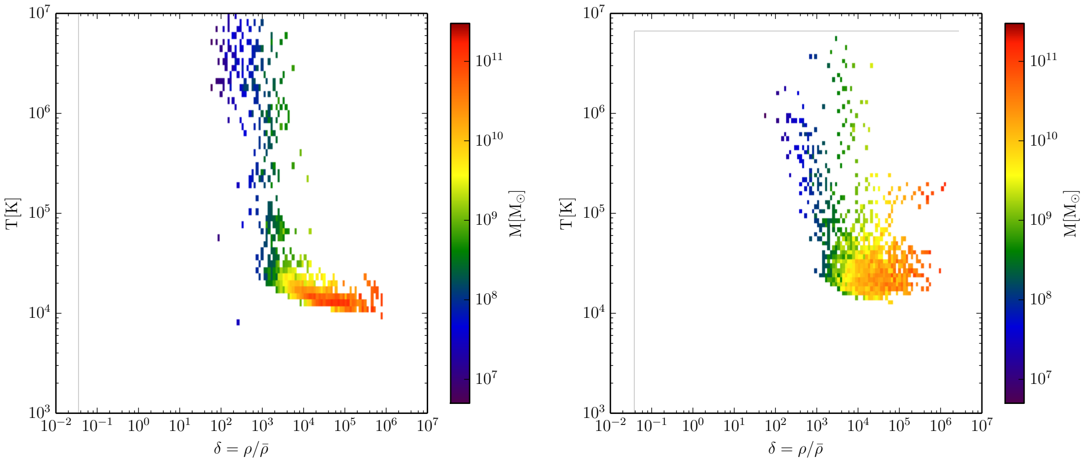

(c) Cells with active feedback / *fiducial* (d) Cells with active feedback / *intediff*

Figure 5.19: Phase diagrams (temperature versus overdensity) shown for the full box and restricted to cells with active stellar feedback at $z = 2$, comparing the simulations *fiducial* and *intediff*.

of all, we find that both plots agree in their general shape. The *intediff* simulation exhibits slightly less gas in the high temperature and low density regime. This, again, is due to diffusion.

The most interesting aspect of this plot is the tail at high densities and at moderate to low temperatures (i.e. the condensed phase) which is much more compact in the case without TIED. For the simulation with TIED switched on, in contrast, this tail is much more spread out. In simulations without feedback, the condensed-gas tail is very thin since there is no process producing additional pressure at high densities. This may lead to the impression that feedback is inefficient without TIED. Yet, in the following parts of this section, we show that the contrary is the case: The efficiency of feedback is reduced by TIED.

The lower panels of the plot show the same diagnostic, but this time restricted to cells with active feedback. They depict that the difference in the condensed phase is correlated with feedback. In both simulations, feedback happens in the condensed phase as well as in the WHIM and in the hot phase. The WHIM phase is usually associated with the outskirts of galaxies, but this is not the case here. Instead, feedback has driven out most of the gas in these cells and simultaneously heated them.
The condensed phase is again very thin in the *fiducial* simulation. In contrast, the tail is much more spread out in the *intediff* simulation. The reason behind this is that the feedback energy injected into cells in the *intediff* simulation is dispersed via TIED to the surrounding cells. Consequently, these cells are heated only to intermediate temperatures, which cool more efficiently. In contrast, in the *fiducial* simulation, feedback is able to heat up the cells significantly and also to push out the gas, leading to the very hot and thin cells, of which more are present in the *fiducial* simulation. This already indicates that feedback is more efficient when TIED is turned off.

Having discussed global quantities, we now turn to single haloes. Figure 5.20 shows slices at $z = 2$ through halo 0 in simulations with and without TIED. Halo 0 is the most massive halo in each simulation and shows large outflows. Nevertheless, a significant decrease in outflows in simulations with TIED is apparent. While the metal-enriched gas reaches beyond the borders of the panel in the *fiducial* case, it is mostly confined within the virial radius in simulations with TIED. Temperature and turbulent subgrid energy exhibit a similar behaviour. Even the accretion shocks are closer to the halo center for the TIED case. In contrast, the *fiducial* simulation shows areas inside the accretion shocks that are metal-rich but only moderately hot and mildly turbulent.

An even more striking example is halo 4, of which we show slices at $z = 2$ in figure 5.21. In the simulations without TIED this halo shows large outflows and a lot of metal-enriched and hot gas. In the simulations with TIED, the halo and its surroundings fill only a small fraction of the panel. At least in these slices, we find a significant difference in the efficiency of feedback with respect to TIED. To

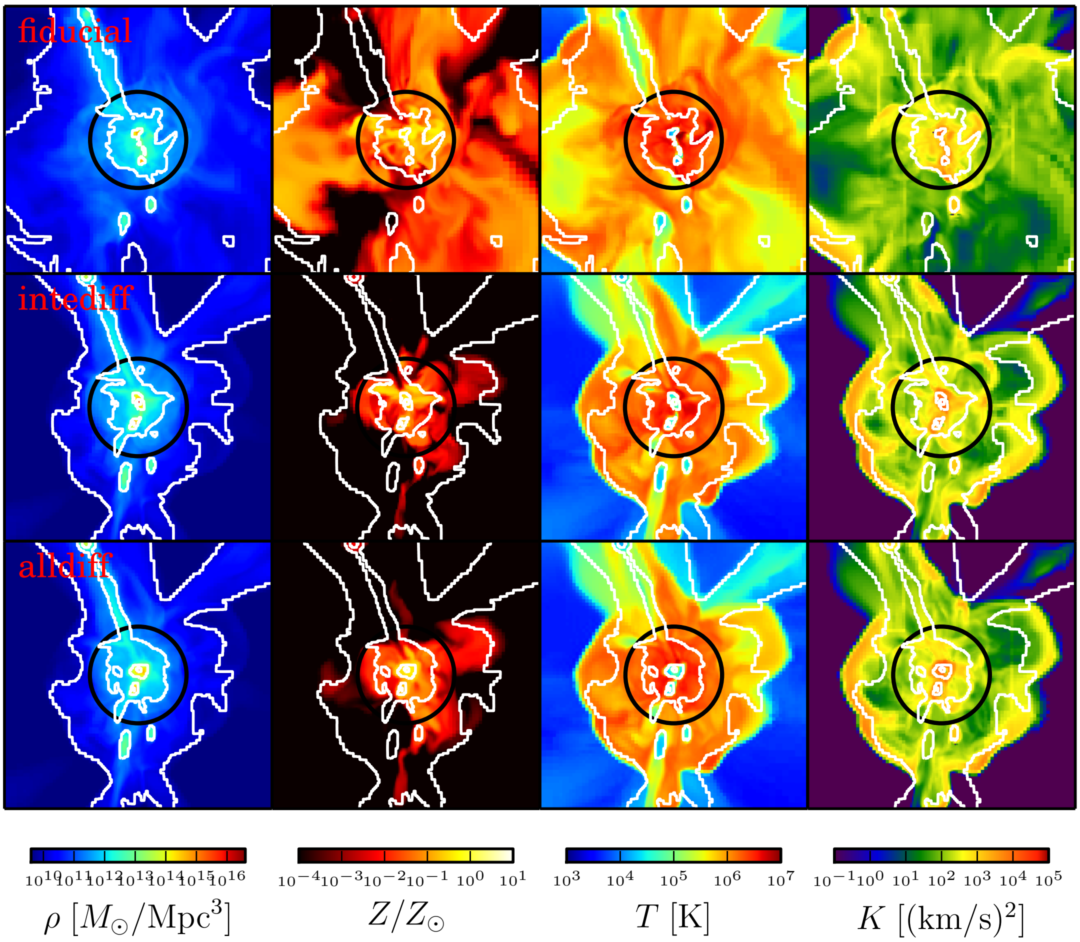

Figure 5.20: Halo 0 in the set of simulations dealing with turbulent diffusion. Each panel has a width of 2 Mpc. The details of the plot are explained in figure 5.4. We omit the *specdiff* simulation since it produces unrealistic metallicities in and around halo 0.

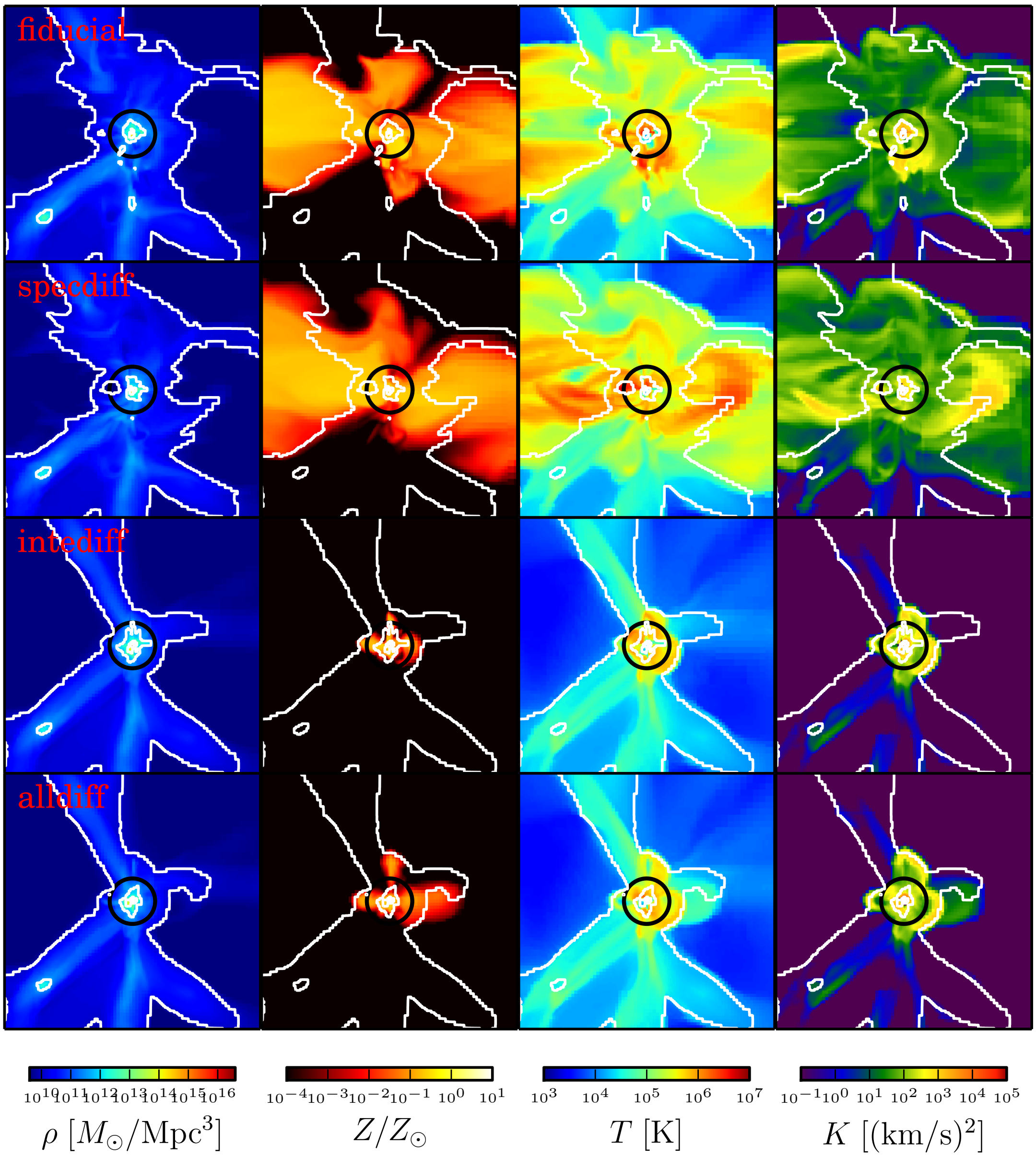

Figure 5.21: This figure shows halo 4 but is otherwise identical to figure 5.20.

give a more quantitative analysis, we show profiles of halo 4 in figure 5.22. First of all, we note that density distribution is pretty similar between simulations with and without TIED. The same is true for stellar density (apart from the *specdiff* simulation, which we do not consider here) and, to a lesser degree, for turbulent subgrid energy. In contrast, metallicity is similar in the central region of the halo, but very different around and beyond the virial radius. For the simulations with TIED, metallicity changes its slope around the virial radius while, for the simulations without TIED, the slope is shallower for all radii and there is no turn-off point in the range of radii plotted here. In temperature profiles, we again neglect the inner 100 kpc due their dependence on momentary state of feedback. Further out, temperature declines gradually for the simulations without TIED while it declines sharply just above the virial radius with TIED switched on. The profiles verify the results we found in the slices: Turbulent internal energy significantly reduces maximal radius affected by feedback.

By now, we discussed single haloes and their properties. For a more comprehensive analysis, we plot stacked profiles of all haloes with masses larger than 10^{11} $\mathrm{M}_\odot$ at $z = 2$ in figure 5.23. The figure shows, again, that the density profiles do not differ; the small differences seen in the single haloes are averaged out. Consequently, feedback does not transport significant amounts of mass outward, even in the simulations where it is most efficient. Metallicity in the simulations with TIED shows a plateau ranging from inside the virial radius to approximately three times the virial radius, after which metallicity slowly declines. In contrast, the simulations without TIED show a steady decline with an approximately constant slope that is similar to the one the simulations with TIED exhibit inwards and outwards of the plateau. Temperature shows significant differences as well. The simulations without TIED reach higher temperatures and maintain them for larger radii. In the simulations without TIED, the radius at which the profiles decline and their slopes are similar for temperature and metallicity. The inner part of the temperature profile shows that the simulations without TIED exhibit colder cores. While this difference could be explained with TIED, this result is not conclusive because of the scatter in the single halo profiles. The profiles of turbulent subgrid energy agree out to a few times the virial radius, but outwards the simulations without TIED again show a plateau, which reaches a little farther out than the ones in the metallicity and temperature profiles. These plateaus are due to the large volumina which are dominated by outflows. The decline in turbulent subgrid energy marks the outer edge of the accretion shocks. Consequently, the absence of TIED leads to a large volume inside the accretion shocks. If one defines the circumgalactic medium (CGM) as the area that is dominated by the galaxy, then the simulations without TIED predict a CGM that is larger by a factor of approximately five in haloes of more than 10^{11} $\mathrm{M}_\odot$.

Figure 5.24 shows profiles for haloes with masses in the range of 10^{10} $\mathrm{M}_\odot$ to 10^{11} $\mathrm{M}_\odot$. In general, the results agree with what we found for the more heavy haloes, but

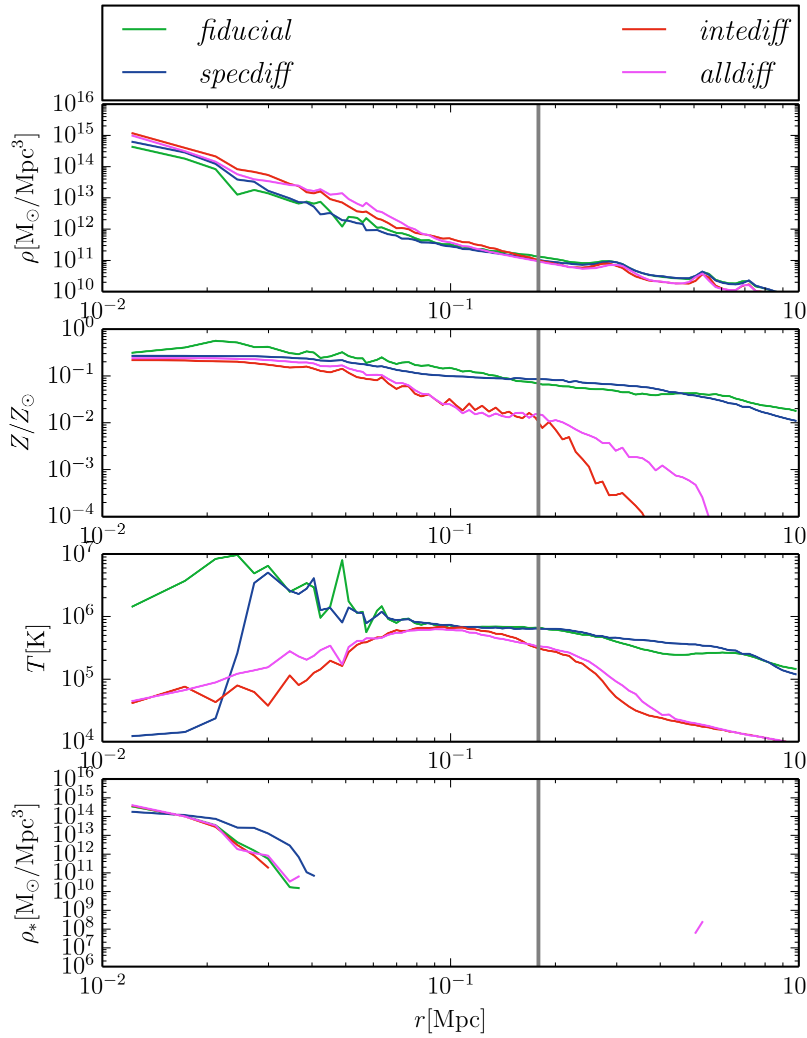

Figure 5.22: Profiles of halo 4 for the four simulations performed to analyze turbulent diffusion. Details of this plot are given in figure 5.6.

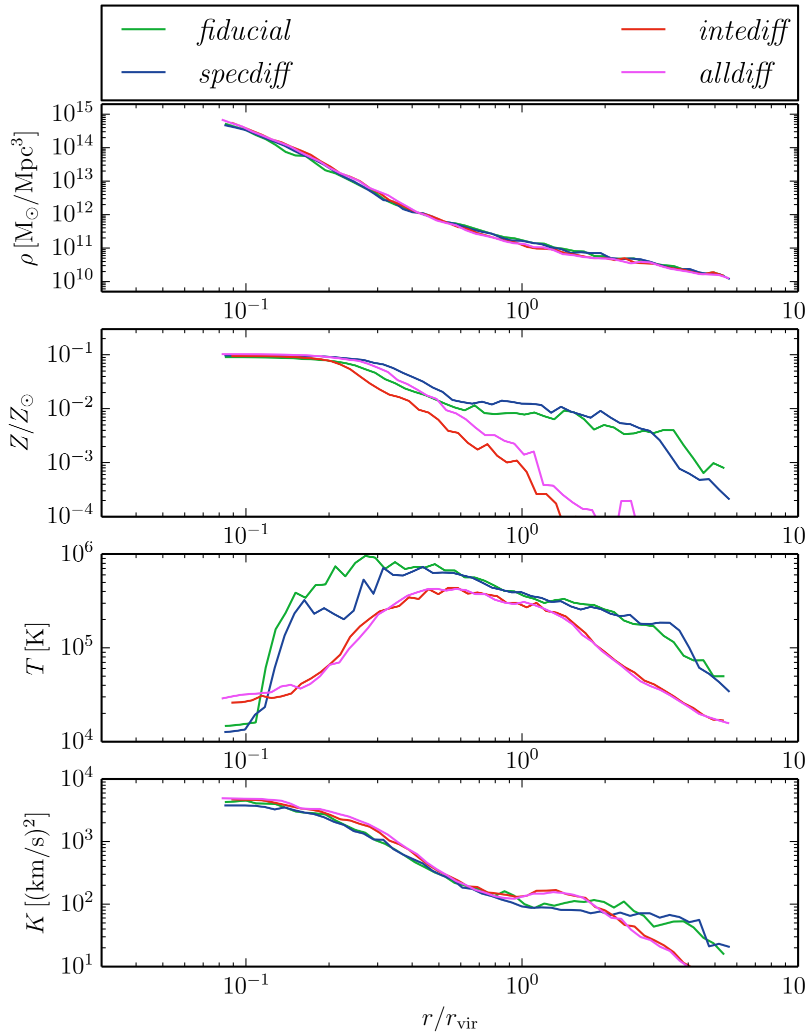

Figure 5.23: Stacked profiles at a redshift of $z = 2$ taking haloes with more than 10^{11} $\mathrm{M}_\odot$ into account, excluding halo 0.

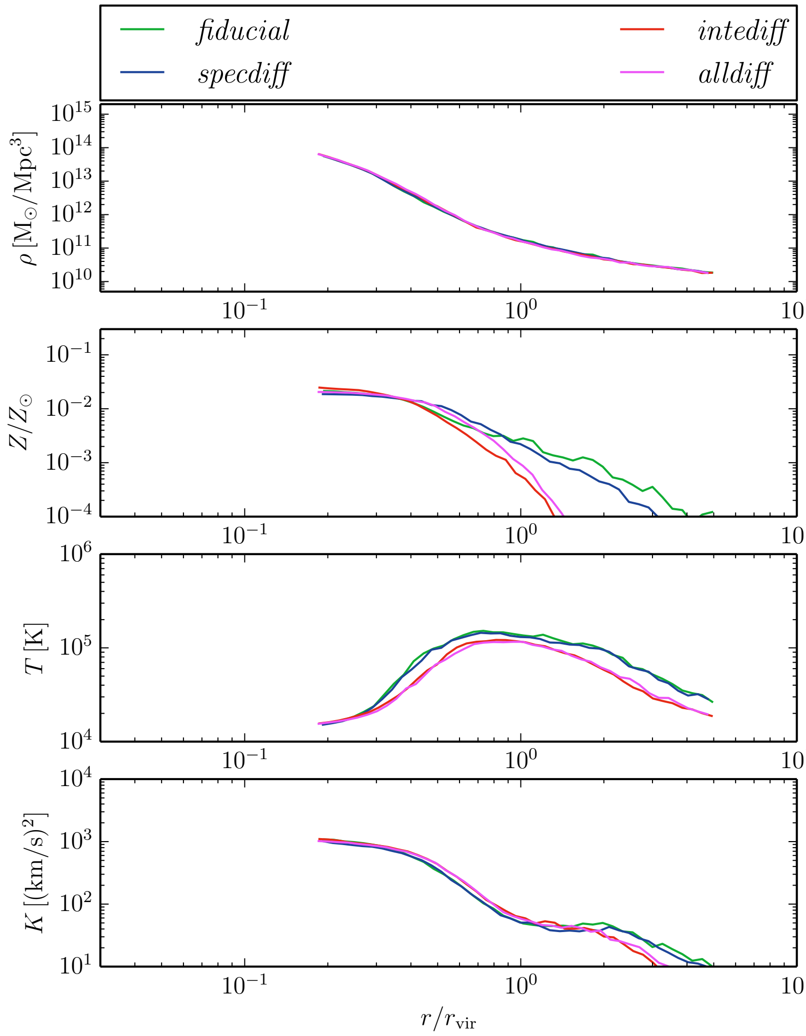

Figure 5.24: Stacked profiles for haloes in the mass range from $10^{10}\,\mathrm{M}_\odot$ to $10^{11}\,\mathrm{M}_\odot$. Apart from the mass range, this figure is otherwise identical to 5.23.

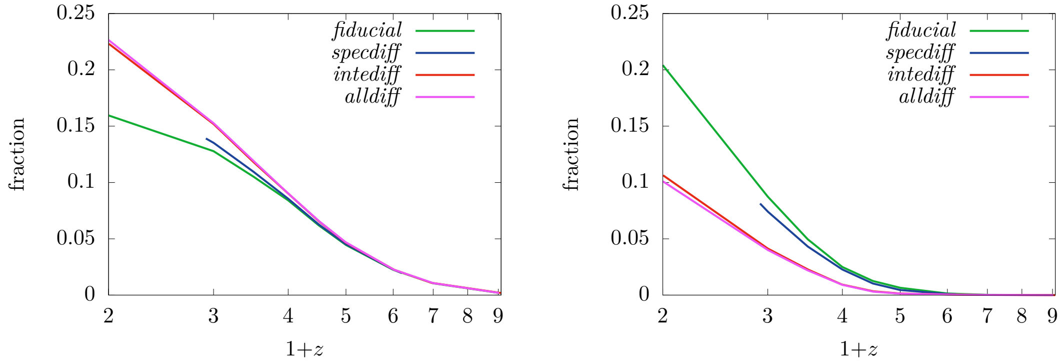

(a) Condensed phase

(b) WHIM phase

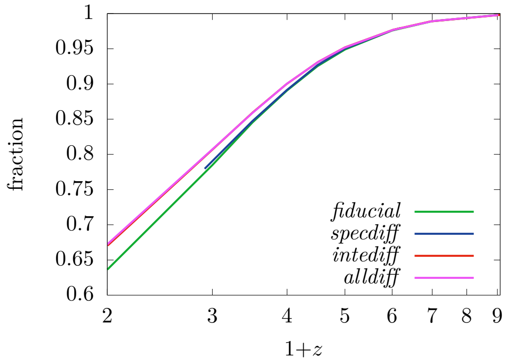

(c) Warm phase

Figure 5.25: Evolution of the global fractions of gas phases (see table 5.2) as a function of redshift. We omit the hot fraction since it is noisy, as discussed above.

the differences are less pronounced. Additionally, the temperature and metallicity profiles do not show plateaus. Less massive haloes (not shown here) exhibit even less deviations. This shows that TIED has a stronger impact on heavier haloes. This result somewhat contradicts a result by Fielding et al. [23], who find a strong dependence on the feedback parameters for haloes lighter than $10^{11.5}$ $\mathrm{M}_\odot$ and a robust behaviour for haloes heavier than that.

In figure 5.25, we show the gas phases as defined in table 5.2. As one would expect, we find a significant difference depending on TIED being used or not. In simulations without TIED, significantly less gas is found in the condensed phase and significantly more in the WHIM phase. This can be understood by the tremendous differences in feedback efficiency as discussed above. Additionally, the higher content in the condensed phase correlates with the higher star formation rate in the case with TIED. The differences in the warm phase (i.e. IGM-like phase) are less pronounced and harder to understand. Although the simulations without TIED exhibit very efficient feedback, they consumed more gas from the warm phase than

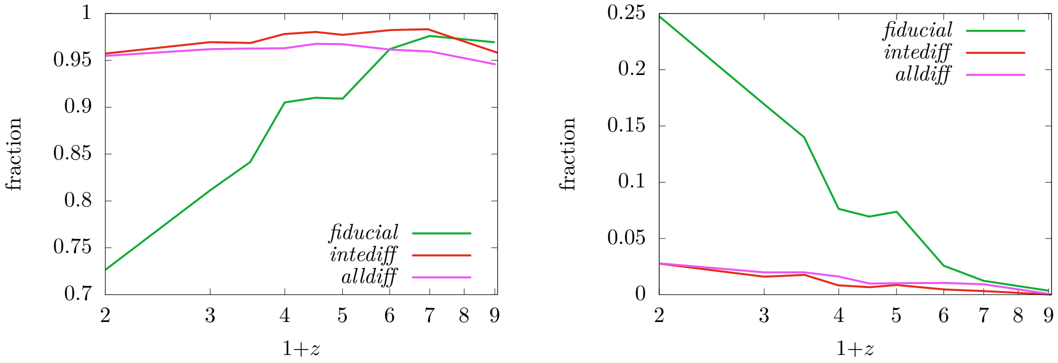

(a) Condensed phase (b) WHIM phase

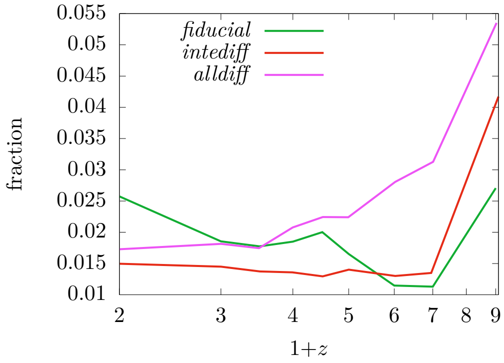

(c) Warm phase

Figure 5.26: Evolution of the fraction of metals in each of the gas phases over the total metal mass as a function of redshift. We omit the *specdiff* simulation since it contains one halo with defective metallicities.

the ones with TIED. This additional gas is in the WHIM phase. This is due to the fact that the accretion shocks are larger in simulations without TIED. Therefore gas flowing into galaxies is shock-heated at earlier time.

Figure 5.26 shows the distribution of metals over the gas phases. We note that the fraction is relative to total metal mass, which is growing as star formation and feedback progresses. The figure shows that, for simulations with TIED, most of the metals reside in the condensed phase and less than five percent reside in the WHIM or warm phase. In contrast, simulations without TIED exhibit an increasingly large fraction of metals in the WHIM phase that makes up to 25 %. The plateau in both curves between $z = 4$ and $z = 3$ correlates with a phase of low star formation activity and is probably related to a major merger event. The warm phase shows a more intricate behaviour. The fraction of metals in the warm phase, indicating the enrichment of the IGM, is largest at high redshifts in all simulations. But looking at the absolute metal masses in each phase, we find that this enrichment is tiny compared to later times. Whether TIED is switched on or off does not have a clear impact on the amount of metals in the warm phase.

Having analysed the influence of TIED on a multitude of quantities, we found that it has a huge and unexpected impact. But is it correct to switch off turbulent internal energy diffusion? Our answer is yes, due to the following reasons: Galaxies and their surroundings are inherently multiphase media, which are largely unresolved in our simulations. Since we cannot differentiate between warm and cold phases in turbulent and non-turbulent states on subgrid scales, the application of a single turbulent diffusivity to a temperature averaged over different phases is inadequate. Therefore, both options are physically inconsistent – switching TIED off is inconsistent since it happens in nature, while switching TIED on overpredicts the mixing in regions this work is concerned with.

5.3.2 Turbulent species diffusion

In this section, we discuss the turbulent diffusion of species (TDS). For this we analyse the same suite of simulations and the same figures as in section 5.3.1, in which we looked at turbulent internal energy diffusion. We note that in the *specdiff* simulation halo 0 exhibits implausibly high metallicities. This is due to our simple integration scheme for turbulent diffusion. A rerun of this simulation with smaller time step would have been ideal, but would also have been prohibitively expensive. This problem prevents us from doing a number of analysis steps with this simulation, but we are certain that we can nevertheless quantify the influence of turbulent diffusion of metals.

The global star formation history in figure 5.17 does not exhibit a strong dependence on turbulent diffusion of species, and the star formation rates are rather noisy. Stellar density is almost indistinguishable for the two simulations with turbulent internal energy diffusion (TIED) switched on. For the simulations without TIED, stellar density is enhanced by approximately 10 % at $z = 2$. The reason for this is that TDS leads to a broader distribution of metals which in turn decreases the cooling times for more gas. Consequently, star formation in those cells is more efficient. In the simulations with TIED, cooling is already efficient, so this effect does not have an influence.

The temperature PDF in figure 5.18 shows a behaviour similar to the stellar history. TDS does not make a difference in the simulations with TIED, but induces small deviations in those without. The lack of differences in the first case can be ascribed to metal cooling being a subdominant effect compared to TIED and its mechanism of mixing gas temperatures down to regions in which cooling is efficient. The changes in the simulations without TIED are difficult to explain with cooling properties: The PDF indicates slightly less gas in the range from 10^6 K to 10^7 K but more gas in the range from 10^6 K to 10^7 K. This is contrary to the aforementioned effect of stronger cooling, but is the other side of the effect of turbulent diffusion of species: Peaks of high metallicity are smoothed out and increase thereby the cooling time in cells with very high temperatures. Broadly speaking, TDS leads to a wider but flatter temperature PDF. The cells obtaining additional cooling are not visible in the PDF since they contribute to the well-populated peak around 10^4 K.

Figure 5.21 shows slices of halo 4. Comparing the two top panels (simulations without TIED), we find differences in the distribution of temperature and turbulent subgrid energy. These are probably due to different stages of feedback and not due to TDS. The distribution of metals is largely unaffected by TDS. The two lower panels (simulations with TIED) differ in a region in which metal-rich gas is ejected in the simulation with TDS. This ejection is also seen in temperature and turbulent subgrid energy and is therefore considered as an indication of ongoing feedback.

Again, a more quantitative approach is analysing profiles of haloes. Those of halo 4 are shown in figure 5.22. Density profiles do not exhibit significant differences. The same is true for the metallicity in the simulations without TIED whereas metallicity profiles in those with TIED differ; but this is probably due to the feedback ejection seen in the slices above. Ignoring the noisy inner part of the temperature profiles, these exhibit only minor differences when varying the TDS. The turbulent subgrid energy is systematically higher for the *specdiff* simulation than for the other three simulations.

The stacked profiles in figure 5.23 and 5.24 show that TDS does not transport metals farther out, as one might expect. Especially haloes in the mass range from 10^{10} $\mathrm{M}_\odot$ to 10^{11} $\mathrm{M}_\odot$ shown in figure 5.24 in the simulations without TIED exhibit the opposite. This effect is explained by the fact that diffusion is weaker than accretion, which constantly pushes (pristine) gas inwards.

In contrast to the negative results in the profiles, the simulation with TDS and without TIED contains a higher fraction of condensed gas, which supports the result from above that TDS enhances the efficiency of metal cooling. The same simulation also shows a lower content in the WHIM phase. This is explained by the same argument.

The fraction of metals in each of the gas phases in figure 5.26 shows that, for the simulations with TIED, TDS increases the metal content of the warm phase (i.e. the IGM). However, the effect is of the order of 1.5 around $z = 4$ and subsequently declines. A comparison of the simulations without TIED is not possible since we did not find a way to correct for the defective halo in the *specdiff* simulation.

In this section, we found that turbulent diffusion of species has a small influence on the star formation rates and the distribution of gas over the gas phases since it enhances metal cooling. However, we did not find evidence for the transport of metals out of galaxies into the CGM or IGM.

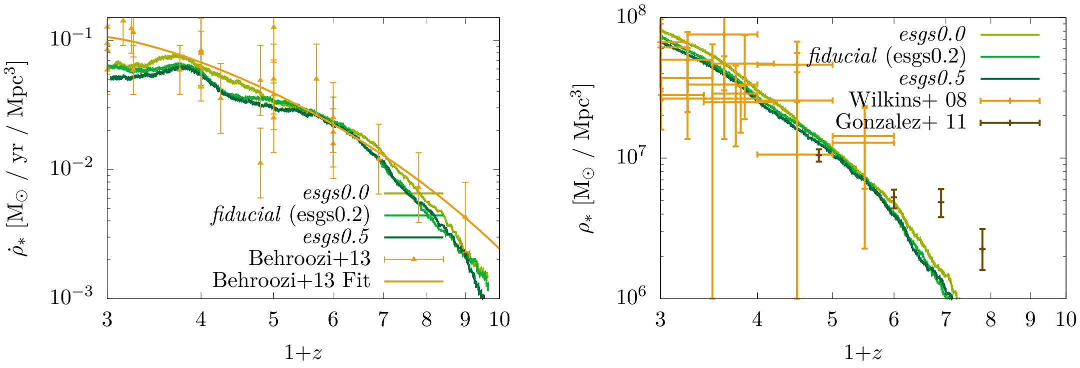

(a) Global star formation rate

(b) Global stellar density

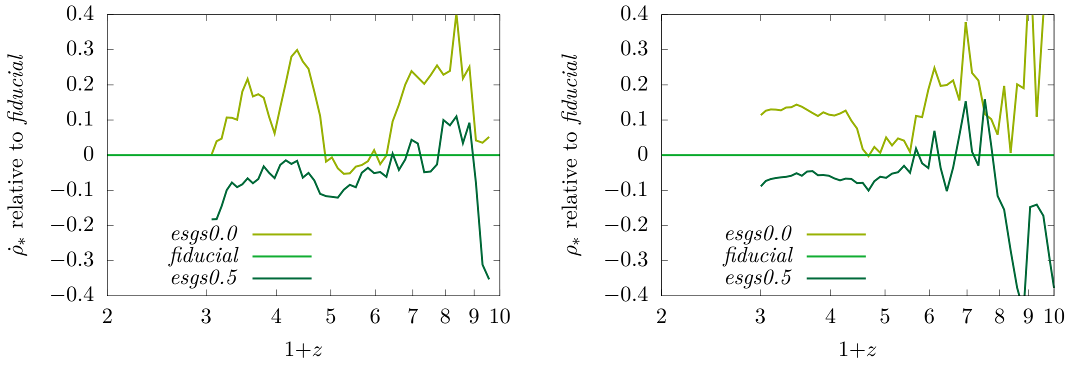

(c) Star formation rate relative to *fiducial*

(d) Stellar density relative to *fiducial*

Figure 5.27: Stellar history when varying the fraction of feedback that is used for explicit turbulent feedback ϵ_{SGS}.

5.3.3 Turbulent feedback

In section 4.5 we gave a motivation for explicit turbulent stellar feedback. We expect turbulent feedback to suppress star formation because the turbulent subgrid energy does not cool, and we therefore suspect the gas to stay hotter for longer times. This effect and turbulent pressure are assumed to help in pushing feedback out of the galaxy. In this section, we analyse its influence. For this, we have done three simulations: one in which we switched explicit turbulent feedback off, one with the fiducial choice of $\epsilon_{\mathrm{SGS}} = 0.2$, and one with a high amount of turbulent feedback, i.e. $\epsilon_{\mathrm{SGS}} = 0.5$.

Figure 5.27 compares the stellar histories of these three simulations. In general, star formation is more efficient without stellar feedback and is less efficient for higher ϵ_{SGS}. Additionally, the star formation rate is more variable without turbulent feedback. At $z = 2$, the simulation without turbulent feedback produced about 15 % more stars than the fiducial one, while the additional turbulent feedback in the *esgs0.5* simulation only lead to a decrease of less than 10 % in stellar

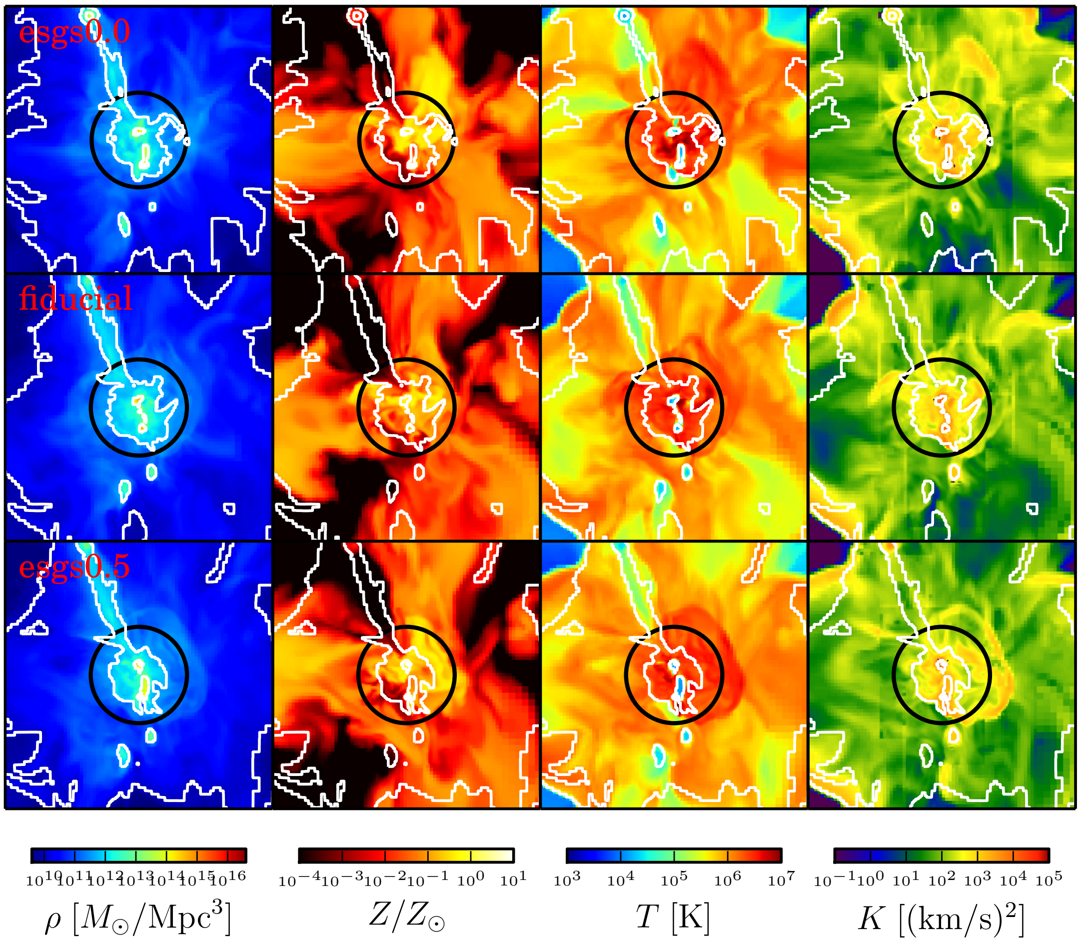

Figure 5.28: Comparison of slices with a width of 2 Mpc of halo 0 when varying the fraction of feedback energy used for turbulent feedback. This figure is of the same type as figure 5.4.

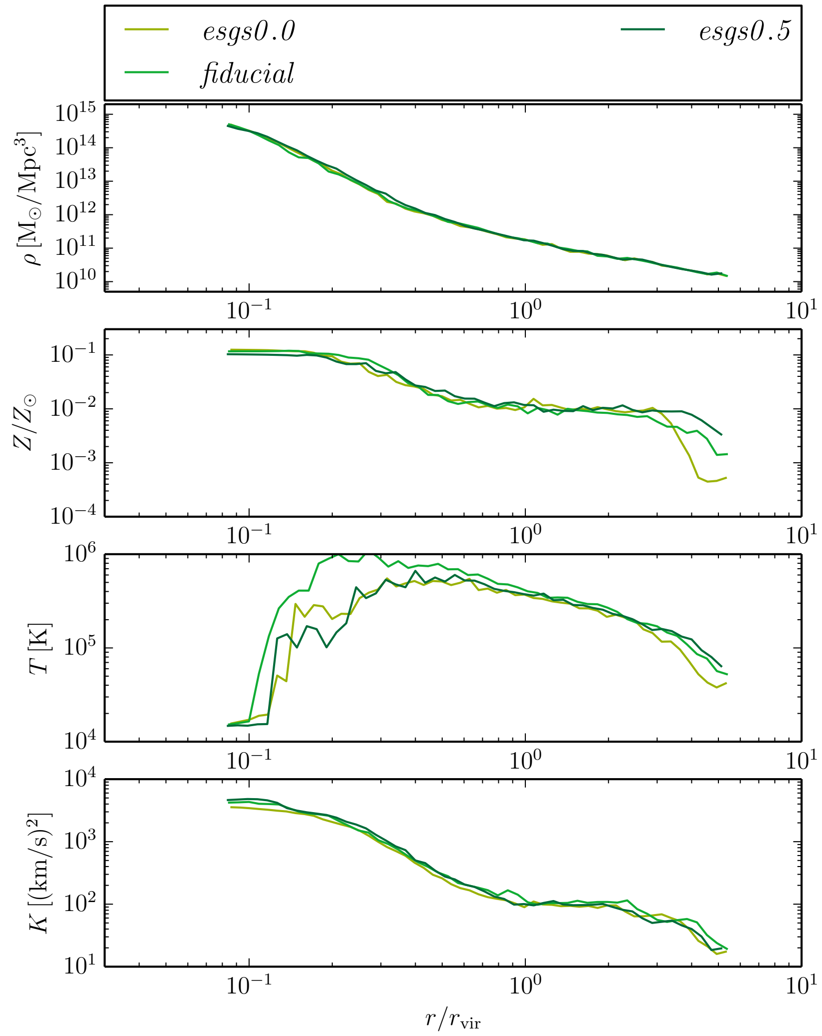

Figure 5.29: Stacked profiles for haloes with masses larger than 10^{11} M$_\odot$.

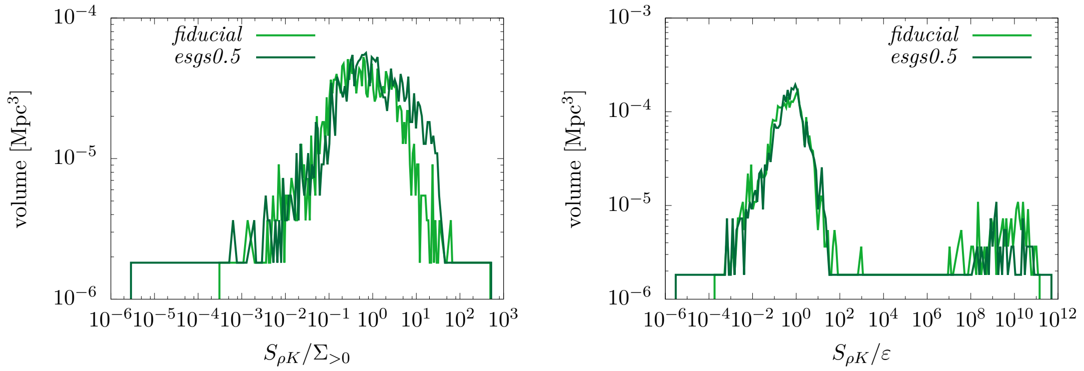

(a) PDF of the ratio between turbulent feedback and production by the turbulent cascasde.

(b) PDF of the ratio between turbulent feedback and dissipation of turbulent subgrid energy into heat.

Figure 5.30: PDFs of ratios between turbulent feedback and turbulent production/dissipation at $z = 2$ for both simulations in which we employ turbulent feedback.

mass. This indicates that turbulent feedback may saturate at some point.

Slices through the most massive halo in all three simulations are shown in figure 5.28. The slices are remarkably similar although minor differences can be seen. These differences are not necessarily due to the difference in turbulent stellar feedback but mainly due to the randomness of feedback and the chaotic nature of fluid instabilities.

Turning to stacked profiles of all haloes with more than 10^{11} $\mathrm{M}_\odot$ in figure 5.29, we again find no significant difference. Temperatures differ in the inner region due to the well known effects, and metallicities differ in the very outer regions. Most prominently, the turbulent subgrid energies in the central region are similar in all cases, and the simulation without turbulent feedback shows values only 25 % less than the ones with. This already shows that turbulent feedback is not the dominant turbulent process.

To quantify this finding, we plot probability distribution functions (PDF) in figure 5.30. These PDFs compare the relative importance of turbulent feedback to the key components of the turbulent subgrid model. Figure 5.30a shows a PDF of the ratio of turbulent feedback to turbulent production from the flow according to the SGS model, as explained in section 2.5. This distribution has its maximum at unity for both simulations containing turbulent feedback; it drops off significantly at 10 for the *fiducial* simulation and at 30 for *esgs0.5*. This clearly shows that turbulent feedback is not outweighing the turbulent production by much. Stirring the fluid via feedback inherently leads to an increase in turbulent production, independent of whether we employ explicit turbulent feedback or not. The statistics inferred from our simulations indicate that the stirring of halo gas dominates feedback. This might be biased, however, by insufficient resolution of both non-linear turbulent interactions and star formation activity.

The PDF of the ratio between turbulent feedback and dissipation of turbulent energy into heat in figure 5.30b shows a similar behaviour, its maximum is at one. This is due to the fact that the dissipation rate increases with turbulent energy. Additionally, we find a few cells with very high ratios. In these cells, we can see an artifact of the numerical implementation. The turbulent feedback is added after the dissipation has been calculated. According to this PDF, turbulent feedback energy is a transient contribution to the subgrid energy reservoir and is dissipated to heat rather fast. Therefore, it can not exert a significant turbulent pressure onto the surrounding gas. Speaking broadly, this is a turbulent overcooling problem. The root cause for this problem is that the turbulent subgrid model was developed assuming stationary, homogenous, and isotropic turbulence, without injection of large amounts of turbulent energy on small scales. For efficient turbulent feedback, a mechanism that slows down the increase of dissipation to heat is needed. This leads to higher turbulent energies for a longer period of time. Since this requires changes in the very basic assumptions of the turbulent subgrid model, this problem can be fixed only by developing a new kind of turbulent subgrid model.

Finally, we remark that other diagnostics like density or temperature PDFs do not differ while the content of gas in the various phases shows the expected behaviour (more effective feedback in simulations with more turbulent feedback), albeit with small differences.

In this section, we found that explicit turbulent feedback does not have a strong influence, since the stirring due to gas accretion, mergers, and feedback-driven outflows produces turbulence on numerically resolved scales, which is the dominant production mechanism.

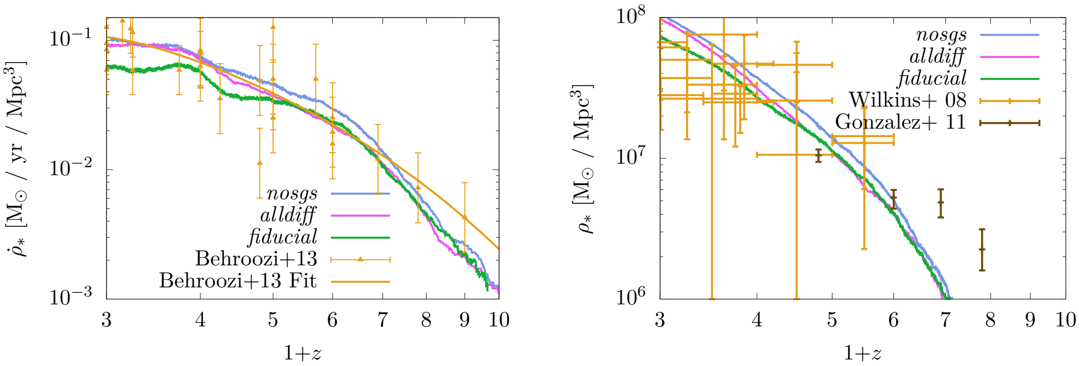

(a) Global star formation rate

(b) Global stellar density

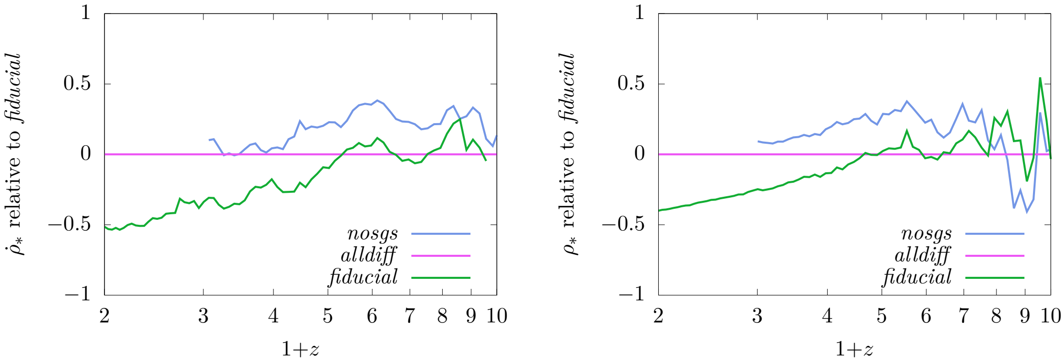

(c) Star formation rate relative to *alldiff*

(d) Stellar density relative to *alldiff*

Figure 5.31: Stellar history for simulations with (*alldiff* and *fiducial*) and without (*nosgs*) the turbulent subgrid model.

5.3.4 Turbulent subgrid model

Next, we compare our previous results to a simulation without the turbulent subgrid (SGS) model, entitled *nosgs*. Inherently, turbulent diffusion and turbulent feedback are disabled. As a consequence, the *nogsg* simulation and the (reduced) feedback model are comparable to typical simulations in the literature. We compare the *nosgs* simulation with the *fiducial* simulation and with the *alldiff* simulation. We do not compare to *esgs0.0*, which is, due to the absence of turbulent feedback, closer to *nosgs* than *fiducial* since we found in section 5.3.4 that turbulent feedback induces fairly small changes.

The stellar histories of the simulations in question are shown in figure 5.31. The *nosgs* simulation produces more stars than simulations with the SGS model before a redshift of $z \approx 3$. Afterwards, the star formation rates are nearly identical to the one of the *alldiff* simulation. Consequently, the stellar density adapts to the one observed in the *alldiff* simulation. The *fiducial* simulation significantly differs from the *nosgs* one at all times.

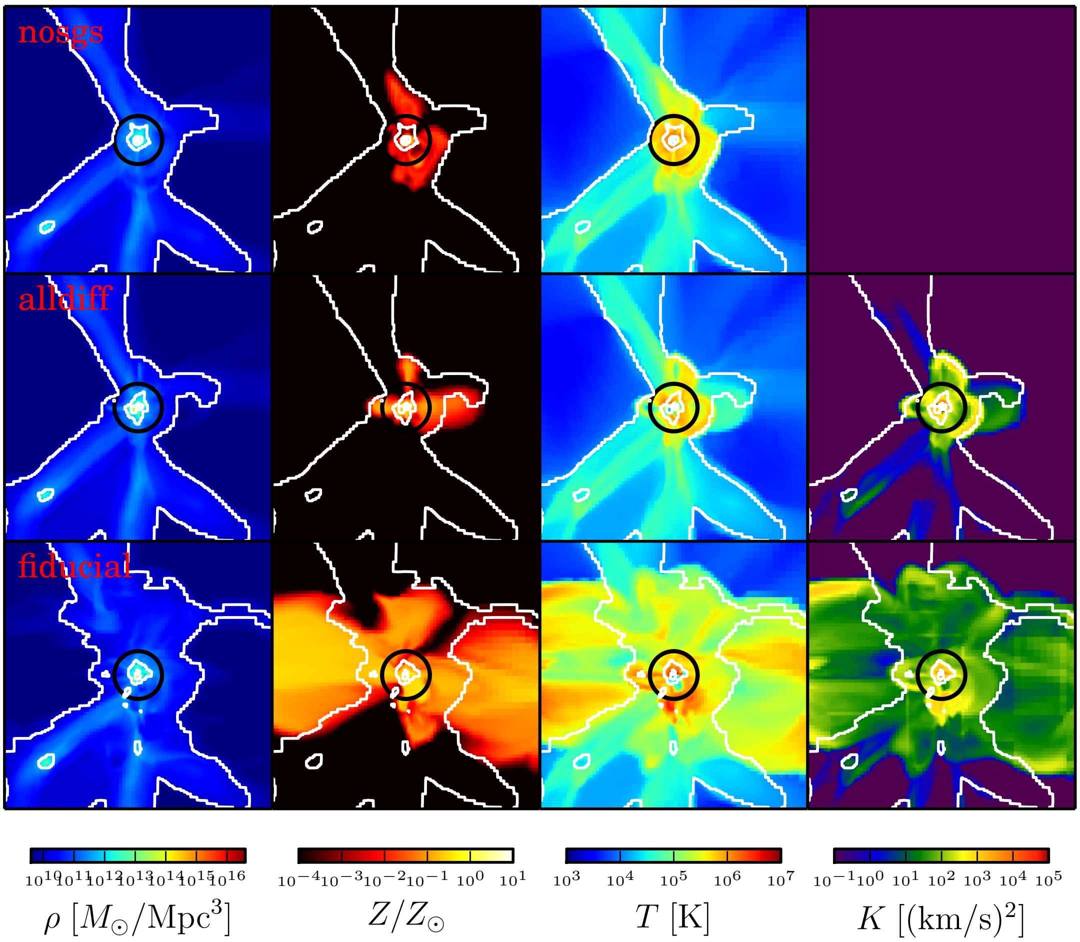

Figure 5.32: Slices of halo 4. Each panel has a width of 2 Mpc. The figure is of the same type as figure 5.4.

Figure 5.32 shows slices of halo 4 at $z = 2$. As indicated by the stellar history, *nosgs* and *alldiff* resemble each other and, as a result, *nosgs* and *fiducial* differ significantly. Zooming in on halo 1 in figure 5.33, we see that the simulations using the SGS model exhibit larger cold regions in the center than the *nosgs* simulation. This feature can also be found in other haloes. The other quantities do not differ significantly between *nosgs* and *alldiff* although *nosgs* exhibits a metal-rich blob in the upper right quarter of the panel, which is not present in the slice of the *alldiff* simulation.

To help quantifying the differences, we plot stacked profiles at $z = 2$ in figure 5.34 and at $z = 4$ in figure 5.35. The former exhibits large differences in the metallicity distribution between all three simulations. While the *fiducial* and the *alldiff* simulation show the behaviour discussed in section 5.3.1, the metallicity profile of the *nosgs* simulation decreases earlier than the profiles of the simulations with the SGS model. Further out, it features a small plateau, which is somewhat similar to the *fiducial* simulation, though showing lower metallicities and less uniformity. Looking at stacked profiles of the highest mass bin ($M_{\text{halo}} > 10^{11}\ \text{M}_{\odot}$) at $z \leq 5$ especially in figure 5.35, we consistently find that the *nosgs* simulations enrich farther out than the *alldiff* simulations. Nonetheless, they only reach approximately half the metallicity of the *fiducial* simulation at the virial radius: This indicates that feedback is more efficient in enriching the surroundings of a halo when switching the SGS model off than in the simulation with the SGS model and turbulent internal energy diffusion. Nevertheless, the simulations without turbulent internal energy diffusion, but with the SGS model, are even more effective.

In any case, the temperature profiles do not reflect the cold areas found in the slices due to the well known averaging problem. Looking at larger radii, they show a similar behaviour for *alldiff* and *nosgs* at $z = 2$. This is not the case at higher redshifts, for which temperatures are comparable between *nosgs* and *fiducial* but with lower maximal temperatures and an earlier drop-off. Especially the stacked temperature profile at $z = 4$ in figure 5.35 is an impressive example.
For haloes with masses between $10^{10}\ \text{M}_{\odot}$ and $10^{11}\ \text{M}_{\odot}$, we only find significant differences in the metallicity profiles, and these are only present at $z = 2$. *fiducial* and *nosgs* show the same behaviour with a slow decrease while *alldiff* rapidly drops-off around the virial radius.

We conclude that turbulent internal energy diffusion weakens the efficiency of feedback even beyond vanilla-type simulations without the SGS model. On the contrary, in simulations without TIED, turbulent effects[2] lead to a strong enhancement of the efficiency of feedback. These effects are also present in the simulations with TIED but are overcompensated by the enhanced cooling efficiency.

Having discussed the halo properties and the effectiveness of feedback, we go back to a more global diagnostic: the mass fractions, which are shown in figure 5.36.

---

[2] e.g. turbulent pressure and the existence of the turbulent subgrid energy as an energy reservoir that does not cool

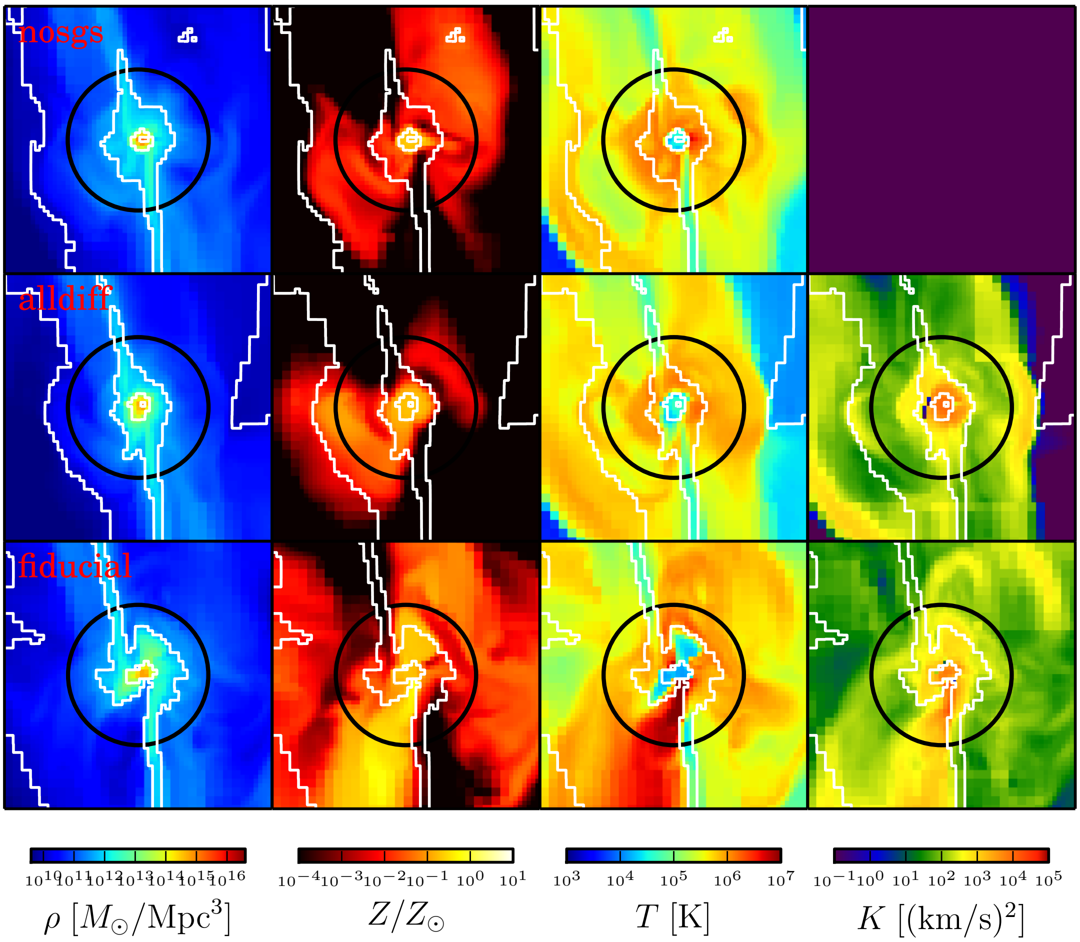

Figure 5.33: Zoom onto halo 1 using slices with a side length of 0.75 Mpc and showing simulations with and without the turbulent subgrid model. Otherwise, the plot is identical to figure 5.4.

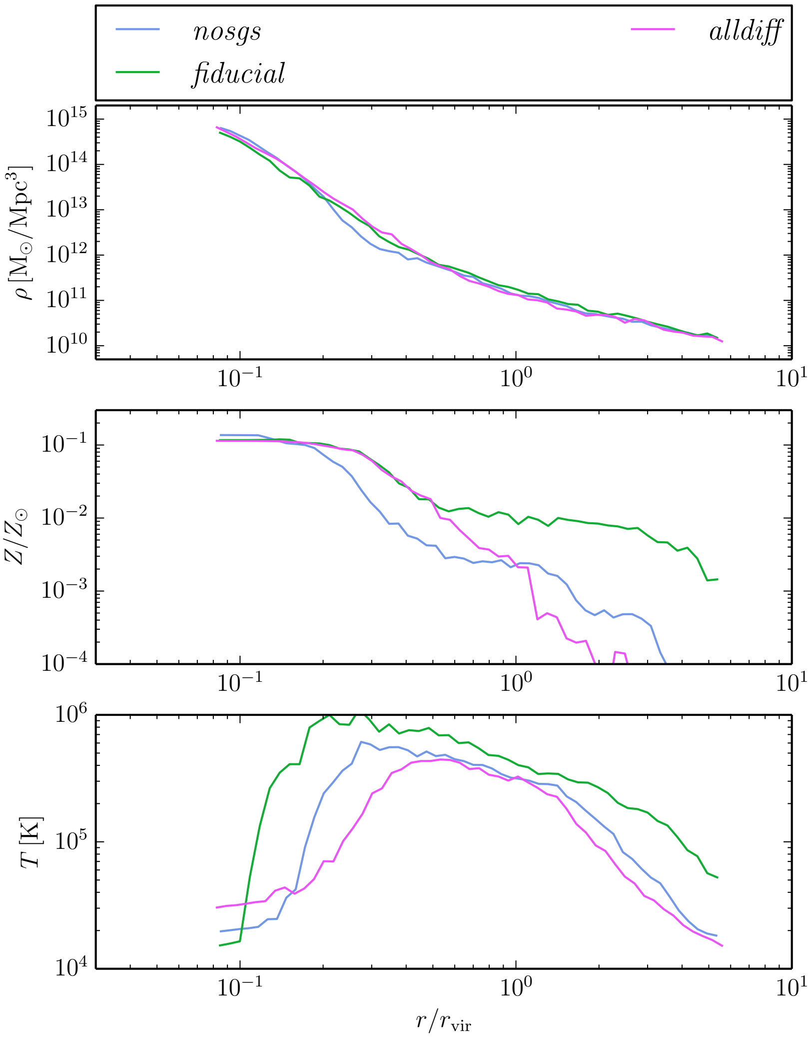

Figure 5.34: Stacked profiles for haloes with masses above 10^{11} $\mathrm{M}_\odot$ at $z = 2$.

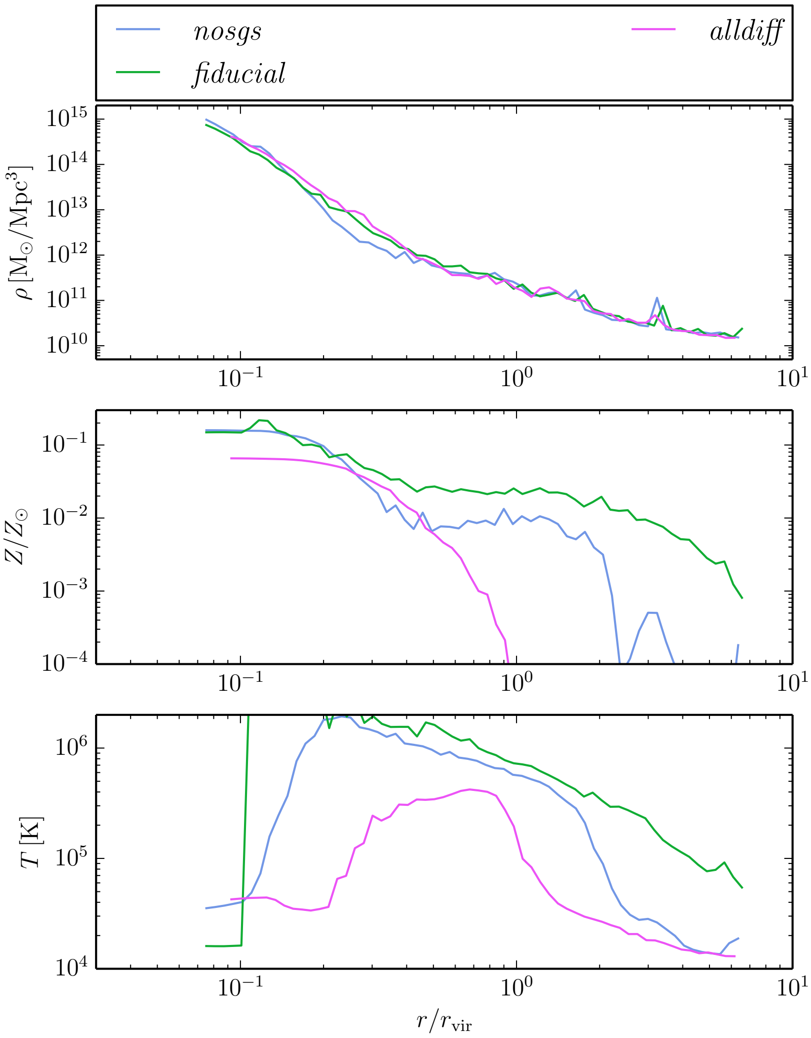

Figure 5.35: As figure 5.34 but at redshift $z = 4$.

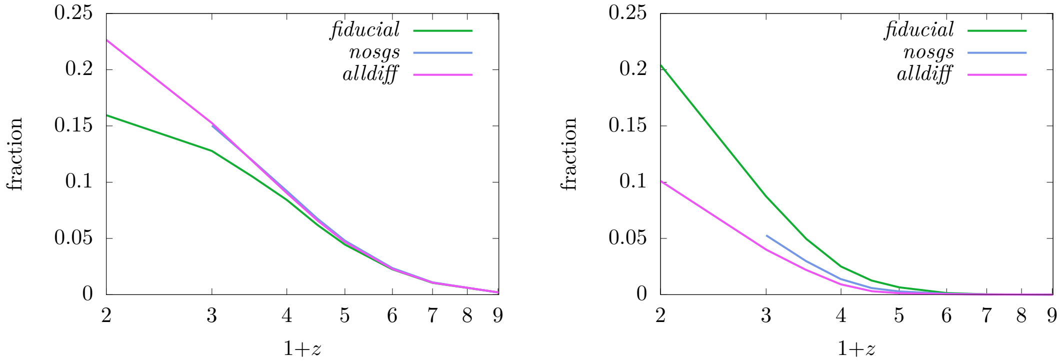

(a) Condensed phase

(b) WHIM phase

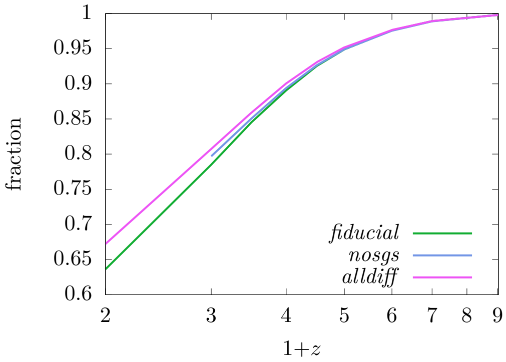

(c) Warm phase

Figure 5.36: Evolution of the global fractions of gas phases (see table 5.2) as a function of redshift. We omit the hot fraction since it is too noisy.

The condensed fraction is nearly identical for *nosgs* and *alldiff*. In contrast, a large difference is found between these two and the *fiducial* simulation. Since the condensed fraction is the reservoir from which stars are formed, the reduction of the star formation rates in *fiducial* is due to the turbulent effects reducing the gas available for star formation. This is to be expected, since our model of star formation as described in section 4.2 contains a constant efficiency.

In the *nosgs* simulation, the WHIM is slightly more populated compared to the *alldiff* simulation. This is consistent with our results above, where we found that *nosgs* shows a more efficient feedback than *alldiff*. Concerning the warm phase, we refer to the explanation in section 5.3.1, in which we found that the warm gas missing in the *fiducial* simulation is in fact heated by feedback and thereby shifted to the WHIM phase. This is consistent with our findings for the WHIM phase.

The comparison done in this chapter shows that the turbulent subgrid model has a strong influence on star formation as well as on stellar feedback: It suppresses star formation, helps in preventing overcooling, and strongly increases the efficiency of feedback. However, the large enhancement in the cooling efficiency due to turbulent internal energy diffusion (over-)compensates most of the turbulent effects and may lead to the wrong impression that the turbulent subgrid model is not important. Most observables are similar in *nosgs* and *alldiff*, which is probably due to the fact that in both cases star formation is mostly limited by accretion and not by efficient feedback.

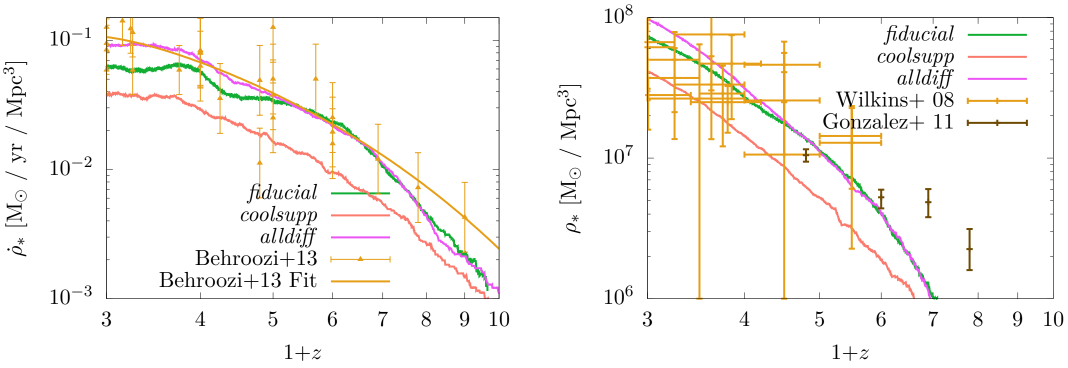

(a) Global star formation rate

(b) Global stellar density

Figure 5.37: Stellar history upon varying cooling suppression. Since the *coolSupp* simulation has turbulent diffusion of metals and internal energy enabled, we also compare with the *alldiff* simulation, as these two only differ by the additional cooling suppression.

5.3.5 Cooling suppression

In the literature, the application of cooling suppression is often motivated by its proposed ability to mimic turbulence which we discussed in section 4.4.2. In this section, we analyse the *coolsupp* simulation, which shares the configuration with the *alldiff* simulation but with additional cooling suppression. Additionally, we show the *fiducial* simulation in some plots, which is our favoured model and exhibits the full set of turbulent effects.

In figure 5.37, the stellar history is shown. The suppression of star formation due to cooling suppression is striking in both the star formation rate and stellar density. It increases with time and is the process with the strongest influence on star formation of all processes considered in this work.

The stellar mass-halo mass relations in figure 5.38 differ significantly. For the *coolsupp* simulation, it is lower everywhere, but the difference grows for larger halo masses. This is explained by the fact that massive objects form at later times which leads to the suppression of star formation is stronger at later times. Figure 5.38 may mislead to the false impression that a simulation with cooling suppression performs better in reproducing the observations of the stellar mass-halo mass relation. This impression is inaccurate for the following two reasons: Firstly, this simulation's global stellar density is far off from the observed values and a recalibrated run would shift the stellar mass-halo mass relation upwards. Secondly, the general slope and especially the strong flattening above $2 \cdot 10^{11}$ M$_\odot$ are not found in the observations.

Figure 5.39a shows density PDFs. While the simulations without cooling suppression agree, the *coolsupp* simulation contains significantly less gas at high den-

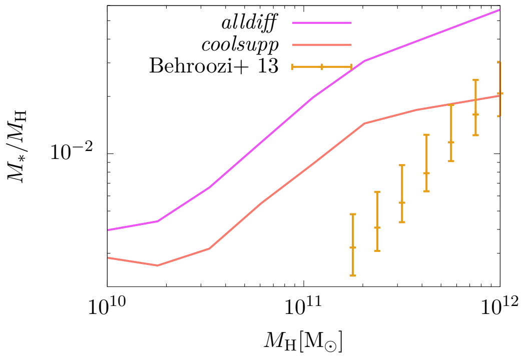

Figure 5.38: Stellar mass-halo mass relation for two simulations, one with and one without cooling suppression at $z = 2$.

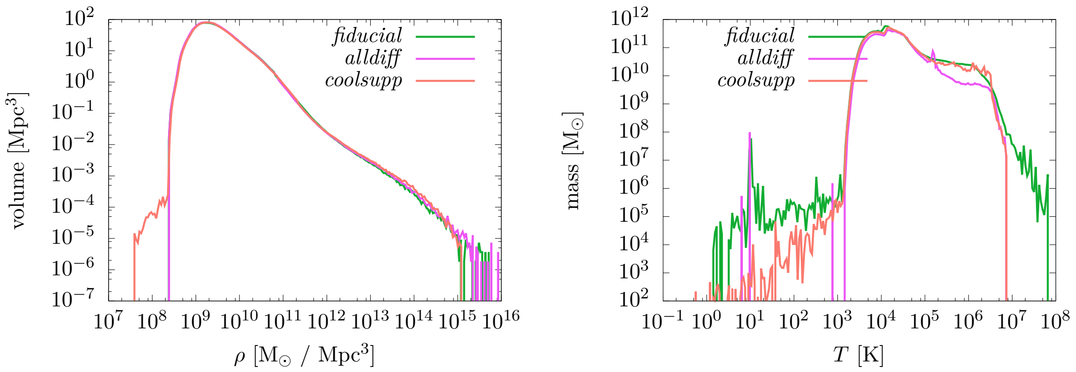

(a) PDF of the density

(b) PDF of the temperature

Figure 5.39: PDFs of the density and temperature at $z = 2$. Beware that the temperature PDF is with respect to mass.

sities. Differences can be seen in the density maximum, which is one order of magnitude lower for *coolsupp*, as well as in the density minimum, which is nearly one order of magnitude lower in the *coolsupp* simulation. Since the star formation rate is dominated by density, the difference in the maximum of the density PDF explains the suppression of star formation.

The temperature PDF in figure 5.39b shows that the *coolsupp* simulation contains more gas at high temperatures than the *alldiff* simulation. Nevertheless, both simulations share the rather low maximal temperature, which is exceeded by the *fiducial* simulation by one order of magnitude. The excess of hot gas compared to *alldiff* is the reason for the smaller densities seen in the density PDF because higher temperatures lead to higher thermal pressure and thereby reduce the efficiency of accretion. The similarity of *coolsupp* and *fiducial* in the temperature PDF between 10^5 K and $3 \cdot 10^6$ K is mere coincidence. Below 10^3 K, the *coolsupp* simulation contains significantly more gas than the *alldiff* simulation. This result is unexpected as both simulations share the same physics for areas outside the regions in which feedback happens. Therefore, turbulent diffusion of internal energy should move the cold gas to the cooling equilibrium, as argued above.

Figure 5.40 shows slices of the *coolsupp* and the *alldiff* simulation. When looking at the density contours belonging to lower densities, we find that both simulations agree very well. In the inner part, in contrast, density is significantly lower, but the high density region is larger for the *coolsupp* simulation. The metallicity distribution in the *coolsupp* simulation looks slightly smoother, while the metallicity is significantly lower. This disparity is due to the strong suppression of star formation. The temperature in the *coolsupp* simulation differs from any other simulation: It contains a hot core – whereas all other simulations contain a cold one. This hot core is smaller than the high density region, and surrounded by a cold sphere. This hot core is the direct effect of cooling suppression. The turbulent subgrid energy deviates as well. It is lower and spread out farther.

The profiles of halo 0, shown in figure 5.41, reproduce most of the findings from the slices in a more quantitative way. The density profile is lower in the center, and flatter and higher in the outer parts. Metallicity is lower but otherwise resembling behaviour of the *alldiff* simulation, which declines fast compared to the *alldiff* simulation. Ignoring once again the inner part of the temperature profile, the part beyond the virial radius is closely following the *alldiff* simulation. The profile of the turbulent internal energy is constant in the inner part and resembles, consequently, the *alldiff* one. The constancy of turbulent subgrid energy in the center of the halo and its low value indicate that the center of the halo is in hydrostatic equilibrium without large disturbances. Apart from this, the profile of the stellar density is very interesting: Compared to the *fiducial* and *alldiff* simulations, the *coolsupp* simulation produces fewer stars by more than two order of magnitude. And, in contrast to any other simulation, the stellar density slightly increases when going outwards, corresponding to the cold sphere seen in the slices. Thus, is seems that stars are formed in a region which is larger by a factor of up to two. This can also be seen when comparing the regions with active feedback.

The stacked profiles in figure 5.42 confirm the results we found in the slices and in the haloes. The difference in densities is smaller, but still significantly distinct compared to the difference between the *alldiff* and the *fiducial* simulation. The inner temperature profile of the *coolsupp* simulation, although to be taken with caution due to the problems described above, is similar to the behaviour we found in the slices. The inner part is hot; then, going outwards, there is a cold sphere, and farther out they show the properties of the *alldiff* simulation. We point out that the profiles should be reliable since the slices show a rather smooth and radially symmetric characteristic.

Summarizing, we find that cooling suppression helps in reducing star formation by heating up the central parts of a halo, but it does not incur the turbulent effects we find in the *fiducial* simulation. Therefore, cooling suppression is not a good replacement for an explicit treatment of turbulence.

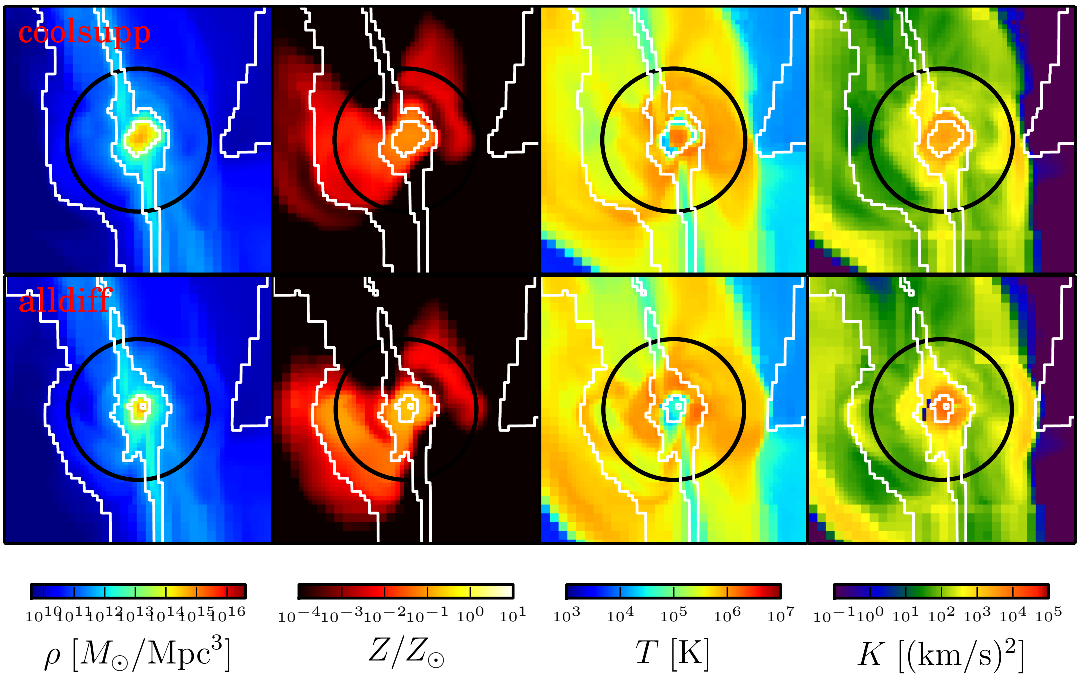

Figure 5.40: Slices of halo 1. Each panel has a width of 0.75 Mpc.

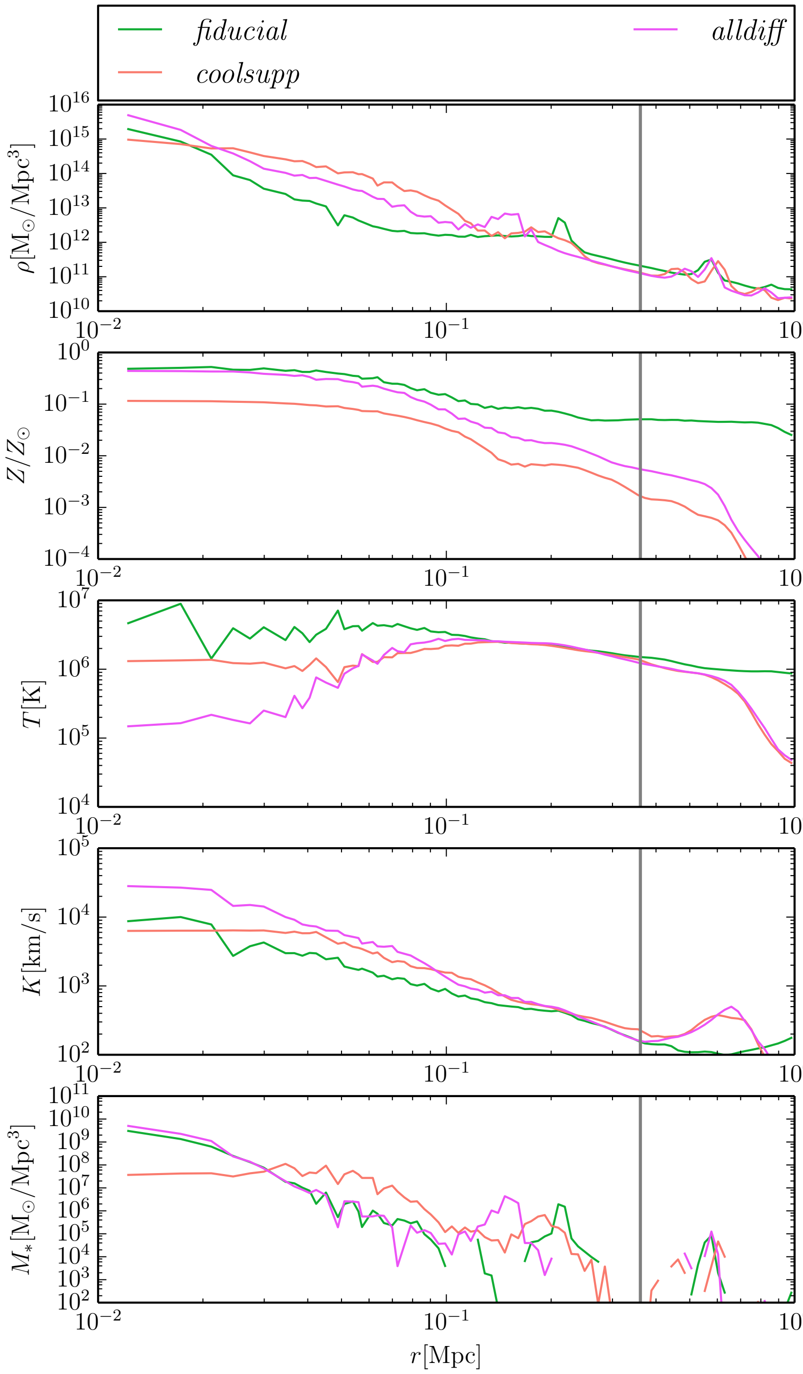

Figure 5.41: Profiles of halo 0 at redshift $z = 2$.

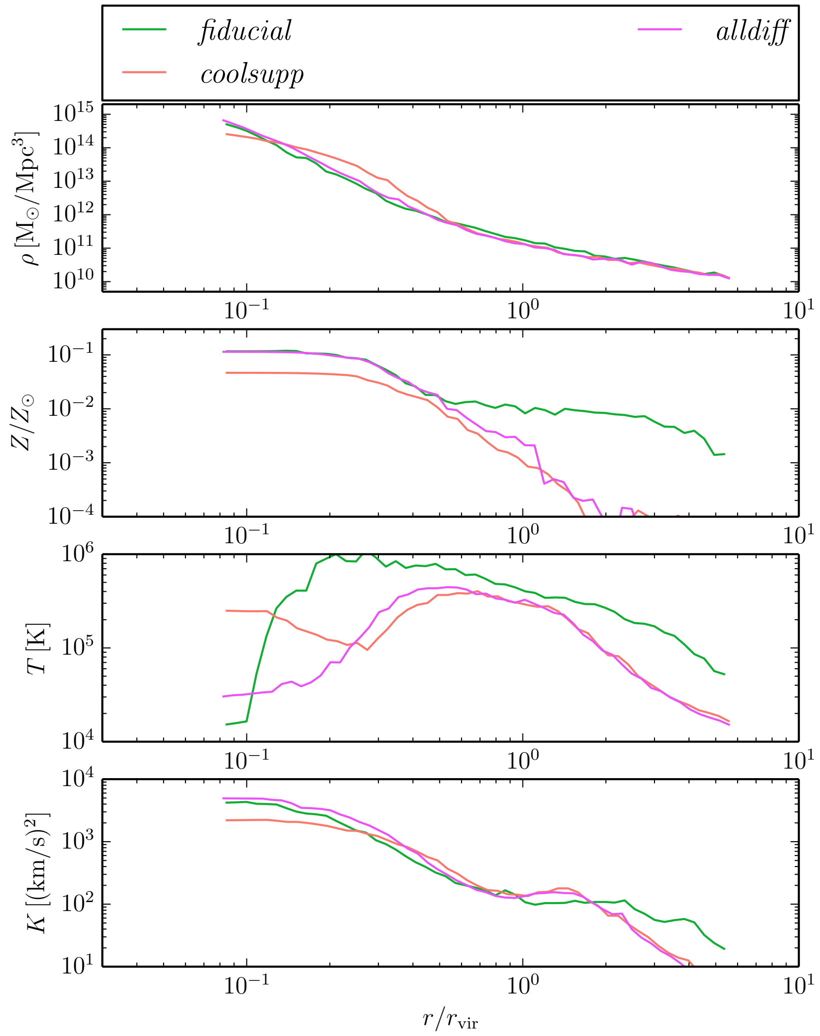

Figure 5.42: Stacked profiles for haloes with masses larger than 10^{11} $\mathrm{M}_\odot$.

6 Conclusion

In this work, a state of the art-model for star formation and stellar feedback has been developed, verified, and used in cosmological simulations. Alongside, numerical and physical models had to be implemented and refined. This includes cosmological initial conditions, (metal) cooling, star particles, and various analysis techniques.

The star formation model used in this work employs a Kennicutt-Schmidt law [41, 86] with a constant star formation efficiency and a density exponent of 3/2. It is sampled stochastically under the assumption of Poisson distributed star formation events. Star formation is allowed in cells which reach a certain density and reside on the finest level in the simulation. We found that most additional star formation criteria, apart from the Jeans criterion, have a negligible influence. Our stellar feedback model derives the temporal distribution of feedback from stellar lifetimes. We consider metal enrichment by stellar winds of AGB stars and by supernovae but assume supernovae to be the only mechanism transporting metals outwards. For feedback energy, we assume the canonical 10^{51} erg per supernova. Additionally, our model is able to inject an adjustable fraction of feedback energy directly into the turbulent kinetic subgrid energy and to explicitely model turbulent diffusion of species as well as internal energy. Compared to other models, turbulent feedback based on the LES approach is a unique feature, although turbulent diffusion in a very simplified implementation is used in a few publications ([104, 115]). Our approach for modeling star formation and stellar feedback is comparable to the methods used in most simulations in the literature which aim at similar resolutions (e.g. [71, 99]). In contrast, simulations of isolated disk galaxies like the ones by [8], focussing on much higher resolutions, use a more detailed description of the multiphase interstellar medium, form stars only from molecular hydrogen, and employ a variable star formation efficiency. In our simulations, we do not resolve star formation regions at all, so the processes leading to different phases are not numerically accessible. Coarse-graining a simulated galaxy by [8] to resolutions used in this work shows that their star formation model is well approximated by our approach.

We tested our model thoroughly and found that it reproduces the observed evolution of star formation (see chapter five). Specifically, we are able to reproduce the star formation rate or stellar density up to $z = 1$. We can not reproduce both star formation rate and stellar density at the same time since the observations are not fully consistent. Additionally, star formation at late times is significantly reduced by the outflows of active galactic nuclei ([84, 111]). Since our model does not include active galactic nuclei, we only find a minor decline in star formation rates below a redshift of two, where the observations show a strong decline.

In the stellar mass function and in the stellar mass-halo mass relation, our model shows certain problems in reproducing the observational data. In contrast, the halo mass function is reproduced very well but drops off at low halo masses. This makes it difficult to fit both the global quantities, such as star formation rate and stellar mass density, and the local ones, e.g. the stellar mass function and the stellar mass-halo mass relation. This result is also supported by our tests employing different cosmological initial conditions, which suggest that the star formation rate strongly depends on the number of very massive haloes, while the stellar mass-halo mass relation is robust under changing the initial conditions. The phase diagram with respect to temperature and overdensity shows the expected behaviour.

Moving to ever smaller scales and comparing individual but massive haloes, we find that their surroundings differ significantly, which is apparent in slices and profiles of the haloes. Applying two criteria for the CGM (by [34] and [72]), we find them disagreeing in haloes with significant outflows but agree in the quiescent ones. Analyzing stacked profiles grouped into mass bins, we find that density and turbulent subgrid energy agree over the mass bins considered while temperature and metallicity are higher with higher halo mass. Since higher mass haloes form more stars both is to be expected. Additionally, the metallicity distribution is flatter for higher mass haloes. This means that there are more metals on the outskirts of more massive haloes, which therefore enrich their surroundings more efficiently. We also find that an approximation to baryonic density in the CGM by Pallottini et al. [72], which only depends on the radius scaled by the virial radius, fits our data well although there are significant deviations in the centers of the haloes.

Studying the influence of the turbulence subgrid model, we find that it increases the efficiency of feedback and reduces the star formation rates significantly. Hence, the gas available for star formation is reduced. Galactic outflows, consequently, are much stronger and spread to larger radii. One example is a metallicity of $Z = 0.01Z_\odot$, which is sustained for approximately three virial radii at $z = 2$ for haloes with $M > 10^{11}\ \mathrm{M}_\odot$ in a simulation with the SGS model turned on. In a simulation without SGS model, in contrast, metallicity drops below $Z = 0.01Z_\odot$ at 0.2 virial radii. This shows that turbulent pressure can reduce gravitational collapse and that turbulent dissipation can solve the overcooling problem by keeping the feedback hot and counteracting cooling. We find that this effect, similar to most effects discussed in this work, is stronger for more massive haloes. This is due to the fact that only massive haloes can maintain a sufficient level of turbulence.

A contrary effect results from turbulent diffusion of internal energy (TIED), which leads to significantly increased star formation rates and to significantly weaker feedback, up to the point where the simulation becomes similar to one without the subgrid turbulence model. The magnitude of this effect was not expected. It results from the fact that cooling rates are highly nonlinear. Hot gas has a considerably longer cooling timescale than warm gas. If TIED distributes feedback energy over a larger number of cells, the resulting temperature is reduced and cooling becomes, thus, more efficient. This effect is especially strong around temperatures of 10^6 K, for which the PDF shows one order of magnitude less gas in the simulations with TIED compared to the one without. Hence, TIED leads to overcooling. When comparing simulations with and without TIED, we find that the star formation rates at $z = 1$ differ by a factor of two while the corresponding stellar densities differ by a factor of 1.5.

Severe changes can also be seen in the structure of the CGM in simulations with TIED. Baryonic density is not affected strongly, but metallicity and temperature extend to much smaller radii. In stacked profiles, for example, a metallicity of $0.01\ \mathrm{Z}_\odot$ is sustained up to three times the virial radius in simulations without TIED while in simulations with TIED the metallicity drops below $0.01\ \mathrm{Z}_\odot$ around 0.5 times the virial radius. A similar behaviour is seen in turbulent energy, leading to the conclusion that the accretion shocks are located at least three times farther out in simulations without TIED. In most aspects, the simulations with TIED resemble the ones without the turbulent subgrid model, but the latter produce more efficient feedback. The efficiency of feedback in simulations without TIED can also be seen by the fact that the warm-hot intergalactic medium (WHIM) is populated by as much as 20 % of the baryons and the condensed medium by only 15 %, compared to 10 % and 22 %, respectively, in the simulations with TIED at $z = 1$. For the fraction of metals, this diagnostic is even more significant: The simulation without TIED expels one fourth of the metals into the WHIM while the simulation with TIED only around 3 %. To the best of our knowledge, these effects have not been studied before. In our favourite model, we neglect TIED due to the strong disadvantageous effects it shows. We argue that TIED is artificially strong since it neglects the multiphase structure of the medium on subgrid scales.

We conclude that using a turbulent subgrid model without turbulent internal energy diffusion is viable and a physically well-motivated way to solve the overcooling problem as well as to obtain efficient feedback, without introducing complicated feedback schemes.

We also studied the influence of turbulent diffusion of species (TDS) and found it to be rather weak. As expected, the smoother distribution of metals leads to more star formation, by enabling more gas to cool below 10^4 K. Nonetheless, this effect increases star formation only by about 10 % at $z = 2$. This result has also been found by [104] using a simple shear-based estimator for turbulence.

When looking at the metallicity distribution around haloes, we find that it is dominated by the effects of TIED. Only if outflows are weakened by switching on TIED, TDS is able to transport metals outward in some haloes. This effect is showing up only weakly in stacked profiles. One would expect that TDS is able to transport metals outward along the metallicity gradient. This is not the case since, firstly, accretion flows are moving gas in the opposite direction and, secondly, in simulations without TIED, feedback transports metals already to large radii.

An appealing idea in the context of our model is explicit turbulent feedback: A fraction of feedback energy is directly fed into the turbulent subgrid energy rather than into the thermal energy. The underlying hypothesis is that the additional turbulent subgrid energy enhances feedback efficiency by increasing turbulent pressure and by sustaining a higher temperature due to a delayed release of feedback energy into the internal energy via turbulent dissipation.

We varied the fraction of turbulent feedback and found that feeding 50 % of feedback energy into the turbulent subgrid energy reduces stellar density by about 25 % at $z = 2$. Morphology and profiles of haloes are largely unaffected by this. The reason is that turbulent feedback is not the dominant production process of turbulent energy. Even when taking only cells with active feedback into account, turbulent production from resolved flows and turbulent feedback are equal on average. Additionally, we found that turbulent dissipation into heat adapts instantly to the increased turbulence level. This is due to the fact that the SGS model was developed for stationary, homogenous, and isotropic turbulence. In a future work, after developing a SGS model overcoming these limitations, one may reassess turbulent feedback. Similarly, [8] found that turbulent feedback does not have a strong influence for isolated disk galaxies as long as the star formation efficiency does not depend on turbulence.

In the literature, it is often claimed that turbulent effects can be mimiced via cooling suppression (see, e.g. [33, 115]). Cooling suppression means that cooling is switched off in cells in which feedback occurs. The idea is to sustain a high temperature so that gas can expand and launch feedback effectively. Thereby, it is meant to overcome the overcooling problem.

We implemented a cooling suppression scheme and applied it to find that cooling suppression is able to suppress star formation by a factor of three at $z = 3$. Additionally, it leads to a flat core and a very slow decrease of the radial density profile. Furthermore, stars are forming significantly farther out. Nevertheless, cooling suppression is not able to launch feedback efficiently. Compared to our preferred model, feedback is significantly weaker. Using a turbulent subgrid model without TIED instead of cooling suppression thus appears to be favorable.

Summarizing, this work shows that modeling unresolved turbulence can have a large impact on star formation rates and feedback efficiency. Furthermore, the introduction of the turbulent subgrid energy as an additional energy budget can help to overcome the overcooling problem. This is especially the case for simulations without turbulent internal energy diffusion, although this setup is physically not fully consistent.

Future work might explore the applicability of the model at even lower resolutions and possibly use it for example in simulations of the Lyman-α forest. In contrast, for a deeper understanding of the turbulent processes around galaxies higher resolutions are needed. A good approach would be zoom-in simulations but, as we found, these are not feasible with the current code.

Bibliography

[1] A. S. Almgren, J. B. Bell, M. J. Lijewski, Z. Lukić, and E. Van Andel. Nyx: A Massively Parallel AMR Code for Computational Cosmology. *ApJ*, 765: 39, March 2013. doi: 10.1088/0004-637X/765/1/39.

[2] Gene M. Amdahl. Validity of the single processor approach to achieving large scale computing capabilities. In *Proceedings of the April 18-20, 1967, Spring Joint Computer Conference*, AFIPS '67 (Spring), pages 483–485, New York, NY, USA, 1967. ACM. doi: 10.1145/1465482.1465560. URL `http://doi.acm.org/10.1145/1465482.1465560`.

[3] I. K. Baldry and K. Glazebrook. Constraints on a Universal Stellar Initial Mass Function from Ultraviolet to Near-Infrared Galaxy Luminosity Densities. *ApJ*, 593:258–271, August 2003. doi: 10.1086/376502.

[4] P. S. Behroozi, R. H. Wechsler, and C. Conroy. The Average Star Formation Histories of Galaxies in Dark Matter Halos from z = 0-8. *ApJ*, 770:57, June 2013. doi: 10.1088/0004-637X/770/1/57.

[5] Y. Birnboim and A. Dekel. Virial shocks in galactic haloes? *MNRAS*, 345: 349–364, October 2003. doi: 10.1046/j.1365-8711.2003.06955.x.

[6] H. Braun and W. Schmidt. A semi-analytic model of the turbulent multiphase interstellar medium. *MNRAS*, 421:1838–1860, April 2012. doi: 10.1111/j.1365-2966.2011.19889.x.

[7] H. Braun and W. Schmidt. The small and the beautiful: how the star formation law affects galactic disc structure. *MNRAS*, 454:1545–1555, December 2015. doi: 10.1093/mnras/stv1856.

[8] H. Braun, W. Schmidt, J. C. Niemeyer, and A. S. Almgren. Large-eddy simulations of isolated disc galaxies with thermal and turbulent feedback. *MNRAS*, 442:3407–3426, August 2014. doi: 10.1093/mnras/stu1119.

[9] N. G. Busca, T. Delubac, J. Rich, S. Bailey, A. Font-Ribera, D. Kirkby, J.-M. Le Goff, M. M. Pieri, A. Slosar, É. Aubourg, J. E. Bautista, D. Bizyaev, M. Blomqvist, A. S. Bolton, J. Bovy, H. Brewington, A. Borde, J. Brinkmann, B. Carithers, R. A. C. Croft, K. S. Dawson, G. Ebelke, D. J. Eisenstein, J.-C. Hamilton, S. Ho, D. W. Hogg, K. Honscheid, K.-G. Lee, B. Lundgren, E. Malanushenko, V. Malanushenko, D. Margala,

C. Maraston, K. Mehta, J. Miralda-Escudé, A. D. Myers, R. C. Nichol, P. Noterdaeme, M. D. Olmstead, D. Oravetz, N. Palanque-Delabrouille, K. Pan, I. Pâris, W. J. Percival, P. Petitjean, N. A. Roe, E. Rollinde, N. P. Ross, G. Rossi, D. J. Schlegel, D. P. Schneider, A. Shelden, E. S. Sheldon, A. Simmons, S. Snedden, J. L. Tinker, M. Viel, B. A. Weaver, D. H. Weinberg, M. White, C. Yèche, and D. G. York. Baryon acoustic oscillations in the Lyα forest of BOSS quasars. *A&A*, 552:A96, April 2013. doi: 10.1051/0004-6361/201220724.

[10] A. Cahuzac, J. Boudet, P. Borgnat, and E. Lévêque. Smoothing algorithms for mean-flow extraction in large-eddy simulation of complex turbulent flows. *Physics of Fluids*, 22(12):125104–125104, December 2010. doi: 10.1063/1.3490063.

[11] R. Cen and N. E. Chisari. Star Formation Feedback and Metal-enrichment History of the Intergalactic Medium. *ApJ*, 731:11, April 2011. doi: 10.1088/0004-637X/731/1/11.

[12] R. Cen and J. P. Ostriker. Galaxy formation and physical bias. *ApJ*, 399: L113–L116, November 1992. doi: 10.1086/186620.

[13] G. Chabrier. Galactic Stellar and Substellar Initial Mass Function. *PASP*, 115:763–795, July 2003. doi: 10.1086/376392.

[14] P. Colella. Multidimensional upwind methods for hyperbolic conservation laws. *Journal of Computational Physics*, 87:171–200, March 1990. doi: 10.1016/0021-9991(90)90233-Q.

[15] Luc Devroye. *Non-uniform random variate generation.* Springer, 1986.

[16] K. Dolag, F. Vazza, G. Brunetti, and G. Tormen. Turbulent gas motions in galaxy cluster simulations: the role of smoothed particle hydrodynamics viscosity. *MNRAS*, 364:753–772, December 2005. doi: 10.1111/j.1365-2966.2005.09630.x.

[17] Y. Dubois and R. Teyssier. On the onset of galactic winds in quiescent star forming galaxies. *A&A*, 477:79–94, January 2008. doi: 10.1051/0004-6361:20078326.

[18] D. J. Eisenstein and W. Hu. Power Spectra for Cold Dark Matter and Its Variants. *ApJ*, 511:5–15, January 1999. doi: 10.1086/306640.

[19] D. J. Eisenstein and P. Hut. HOP: A New Group-Finding Algorithm for N-Body Simulations. *ApJ*, 498:137–+, May 1998. doi: 10.1086/305535.

[20] J. F. Engels, W. Schmidt, and J. C. Niemeyer. Modelling turbulent effects of stellar feedback in cosmological simulations. *in preparation*, 2017.

[21] G. J. Ferland, K. T. Korista, D. A. Verner, J. W. Ferguson, J. B. Kingdon, and E. M. Verner. CLOUDY 90: Numerical Simulation of Plasmas and Their Spectra. *PASP*, 110:761–778, July 1998. doi: 10.1086/316190.

[22] G. J. Ferland, R. L. Porter, P. A. M. van Hoof, R. J. R. Williams, N. P. Abel, M. L. Lykins, G. Shaw, W. J. Henney, and P. C. Stancil. The 2013 Release of Cloudy. *Rev. Mexicana Astron. Astrofis.*, 49:137–163, April 2013.

[23] Drummond Fielding, Eliot Quataert, Michael McCourt, and Todd A. Thompson. The impact of star formation feedback on the circumgalactic medium. June 2016.

[24] J. A. Frieman, M. S. Turner, and D. Huterer. Dark energy and the accelerating universe. *ARA&A*, 46:385–432, September 2008. doi: 10.1146/annurev.astro.46.060407.145243.

[25] V. González, I. Labbé, R. J. Bouwens, G. Illingworth, M. Franx, and M. Kriek. Evolution of Galaxy Stellar Mass Functions, Mass Densities, and Mass-to-light Ratios from z ˜ 7 to z ˜ 4. *ApJ*, 735:L34, July 2011. doi: 10.1088/2041-8205/735/2/L34.

[26] F. Haardt and P. Madau. Modelling the UV/X-ray cosmic background with CUBA. In D. M. Neumann and J. T. V. Tran, editors, *Clusters of Galaxies and the High Redshift Universe Observed in X-rays*, 2001.

[27] F. Haardt and P. Madau. Radiative Transfer in a Clumpy Universe. IV. New Synthesis Models of the Cosmic UV/X-Ray Background. *ApJ*, 746:125, February 2012. doi: 10.1088/0004-637X/746/2/125.

[28] O. Hahn and T. Abel. Multi-scale initial conditions for cosmological simulations. *MNRAS*, 415:2101–2121, August 2011. doi: 10.1111/j.1365-2966.2011.18820.x.

[29] D. H. Hartmann. Afterglows From the Largest Explosions in the Universe. *Proceedings of the National Academy of Science*, 96:4752–4755, April 1999. doi: 10.1073/pnas.96.9.4752.

[30] P. Hennebelle and E. Falgarone. Turbulent molecular clouds. *A&A Rev.*, 20:55, November 2012. doi: 10.1007/s00159-012-0055-y.

[31] P. F. Hopkins, E. Quataert, and N. Murray. Self-regulated star formation in galaxies via momentum input from massive stars. *MNRAS*, 417:950–973, October 2011. doi: 10.1111/j.1365-2966.2011.19306.x.

[32] P. F. Hopkins, D. Kereš, J. Oñorbe, C.-A. Faucher-Giguère, E. Quataert, N. Murray, and J. S. Bullock. Galaxies on FIRE (Feedback In Realistic Environments): stellar feedback explains cosmologically inefficient star formation. *MNRAS*, 445:581–603, November 2014. doi: 10.1093/mnras/stu1738.

[33] C. B. Hummels and G. L. Bryan. Adaptive Mesh Refinement Simulations of Galaxy Formation: Exploring Numerical and Physical Parameters. *ApJ*, 749:140, April 2012. doi: 10.1088/0004-637X/749/2/140.

[34] C. B. Hummels, G. L. Bryan, B. D. Smith, and M. J. Turk. Constraints on hydrodynamical subgrid models from quasar absorption line studies of the simulated circumgalactic medium. *MNRAS*, 430:1548–1565, April 2013. doi: 10.1093/mnras/sts702.

[35] L. Iapichino, J. Adamek, W. Schmidt, and J. C. Niemeyer. Hydrodynamical adaptive mesh refinement simulations of turbulent flows - I. Substructure in a wind. *MNRAS*, 388:1079–1088, August 2008. doi: 10.1111/j.1365-2966.2008.13137.x.

[36] L. Iapichino, W. Schmidt, J. C. Niemeyer, and J. Merklein. Turbulence production and turbulent pressure support in the intergalactic medium. *MNRAS*, 414:2297–2308, July 2011. doi: 10.1111/j.1365-2966.2011.18550.x.

[37] L. Iapichino, M. Viel, and S. Borgani. Turbulence driven by structure formation in the circumgalactic medium. *MNRAS*, 432:2529–2540, July 2013. doi: 10.1093/mnras/stt611.

[38] R. E. Kalman. A New Approach to Linear Filtering and Prediction Problems. *Journal of Basic Engineering*, 82:35–45, 1960. doi: doi:10.1115/1.3662552.

[39] A. I. Karakas. Updated stellar yields from asymptotic giant branch models. *MNRAS*, 403:1413–1425, April 2010. doi: 10.1111/j.1365-2966.2009.16198.x.

[40] N. Katz, D. H. Weinberg, and L. Hernquist. Cosmological Simulations with TreeSPH. *MNRAS*, 105:19, July 1996. doi: 10.1086/192305.

[41] R. C. Kennicutt, Jr. The Global Schmidt Law in Star-forming Galaxies. *ApJ*, 498:541–552, May 1998. doi: 10.1086/305588.

[42] J.-h. Kim, T. Abel, O. Agertz, G. L. Bryan, D. Ceverino, C. Christensen, C. Conroy, A. Dekel, N. Y. Gnedin, N. J. Goldbaum, J. Guedes, O. Hahn, A. Hobbs, P. F. Hopkins, C. B. Hummels, F. Iannuzzi, D. Keres, A. Klypin, A. V. Kravtsov, M. R. Krumholz, M. Kuhlen, S. N. Leitner, P. Madau, L. Mayer, C. E. Moody, K. Nagamine, M. L. Norman, J. Onorbe, B. W. O'Shea, A. Pillepich, J. R. Primack, T. Quinn, J. I. Read, B. E. Robertson, M. Rocha, D. H. Rudd, S. Shen, B. D. Smith, A. S. Szalay, R. Teyssier, R. Thompson, K. Todoroki, M. J. Turk, J. W. Wadsley, J. H. Wise, A. Zolotov, and t. AGORA Collaboration29. The AGORA High-resolution Galaxy Simulations Comparison Project. *ApJS*, 210:14, January 2014. doi: 10.1088/0067-0049/210/1/14.

[43] A. A. Klypin. Numerical Simulations of Galaxy Formation: Cooling, Heating, Star \\ Formation. In V. Mueller, S. Gottloeber, J. P. Muecket, and J. Wambsganss, editors, *Large Scale Structure: Tracks and Traces*, pages 47–50, 1998.

[44] E. Komatsu, J. Dunkley, M. R. Nolta, C. L. Bennett, B. Gold, G. Hinshaw, N. Jarosik, D. Larson, M. Limon, L. Page, D. N. Spergel, M. Halpern, R. S. Hill, A. Kogut, S. S. Meyer, G. S. Tucker, J. L. Weiland, E. Wollack, and E. L. Wright. Five-Year Wilkinson Microwave Anisotropy Probe Observations: Cosmological Interpretation. *ApJS*, 180:330–376, February 2009. doi: 10.1088/0067-0049/180/2/330.

[45] M. R. Krumholz and C. F. McKee. A General Theory of Turbulence-regulated Star Formation, from Spirals to Ultraluminous Infrared Galaxies. *ApJ*, 630:250–268, September 2005. doi: 10.1086/431734.

[46] M. R. Krumholz, A. Dekel, and C. F. McKee. A Universal, Local Star Formation Law in Galactic Clouds, nearby Galaxies, High-redshift Disks, and Starbursts. *ApJ*, 745:69, January 2012. doi: 10.1088/0004-637X/745/1/69.

[47] L.D. Landau and E.M. Lifshits. *Lehrbuch der theoretischen Physik. In deutscher Sprache hrsg. von Paul Ziesche. Band VI: Hydrodynamik. In deutscher Sprache hrsg. von Wolfgang Weller. Übers. aus dem Russ. von Adolf Kühnel und Wolfgang Weller. (Textbook of theoretical physics. In German language edited by Paul Ziesche. Vol. VI: Hydrodynamics. In German language edited by Wolfgang Weller, Transl. from the Russian by Adolf Kühnel and Wolfgang Weller). 5., überarb. Aufl.* Berlin: Akademie-Verlag, 5., überarb. aufl. edition, 1991. ISBN 3-05-500070-6.

[48] K.-G. Lee, S. Bailey, L. E. Bartsch, W. Carithers, K. S. Dawson, D. Kirkby, B. Lundgren, D. Margala, N. Palanque-Delabrouille, M. M. Pieri, D. J. Schlegel, D. H. Weinberg, C. Yèche, É. Aubourg, J. Bautista, D. Bizyaev, M. Blomqvist, A. S. Bolton, A. Borde, H. Brewington, N. G. Busca, R. A. C. Croft, T. Delubac, G. Ebelke, D. J. Eisenstein, A. Font-Ribera, J. Ge, J.-C. Hamilton, J. F. Hennawi, S. Ho, K. Honscheid, J.-M. Le Goff, E. Malanushenko, V. Malanushenko, J. Miralda-Escudé, A. D. Myers, P. Noterdaeme, D. Oravetz, K. Pan, I. Pâris, P. Petitjean, J. Rich, E. Rollinde, N. P. Ross, G. Rossi, D. P. Schneider, A. Simmons, S. Snedden, A. Slosar, D. N. Spergel, N. Suzuki, M. Viel, and B. A. Weaver. The BOSS Lyα Forest Sample from SDSS Data Release 9. *AJ*, 145:69, March 2013. doi: 10.1088/0004-6256/145/3/69.

[49] E. Lévêque, F. Toschi, L. Shao, and J.-P. Bertoglio. Shear-improved Smagorinsky model for large-eddy simulation of wall-bounded turbulent

flows. *Journal of Fluid Mechanics*, 570:491–502, 2007. doi: 10.1017/S0022112006003429.

[50] A. Lewis, A. Challinor, and A. Lasenby. Efficient Computation of Cosmic Microwave Background Anisotropies in Closed Friedmann-Robertson-Walker Models. *ApJ*, 538:473–476, August 2000. doi: 10.1086/309179.

[51] M. S. Longair. *Galaxy Formation.* 2008.

[52] Z. Lukić, K. Heitmann, S. Habib, S. Bashinsky, and P. M. Ricker. The Halo Mass Function: High-Redshift Evolution and Universality. *ApJ*, 671:1160–1181, December 2007. doi: 10.1086/523083.

[53] Z. Lukić, C. Stark, P. Nugent, M. White, A. Meiksin, and A. Almgren. The Lyman-α forest in optically-thin hydrodynamical simulations. *ArXiv e-prints*, June 2014. doi: 10.1093/mnras/stu2377.

[54] M.-M. Mac Low and R. S. Klessen. Control of star formation by supersonic turbulence. *Reviews of Modern Physics*, 76:125–194, January 2004. doi: 10.1103/RevModPhys.76.125.

[55] Marie E. Machacek, Greg L. Bryan, Peter Anninos, Avery Meiksin, and Michael L. Norman. Simulating the lyman alpha forest. 1999.

[56] A. Maier, L. Iapichino, W. Schmidt, and J. C. Niemeyer. Adaptively Refined Large Eddy Simulations of a Galaxy Cluster: Turbulence Modeling and the Physics of the Intracluster Medium. *ApJ*, 707:40–54, December 2009. doi: 10.1088/0004-637X/707/1/40.

[57] D. Marchesini, P. G. van Dokkum, N. M. Förster Schreiber, M. Franx, I. Labbé, and S. Wuyts. The Evolution of the Stellar Mass Function of Galaxies from z = 4.0 and the First Comprehensive Analysis of its Uncertainties: Evidence for Mass-Dependent Evolution. *ApJ*, 701:1765–1796, August 2009. doi: 10.1088/0004-637X/701/2/1765. Schechter function definition.

[58] D. C. Martin, M. Matuszewski, P. Morrissey, J. D. Neill, A. Moore, C. C. Steidel, and R. Trainor. A Newly Forming Cold Flow Protogalactic Disk, a Signature of Cold Accretion from the Cosmic Web. *ApJ*, 824:L5, June 2016. doi: 10.3847/2041-8205/824/1/L5.

[59] Davide Martizzi, Oliver Hahn, Hao-Yi Wu, August E. Evrard, Romain Teyssier, and Risa H. Wechsler. Rhapsody-g simulations ii - baryonic growth and metal enrichment in massive galaxy clusters. October 2015.

[60] C. F. McKee and E. C. Ostriker. Theory of star formation. *ARA&A*, 45:565–687, September 2007. doi: 10.1146/annurev.astro.45.051806.110602.

[61] C. F. McKee and J. P. Ostriker. A theory of the interstellar medium - Three components regulated by supernova explosions in an inhomogeneous substrate. *ApJ*, 218:148–169, November 1977. doi: 10.1086/155667.

[62] A. A. Meiksin. The physics of the intergalactic medium. *Reviews of Modern Physics*, 81:1405–1469, October 2009. doi: 10.1103/RevModPhys.81.1405.

[63] G. H. Miller and P. Colella. A Conservative Three-Dimensional Eulerian Method for Coupled Solid-Fluid Shock Capturing. *Journal of Computational Physics*, 183:26–82, November 2002. doi: 10.1006/jcph.2002.7158.

[64] H. J. Mo and S. D. M. White. The abundance and clustering of dark haloes in the standard ΛCDM cosmogony. *MNRAS*, 336:112–118, October 2002. doi: 10.1046/j.1365-8711.2002.05723.x.

[65] Houjun Mo, Frank van den Bosch, and Simon White. *Galaxy Formation and Evolution*. Cambridge University Press, 2010. ISBN 0521857937.

[66] S. G. Murray, C. Power, and A. S. G. Robotham. HMFcalc: An online tool for calculating dark matter halo mass functions. *Astronomy and Computing*, 3:23–34, November 2013. doi: 10.1016/j.ascom.2013.11.001.

[67] M. L. Norman and G. L. Bryan. Cluster Turbulence. In H.-J. Röser and K. Meisenheimer, editors, *The Radio Galaxy Messier 87*, volume 530 of *Lecture Notes in Physics, Berlin Springer Verlag*, page 106, 1999. doi: 10.1007/BFb0106425.

[68] Pierre Ocvirk, Nicolas Gillet, Paul R. Shapiro, Dominique Aubert, Ilian T. Iliev, Romain Teyssier, Gustavo Yepes, Jun-Hwan Choi, David Sullivan, Alexander Knebe, Stefan Gottloeber, Anson D'Aloisio, Hyunbae Park, Yehuda Hoffman, and Timothy Stranex. Cosmic dawn (coda): the first radiation-hydrodynamics simulation of reionization and galaxy formation in the local universe. November 2015.

[69] B. D. Oppenheimer and J. Schaye. Non-equilibirum ionization and cooling of metal-enriched gas in the presence of a photoionization background. *MNRAS*, 434:1043–1062, September 2013. doi: 10.1093/mnras/stt1043.

[70] B. D. Oppenheimer, R. Davé, N. Katz, J. A. Kollmeier, and D. H. Weinberg. The intergalactic medium over the last 10 billion years - II. Metal-line absorption and physical conditions. *MNRAS*, 420:829–859, February 2012. doi: 10.1111/j.1365-2966.2011.20096.x.

[71] A. Pallottini, A. Ferrara, S. Gallerani, S. Salvadori, and V. D'Odorico. Simulating cosmic metal enrichment by the first galaxies. *MNRAS*, 440:2498–2518, May 2014. doi: 10.1093/mnras/stu451.

[72] A. Pallottini, S. Gallerani, and A. Ferrara. The circumgalactic medium of high-redshift galaxies. *MNRAS*, 444:L105–L109, October 2014. doi: 10.1093/mnrasl/slu126.

[73] P. G. Pérez-González, G. H. Rieke, V. Villar, G. Barro, M. Blaylock, E. Egami, J. Gallego, A. Gil de Paz, S. Pascual, J. Zamorano, and J. L. Donley. The Stellar Mass Assembly of Galaxies from z = 0 to z = 4: Analysis of a Sample Selected in the Rest-Frame Near-Infrared with Spitzer. *ApJ*, 675:234–261, March 2008. doi: 10.1086/523690.

[74] Planck Collaboration, P. A. R. Ade, N. Aghanim, C. Armitage-Caplan, M. Arnaud, M. Ashdown, F. Atrio-Barandela, J. Aumont, C. Baccigalupi, A. J. Banday, and et al. Planck 2013 results. XVI. Cosmological parameters. *A&A*, 571:A16, November 2014. doi: 10.1051/0004-6361/201321591.

[75] Planck Collaboration, P. A. R. Ade, N. Aghanim, M. Arnaud, M. Ashdown, J. Aumont, C. Baccigalupi, A. J. Banday, R. B. Barreiro, J. G. Bartlett, N. Bartolo, E. Battaner, R. Battye, K. Benabed, A. Benoit, A. Benoit-Levy, J. P. Bernard, M. Bersanelli, P. Bielewicz, A. Bonaldi, L. Bonavera, J. R. Bond, J. Borrill, F. R. Bouchet, F. Boulanger, M. Bucher, C. Burigana, R. C. Butler, E. Calabrese, J. F. Cardoso, A. Catalano, A. Challinor, A. Chamballu, R. R. Chary, H. C. Chiang, J. Chluba, P. R. Christensen, S. Church, D. L. Clements, S. Colombi, L. P. L. Colombo, C. Combet, A. Coulais, B. P. Crill, A. Curto, F. Cuttaia, L. Danese, R. D. Davies, R. J. Davis, P. de Bernardis, A. de Rosa, G. de Zotti, J. Delabrouille, F. X. Desert, E. Di Valentino, C. Dickinson, J. M. Diego, K. Dolag, H. Dole, S. Donzelli, O. Dore, M. Douspis, A. Ducout, J. Dunkley, X. Dupac, G. Efstathiou, F. Elsner, T. A. Ensslin, H. K. Eriksen, M. Farhang, J. Fergusson, F. Finelli, O. Forni, M. Frailis, A. A. Fraisse, E. Franceschi, A. Frejsel, S. Galeotta, S. Galli, K. Ganga, C. Gauthier, M. Gerbino, T. Ghosh, M. Giard, Y. Giraud-Heraud, E. Giusarma, E. Gjerlow, J. Gonzalez-Nuevo, K. M. Gorski, S. Gratton, A. Gregorio, A. Gruppuso, J. E. Gudmundsson, J. Hamann, F. K. Hansen, D. Hanson, D. L. Harrison, G. Helou, S. Henrot-Versille, C. Hernandez-Monteagudo, D. Herranz, S. R. Hildebrandt, E. Hivon, M. Hobson, W. A. Holmes, A. Hornstrup, W. Hovest, Z. Huang, K. M. Huffenberger, G. Hurier, A. H. Jaffe, T. R. Jaffe, W. C. Jones, M. Juvela, E. Keihanen, R. Keskitalo, T. S. Kisner, R. Kneissl, J. Knoche, L. Knox, M. Kunz, H. Kurki-Suonio, G. Lagache, A. Lahteenmaki, J. M. Lamarre, A. Lasenby, M. Lattanzi, C. R. Lawrence, J. P. Leahy, R. Leonardi, J. Lesgourgues, F. Levrier, A. Lewis, M. Liguori, P. B. Lilje, M. Linden-Vornle, M. Lopez-Caniego, P. M. Lubin, J. F. Macias-Perez, G. Maggio, D. Maino, N. Mandolesi, A. Mangilli, A. Marchini, P. G. Martin, M. Martinelli, E. Martinez-Gonzalez, S. Masi, S. Matarrese, P. Mazzotta, P. McGehee, P. R. Meinhold, A. Melchiorri, J. B. Melin, L. Mendes, A. Mennella, M. Migliaccio, M. Millea, S. Mitra,

M. A. Miville-Deschenes, A. Moneti, L. Montier, G. Morgante, D. Mortlock, A. Moss, D. Munshi, J. A. Murphy, P. Naselsky, F. Nati, P. Natoli, C. B. Netterfield, H. U. Norgaard-Nielsen, F. Noviello, D. Novikov, I. Novikov, C. A. Oxborrow, F. Paci, L. Pagano, F. Pajot, R. Paladini, D. Paoletti, B. Partridge, F. Pasian, G. Patanchon, T. J. Pearson, O. Perdereau, L. Perotto, F. Perrotta, V. Pettorino, F. Piacentini, M. Piat, E. Pierpaoli, D. Pietrobon, S. Plaszczynski, E. Pointecouteau, G. Polenta, L. Popa, G. W. Pratt, G. Prezeau, S. Prunet, J. L. Puget, J. P. Rachen, W. T. Reach, R. Rebolo, M. Reinecke, M. Remazeilles, C. Renault, A. Renzi, I. Ristorcelli, G. Rocha, C. Rosset, M. Rossetti, G. Roudier, B. Rouille d'Orfeuil, M. Rowan-Robinson, J. A. Rubino-Martin, B. Rusholme, N. Said, V. Salvatelli, L. Salvati, M. Sandri, D. Santos, M. Savelainen, G. Savini, D. Scott, M. D. Seiffert, P. Serra, E. P. S. Shellard, L. D. Spencer, M. Spinelli, V. Stolyarov, R. Stompor, R. Sudiwala, R. Sunyaev, D. Sutton, A. S. Suur-Uski, J. F. Sygnet, J. A. Tauber, L. Terenzi, L. Toffolatti, M. Tomasi, M. Tristram, T. Trombetti, M. Tucci, J. Tuovinen, M. Turler, G. Umana, L. Valenziano, J. Valiviita, B. Van Tent, P. Vielva, F. Villa, L. A. Wade, B. D. Wandelt, I. K. Wehus, M. White, S. D. M. White, A. Wilkinson, D. Yvon, A. Zacchei, and A. Zonca. Planck 2015 results. xiii. cosmological parameters. February 2015.

[76] Stephen B. Pope. *Turbulent flows*. Cambridge University Press, Cambridge, 2000. ISBN 0-521-59125-2. Réimpressions (avec des corrections) : 2001, 2003, 2005, 2008, 2010.

[77] L. Portinari, C. Chiosi, and A. Bressan. Galactic chemical enrichment with new metallicity dependent stellar yields. *A&A*, 334:505–539, June 1998.

[78] C. Power and A. Knebe. The impact of box size on the properties of dark matter haloes in cosmological simulations. *MNRAS*, 370:691–701, August 2006. doi: 10.1111/j.1365-2966.2006.10562.x.

[79] William H. Press, Saul A. Teukolsky, William T. Vetterling, and Brian P. Flannery. *Numerical Recipes 3rd Edition: The Art of Scientific Computing*. Cambridge University Press, 3 edition, 2007. ISBN 0521880688.

[80] C. M. Raiteri, M. Villata, and J. F. Navarro. Simulations of Galactic chemical evolution. I. O and Fe abundances in a simple collapse model. *A&A*, 315:105–115, November 1996. URL `http://adsabs.harvard.edu/cgi-bin/nph-data_query?bibcode=1996A%26A...315..105R&link_type=ARTICLE&db_key=AST&high=`.

[81] M. Rauch. The Lyman Alpha Forest in the Spectra of QSOs. *ARA&A*, 36:267–316, 1998. doi: 10.1146/annurev.astro.36.1.267.

[82] P. Santini, R. Maiolino, B. Magnelli, D. Lutz, A. Lamastra, G. Li Causi, S. Eales, P. Andreani, S. Berta, V. Buat, A. Cooray, G. Cresci, E. Daddi, D. Farrah, A. Fontana, A. Franceschini, R. Genzel, G. Granato, A. Grazian, E. Le Floc'h, G. Magdis, M. Magliocchetti, F. Mannucci, N. Menci, R. Nordon, S. Oliver, P. Popesso, F. Pozzi, L. Riguccini, G. Rodighiero, D. J. Rosario, M. Salvato, D. Scott, L. Silva, L. Tacconi, M. Viero, L. Wang, S. Wuyts, and K. Xu. The evolution of the dust and gas content in galaxies. *A&A*, 562:A30, February 2014. doi: 10.1051/0004-6361/201322835.

[83] J. Schaye and C. Dalla Vecchia. On the relation between the Schmidt and Kennicutt-Schmidt star formation laws and its implications for numerical simulations. *MNRAS*, 383:1210–1222, January 2008. doi: 10.1111/j.1365-2966.2007.12639.x.

[84] J. Schaye, C. Dalla Vecchia, C. M. Booth, R. P. C. Wiersma, T. Theuns, M. R. Haas, S. Bertone, A. R. Duffy, I. G. McCarthy, and F. van de Voort. The physics driving the cosmic star formation history. *MNRAS*, 402:1536–1560, March 2010. doi: 10.1111/j.1365-2966.2009.16029.x.

[85] P. Schechter. An analytic expression for the luminosity function for galaxies. *ApJ*, 203:297–306, January 1976. doi: 10.1086/154079.

[86] M. Schmidt. The Rate of Star Formation. *ApJ*, 129:243, March 1959. doi: 10.1086/146614.

[87] W. Schmidt. In preparation.

[88] W. Schmidt. Large Eddy Simulations in Astrophysics. *Living Reviews in Computational Astrophysics*, 1, October 2015. doi: 10.1007/lrca-2015-2.

[89] W. Schmidt and C. Federrath. A fluid-dynamical subgrid scale model for highly compressible astrophysical turbulence. *A&A*, 528:A106, April 2011. doi: 10.1051/0004-6361/201015630.

[90] W. Schmidt, J. C. Niemeyer, and W. Hillebrandt. A localised subgrid scale model for fluid dynamical simulations in astrophysics. I. Theory and numerical tests. *A&A*, 450:265–281, April 2006. doi: 10.1051/0004-6361:20053617.

[91] W. Schmidt, A. S. Almgren, H. Braun, J. F. Engels, J. C. Niemeyer, J. Schulz, R. R. Mekuria, A. J. Aspden, and J. B. Bell. Cosmological fluid mechanics with adaptively refined large eddy simulations. *MNRAS*, 440:3051–3077, June 2014. doi: 10.1093/mnras/stu501.

[92] W. Schmidt, J. F. Engels, J. C. Niemeyer, and A. S. Almgren. Hot and turbulent gas in clusters. *MNRAS*, 459:701–719, June 2016. doi: 10.1093/mnras/stw632.

[93] W. Schmidt, C. Byrohl, J. F. Engels, C. Behrens, and J. C. Niemeyer. Viscosity, pressure and support of the gas in simulations of merging cool-core clusters. *MNRAS*, 470:142–156, September 2017. doi: 10.1093/mnras/stx1274.

[94] S. Shen, J. Wadsley, and G. Stinson. The enrichment of the intergalactic medium with adiabatic feedback - I. Metal cooling and metal diffusion. *MNRAS*, 407:1581–1596, September 2010. doi: 10.1111/j.1365-2966.2010.17047.x.

[95] S. Shen, P. Madau, A. Aguirre, J. Guedes, L. Mayer, and J. Wadsley. The Origin of Metals in the Circumgalactic Medium of Massive Galaxies at z = 3. *apj*, 760:50, November 2012. doi: 10.1088/0004-637X/760/1/50.

[96] R. K. Sheth, H. J. Mo, and G. Tormen. Ellipsoidal collapse and an improved model for the number and spatial distribution of dark matter haloes. *MNRAS*, 323:1–12, May 2001. doi: 10.1046/j.1365-8711.2001.04006.x.

[97] J. Silk. On the fragmentation of cosmic gas clouds. I - The formation of galaxies and the first generation of stars. *ApJ*, 211:638–648, February 1977. doi: 10.1086/154972.

[98] A. Slosar, V. Iršič, D. Kirkby, S. Bailey, N. G. Busca, T. Delubac, J. Rich, É. Aubourg, J. E. Bautista, V. Bhardwaj, M. Blomqvist, A. S. Bolton, J. Bovy, J. Brownstein, B. Carithers, R. A. C. Croft, K. S. Dawson, A. Font-Ribera, J.-M. Le Goff, S. Ho, K. Honscheid, K.-G. Lee, D. Margala, P. McDonald, B. Medolin, J. Miralda-Escudé, A. D. Myers, R. C. Nichol, P. Noterdaeme, N. Palanque-Delabrouille, I. Pâris, P. Petitjean, M. M. Pieri, Y. Piškur, N. A. Roe, N. P. Ross, G. Rossi, D. J. Schlegel, D. P. Schneider, N. Suzuki, E. S. Sheldon, U. Seljak, M. Viel, D. H. Weinberg, and C. Yèche. Measurement of baryon acoustic oscillations in the Lyman-α forest fluctuations in BOSS data release 9. *J. Cosmology Astropart. Phys.*, 4:026, April 2013. doi: 10.1088/1475-7516/2013/04/026.

[99] B. D. Smith, E. J. Hallman, J. M. Shull, and B. W. O'Shea. The Nature of the Warm/Hot Intergalactic Medium. I. Numerical Methods, Convergence, and O VI Absorption. *ApJ*, 731:6, April 2011. doi: 10.1088/0004-637X/731/1/6.

[100] V. Springel. The cosmological simulation code GADGET-2. *MNRAS*, 364:1105–1134, December 2005. doi: 10.1111/j.1365-2966.2005.09655.x.

[101] V. Springel and L. Hernquist. Cosmological smoothed particle hydrodynamics simulations: a hybrid multiphase model for star formation. *MNRAS*, 339:289–311, February 2003. doi: 10.1046/j.1365-8711.2003.06206.x.

[102] C. C. Steidel, D. K. Erb, A. E. Shapley, M. Pettini, N. Reddy, M. Bogosavljević, G. C. Rudie, and O. Rakic. The Structure and Kinematics of the

Circumgalactic Medium from Far-ultraviolet Spectra of z ~= 2-3 Galaxies. *ApJ*, 717:289–322, July 2010. doi: 10.1088/0004-637X/717/1/289.

[103] C. C. Steidel, M. Bogosavljević, A. E. Shapley, J. A. Kollmeier, N. A. Reddy, D. K. Erb, and M. Pettini. Diffuse Lyα Emitting Halos: A Generic Property of High-redshift Star-forming Galaxies. *ApJ*, 736:160, August 2011. doi: 10.1088/0004-637X/736/2/160.

[104] Kung-Yi Su, Philip F. Hopkins, Christopher C. Hayward, Claude-Andre Faucher-Giguere, Dusan Keres, Xiangcheng Ma, and Victor H. Robles. Feedback first: the surprisingly weak effects of magnetic fields, viscosity, conduction, and metal diffusion on galaxy formation. July 2016.

[105] The Enzo Collaboration. ENZO: An Adaptive Mesh Refinement Code for Astrophysics. *ApJS*, 211:19, April 2014. doi: 10.1088/0067-0049/211/2/19.

[106] K. Thornton, M. Gaudlitz, H.-T. Janka, and M. Steinmetz. Energy Input and Mass Redistribution by Supernovae in the Interstellar Medium. *ApJ*, 500:95–119, June 1998. doi: 10.1086/305704.

[107] B. M. Tinsley. Evolution of the Stars and Gas in Galaxies. *Fund. Cosmic Phys.*, 5:287–388, 1980.

[108] M. J. Turk, B. D. Smith, J. S. Oishi, S. Skory, S. W. Skillman, T. Abel, and M. L. Norman. yt: A Multi-code Analysis Toolkit for Astrophysical Simulation Data. *ApJS*, 192:9, January 2011. doi: 10.1088/0067-0049/192/1/9.

[109] F. Vazza, E. Roediger, and M. Brüggen. Turbulence in the ICM from mergers, cool-core sloshing, and jets: results from a new multi-scale filtering approach. *A&A*, 544:A103, August 2012. doi: 10.1051/0004-6361/201118688.

[110] M. Viel, M. G. Haehnelt, and V. Springel. The effect of neutrinos on the matter distribution as probed by the intergalactic medium. *J. Cosmology Astropart. Phys.*, 6:15, June 2010. doi: 10.1088/1475-7516/2010/06/015.

[111] M. Vogelsberger, S. Genel, D. Sijacki, P. Torrey, V. Springel, and L. Hernquist. A model for cosmological simulations of galaxy formation physics. *MNRAS*, 436:3031–3067, December 2013. doi: 10.1093/mnras/stt1789.

[112] Steven Weinberg. *Cosmology*. Oxford University Press, 2008.

[113] R. P. C. Wiersma, J. Schaye, and B. D. Smith. The effect of photoionization on the cooling rates of enriched, astrophysical plasmas. *MNRAS*, 393:99–107, February 2009. doi: 10.1111/j.1365-2966.2008.14191.x.

[114] S. M. Wilkins, N. Trentham, and A. M. Hopkins. The evolution of stellar mass and the implied star formation history. *MNRAS*, 385:687–694, April 2008. doi: 10.1111/j.1365-2966.2008.12885.x.

[115] David John Williamson, Hugo Martel, and Daisuke Kawata. Metal diffusion in smoothed particle hydrodynamics simulations of dwarf galaxies. February 2016.

[116] S. Zaroubi. The epoch of reionization. In T. Wiklind, B. Mobasher, and V. Bromm, editors, *The First Galaxies*, volume 396 of *Astrophysics and Space Science Library*, page 45, 2013. doi: 10.1007/978-3-642-32362-1_2.

[117] Y. B. Zel'dovich. Gravitational instability: An approximate theory for large density perturbations. *A&A*, 5:84–89, March 1970.

[118] Weiqun Zhang, Ann Almgren, Marcus Day, Tan Nguyen, John Shalf, and Didem Unat. Boxlib with tiling: An amr software framework. April 2016.

Danksagung

An erster Stelle möchte ich meinem Betreuer und Erstgutachter Jens Niemeyer für die Möglichkeit zur Promotion danken. Auch meinem Zweitgutachter, Ansgar Reiners, möchte ich für die Bereitschaft sich mit meiner Arbeit auseinanderzusetzen danken. Besonderer Dank gilt Wolfram Schmidt, er hat mir in vielen Situationen fachlich zur Seite gestanden und auch die Entstehung dieser Arbeit intensiv begleitet.

Meinen Büromitbewohnern, Christoph Behrens und Harald Braun, bin ich für vieles – inhaltliches, wie auch soziales – dankbar.

Steffen Klemer, Roland Ring, meinen Eltern und Charlotte Rothfuchs danke ich für vieles, aber insbesondere für emotionale und mentale Unterstützung und die pedantische Diskussion von sprachlichen Aspekten.

Dankbar bin ich auch den vielen guten Geistern, die hinter den Kulissen diese Arbeit möglich und mir in vielen Situationen das Leben leichter gemacht haben, die ich aber nicht namentlich erwähne.